2010

# Lead-free, bronze-based surface layers for wear resistance in axial piston hydraulic pumps

Greg Vetterick
*Iowa State University*

# Lead-free, bronze-based surface layers for wear resistance in axial piston hydraulic pumps

by

Gregory Alan Vetterick

A thesis submitted to the graduate faculty

in partial fulfillment of the requirements for the degree of

MASTER OF SCIENCE

Major: Materials Science and Engineering

Program of Study Committee:
Iver E. Anderson, Major Professor
Scott Chumbley
Palaniappa A. Molian

Iowa State University

Ames, Iowa

2010

# TABLE OF CONTENTS

# LIST OF FIGURES

# LIST OF TABLES

# ABSTRACT

Concerns regarding the safety of lead have provided sufficient motivation to develop substitute materials for the surface layer on a thrust bearing type component known as a valve plate in axial piston hydraulic pumps that consists of 10% tin, 10% lead, and the remainder copper (in wt. %). A recently developed replacement material, a Cu-10Sn-3Bi (wt.%) P/M bronze, was found to be unsuitable as valve plate surface layer, requiring the development of a new alloy. A comparison of the Cu-10Sn-10Pb and Cu-10Sn-3Bi powder metal valve plates showed that the differences in wear behavior between the two alloys arose due to the soft phase bismuth in the alloy that is known to cause both solid and liquid metal embrittlement of copper alloys.

A lead-free alternative was developed by using infiltration of high-tin alloys into porous bronze compacts compacted at 350MPa and sintered for 2 hours at 650°C to replicate the dual phase structure of leaded bronze. The resulting engineered composite had a lower volume loss than samples of leaded and bismuth bronze under lubricated wear test conditions. It also possessed a similar coefficient of friction and abrasive/plowing mechanism of wear as the Cu-10Sn-10Pb alloys. The results of wear testing show that the alloy demonstrates wear resistant properties comparable to those of the very successful leaded-bronze alloys.

Furthermore, the microstructure of the composite alloy can be engineered by increasing the compaction pressure and sintering temperature of the bronze to balance strength and percentage of the soft phase to match the end use. Also critical to the alloys performance is the control of copper-tin intermetallic formation and growth. The amount of intermetallics could be controlled by minimizing time at temperature during infiltration. In addition, it was shown that growth of the copper-tin $Cu_3Sn$ intermetallic can mitigated by the addition of manganese.

# CHAPTER 1. OVERVIEW

## 1.1 Introduction

Copper was the first metal mined and crafted by man, so it only follows that its oldest known alloy, the tin-copper metal called bronze, was used to reduce friction and wear as early as the 4th century B.C. (Lunn, 1965; Dowson, 1998; Davis, 2001). By this time in China, lubricated bronze bearings were being utilized in sophisticated spoked wheels (Dowson, 1998). The reduction of wear became more important with the dawn of the industrial age with the development of high speed mechanized equipment. In the latter half of the 19th century, the heavily loaded machines of the industrialized aged required new bearing technology. As a result, tribological systems consisting of dissimilar metals such as iron and bronze found prominence (Dowson, 1998). The iron/bronze tribological system was strong enough to support heavy loads but soft enough to deform to prevent wear. While adequate for highly loaded bearings, iron and bronze were not always suitable to prevent wear in a given application.

Therefore, soft metals with low yield strengths such as lead and tin were used in low stress applications where their excellent ability to deform due to abrasive wear particles was essential. In 1839, Isaac Babbitt patented tin-based alloys containing copper and antimony to refine their strength (Dowson, 1998). Together with lead-based alloys they became known as babbitts or white metals and are still in use today. To bridge the gap between the strong bronzes and the soft babbitt metals, a bronze or steel backing is often used to increase the fatigue characteristics and apparent strength of the lead or tin-based bearings (Dowson, 1998).

A widely employed variation of one of these multi-layered systems is a cast, leaded-tin bronze. When the cast metal solidifies, the insoluble lead creates free globules in the bronze matrix. The composite-like microstructure combines the strength of the bronze and deformability of the lead just as the bimetal bearings do. From 1875-1890, Dr. C.B. Dudley, a chemist with the Pennsylvania Railroad Company, studied the wear of several leaded bronze alloys as bearing materials in locomotives and cars (Lunn, 1965). Dr. Dudley's work led to specifications for a material that would be vital throughout the industrial revolution and in a

multitude of applications since. Leaded bronze alloys have been used in a wide range of applications including farm machinery, automotive engines, home appliances, and pumps.

## 1.2 Motivation

Although engineers have successfully employed lead containing alloys for a range of applications, the lead must be replaced with alternatives as the world looks to reduce the use of toxic materials wherever possible. The effort to reduce the use of lead political pressure was put into tangible form when the European Union passed Directive 2002/95/EC, the Restriction of certain Hazardous Substances Directive (RoHS). The edict requires substitution for various heavy metals (lead, mercury, cadmium, and hexavalent chromium) in new electrical and electronic equipment put on the market after July 1, 2006. Although this directive was mainly aimed at electrical and electronic equipment, it included a wide swath of engineering applications. Some of these applications did not yet have a viable replacement material. Thus exemptions were made for "lead as a copper alloy containing up to 4 % lead by weight" and later for "lead in lead-bronze bearing shells and bushes" (European Union, 2002 & 2005).

While the exemptions currently allow for leaded tin-bronzes in bearing materials, there is concern among companies, even those outside of the 25 European Union member states (plus Iceland, Liechtenstein and Norway) that restrictions will be tightened in the future. In the United States, similar legislation has not been passed. Lead was, however, identified as one of 31 Priority Chemicals by the United States Environmental Protection Agency in 1998. It is also one of three metals (Lead, Cadmium, and Mercury) on the National Waste Minimization Program's list of chemicals found in U.S. products and wastes that warrant elimination or a substantial reduction (EPA, 2008).

## 1.3 Problem Statement

The legal developments in the United States and European Union have provided companies such as Sauer Danfoss, the industrial partner for this research, with sufficient motivation to develop substitute materials to replace leaded bronze components. In particular, Sauer Danfoss is looking to replace the lead-containing surface layer on a thrust bearing known as a valve plate in axial piston hydraulic pumps. The valve plate is a component that provides a

low friction surface for a cylinder block to rotate against. In certain axial piston hydraulic pumps produced by Sauer Danfoss, a leaded-bronze alloy consisting of 10% tin, 10% lead, and the remainder copper (in wt. %) is used as the surface layer on the valve plate. Although leaded bronze is effective in this application, it may be subject to future legislation like RoHS, so preemptive action is required.

Valve plate surface layers produced for Sauer Danfoss use a water-atomized, prealloyed Cu-10Sn-10Pb powder. This powder is roll-pressed onto a steel backing plate and liquid phase sintered to allow the formation of soft lead phase pockets. The leaded valve plates perform excellently, and are not considered a component that determines the lifetime of the hydraulic pump. However, the environmental and health issues of lead dictate that a new environmentally benign, lead-free material must be developed that performs as well as the leaded bronze.

To replace the leaded bronze as valve plate surface layers, Sauer Danfoss tested a Federal Mogul designed, Cu-10Sn-3Bi (wt.%) bronze. Like the leaded bronze alloys, the Cu-10Sn-3Bi material was designed to produce soft phase pockets using the insolubility of the second phase, in this case bismuth (Saxton, 2006). The bismuth bronze valve plate surface layers were also produced by a powder metallurgy (P/M) process, although the exact production method was proprietary (Sauer, 2008). The Cu-10Sn-3Bi composition demonstrated good wear characteristics in automotive applications, including increased fatigue and corrosion resistance. However, testing in axial piston hydraulic pumps showed that the Cu-10Sn-3Bi material was unsuitable as a bearing material for valve plate surface layers (Sauer, 2009).

The failure of the Cu-10Sn-3Bi lead-free material in axial piston hydraulic pumps meant there was still a need for an acceptable lead-free solution. The objective of this study was to determine the nature of the wear mechanisms in Sauer Danfoss systems including the production-level Cu-10Sn-10Pb and experimental Cu-10Sn-3Bi valve plate materials against a proprietary copper-infiltrated, P/M steel cylinder block face. The results of this characterization were then to be used to develop a new bearing alloy that was free of toxic materials like lead and had properties required to not fail under conditions found in axial piston hydraulic pumps. Once a candidate material was developed, appropriate laboratory equipment and testing regimes were to be used to qualify the material as a replacement for the Cu-10Sn-10Pb valve plates employed by Sauer Danfoss.

## 1.4 Organization of Work

The development of a new bearing material for axial piston hydraulic pumps was divided into three phases: characterization of the current tribological system, design of a new alloy, and the validation of the new bearing material. Each of these steps was critical to developing a material that would perform in the harsh conditions present in hydraulic pumps.

Scanning electron microscopy (SEM) and energy dispersive X-ray spectroscopy (EDS) were used to examine the wear damage on the Cu-10Sn-10Pb and Cu-10Sn-3Bi valve plate materials after they were run in hydraulic pump bench tests with a copper infiltrated, P/M steel cylinder block. These tests were used to determine the dominant wear mechanisms in axial piston hydraulic pumps and the possible mode of failure for the bismuth bronze valve plates. The type of wear mechanisms determine the properties required of the new, lead-free material.

To explain the poor performance of the bismuth bronze valve plates, performance that stands in stark contrast to the reported success in automotive applications, the wear performance of each material was correlated back to its microstructure. Examination of the microstructure was also used to determine the precise method used to produce the bismuth bronze valve plates since certain aspects of the manufacturing process were unknown. (Betz, 2009).

The results of the first phase of the research were then used to develop an effective, lead-free material designed to avoid the problems experienced with the bismuth bronze samples. Copper based alloys such as bronze are utilized throughout the tribological industry in sliding pairs with ferrous alloys with great success. Therefore, the development of a new alloy focused on determining an effective soft phase to replace the free lead and a means of producing the final bearing material.

After the material was developed, the third phase of the project was the validation of the material as a bearing alloy. The primary measure of performance in this study was the wear capability of the alloy. To evaluate this criterion, pin-on-disk testing was used to determine the wear performance in terms of friction, mass loss, wear type, and possible failure modes. In addition, strength and aging tests were used to provide additional data on the reliability of the material.

# CHAPTER 2. REVIEW OF LITERATURE

## 2.1 Hydraulic Systems and Pump Operation

The earliest examples of fluid used to perform work (i.e. hydraulics) date back to the Egyptians and Chinese and utilized the kinetic energy of fluids to perform work. (Akers et. al., 2006). Early examples were mainly systems developed for irrigation and, later, around 100 B.C., water powered grain mills (Lambeck, 1983). The first hydraulic pumps, such as Archamides' screw, were designed around the time of the third century B.C. to move water (Lambeck, 1983).

Today, hydraulics is customarily associated with the use of the potential energy of pressurized fluids. One of the first examples of hydraulics using potential energy was the use of water to quarry marble. Water was poured into bored holes in the marble and wooden plugs were driven into the tops of the holes, creating hydrostatic pressure that resulted in a controlled fracture in the marble (Akers et. al., 2006). The theory behind hydraulics was not explored in depth until around the 1600's and has only led to the strong, capable, and precise hydraulic systems in use today after centuries of research in often utterly unrelated fields (Akers et. al., 2006; Lambeck, 1983).

### 2.1.1 Hydraulic Systems

Modern hydraulic systems are most commonly used as one of three methods (mechanical, electrical, and fluid) to transfer power. Hydraulics are particularly useful in applications requiring large forces and slow speeds with minimal weight and volume. Instead of transmitting power via electricity or mechanical means (gears, belts, chains, etc.), a hydraulic system uses an incompressible fluid to transmit power from a drive power unit to a remote end use. The fluid, often a petroleum based oil, is pressurized by a hydraulic pump and transmitted through high pressure hoses to a motor or actuator. The motor or actuator then performs the required movement, the action of which is controlled with valves or physical manipulation of the pump. There are two main classifications of hydraulic systems; closed circuit and open circuit. In an open circuit, hydraulic fluid is pumped to the actuator or motor to perform the work, then subsequently released into the reservoir as shown in Figure 1.

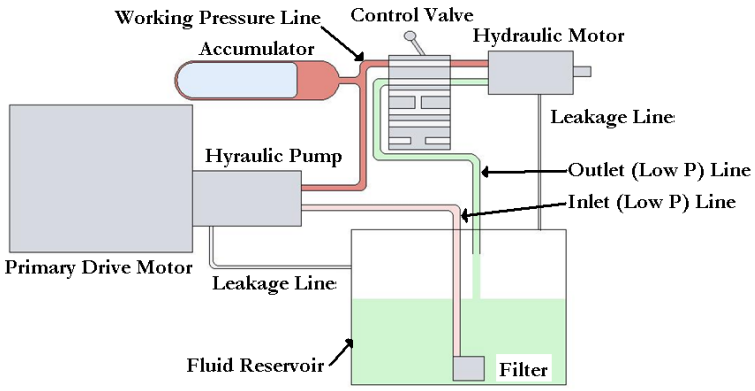


**Figure 1. A basic open loop hydraulic system.**

In contrast to the open loop hydraulic system, a closed circuit system (Figure 2) returns the fluid from the load, usually a fixed displacement hydraulic motor back to the pump inlet. The pump is typically a variable volume pump that is able to change the speed and direction of the output hydraulic motor. The theoretical design of the system uses a constant volume of hydraulic fluid, but design tolerances of the pump and motor create internal leakages. These internal leaks are subsequently used to lubricate and cool the pump however these, in conjunction with external leaks, result in fluid loss from the closed circuit which must be replenished to prevent cavitation. To accomplish this task, a small secondary pump is used to provide the amount of fluid that is lost by the circuit through leakage losses.

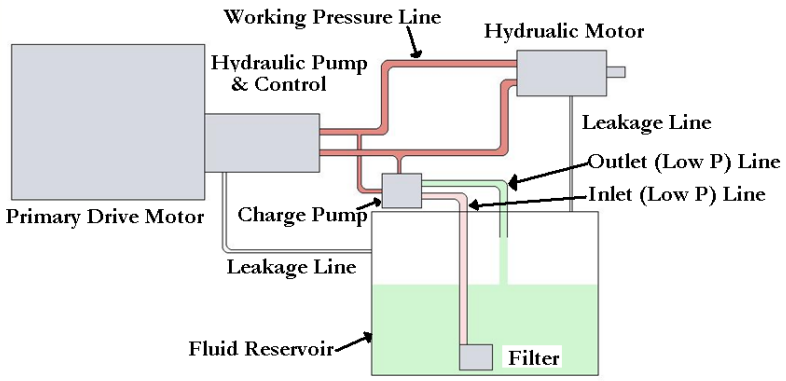


**Figure 2. A basic closed loop hydraulic system.**

Closed circuit hydraulic systems are the basis behind hydrostatic transmissions. The basic hydrostatic transmission consists of a variable displacement axial piston pump connected to a fixed displacement axial piston motor. The variable displacement pump is driven by a primary

mechanical source such as an internal combustion engine or electric motor. The bidirectional fixed volume motor is driven by the fluid discharged from the pump and is used to drive a machine such as a vehicle, hoist, or conveyor. The direction and speed of rotation of the fixed motor shaft depends on the flow from the pump. Axial piston pumps are able to reverse the direction of flow without the primary drive motor changing direction. These pumps also allow for a smooth, stepless transition in flow rate even through zero displacement. This allows the hydraulic pump, and therefore the motor, to transition between any speed and reverse direction seamlessly (Lambeck, 1983). The ability to reverse direction can also be utilized to arrest the motion of the motor using fully hydrostatic braking.

### 2.1.2 Axial Piston Pump Operation

Variable displacement axial piston pumps are critical in making hydrostatic drives work. Axial piston style pumps are a type of positive displacement, or hydrostatic, pump. Positive displacement pumps work by allowing an expanding volume (i.e. a cylinder) to fill with pressurized fluid from an inlet port, then forcing the fluid through an outlet port at a higher pressure by reducing the chamber's volume. Other examples of positive displacement pumps include spur gear, internal gear, gerotor, vane, and screw type pumps (Akers et. al., 2006). The counterpart to (hydrostatic) positive displacement pumps is the hydrodynamic pump. These pumps use a spinning rotor that increases the velocity of the fluid. This mechanism is not applicable to most hydraulic systems that employ the potential energy of high pressure fluid. Positive displacement pumps, on the other hand, perform well, especially when considering pump size and efficiency.

If leakage and mechanical strength considerations are ignored, hydrostatic pumps could pump fluid at any speed and over any pressure difference, however realistic system and material properties prevent high speed (bearing damage) or high pressure (drive shaft or casing failure) operation (Akers et. al., 2006). The pumps must be protected by relief valves or, in the case of variable displacement pumps, a device that would automatically reduce positive displacement to zero at some preset system working pressure (Akers et. al., 2006).

While positive displacement pumps cannot achieve infinite speed and pressure, they are widely used for applications that require high pressure and accurate control of discharge volume.

Gear-type and vane-type pumps commonly run at 2,000-4,000PSI, and piston pumps are capable of pressures from less than 3,000PSI up to 15,000PSI in extreme applications (Villforth III, 1996). Piston pumps are also capable of running reliably over a wide range of pressures, making them useful for hydrostatic transmission applications.

Piston pumps come in three major varieties; radial, bent axis, and swash plate axial pumps. The axial piston is commonly used in hydrostatic transmissions, and as its name implies, consists of pistons mounted axially with respect to the driveshaft. This arrangement, shown simplified in Figure 3, involves pistons spaced evenly around the driveshaft. The pistons are contained in a cylinder block that rotates as one with the drive shaft between the stationary swash and valve plates. The valve plate controls the flow of fluid into the cylinder volume and provides a bearing surface for the cylinder block. The swash plate provides the axial movement of the pistons as they slide over the tilted surface.

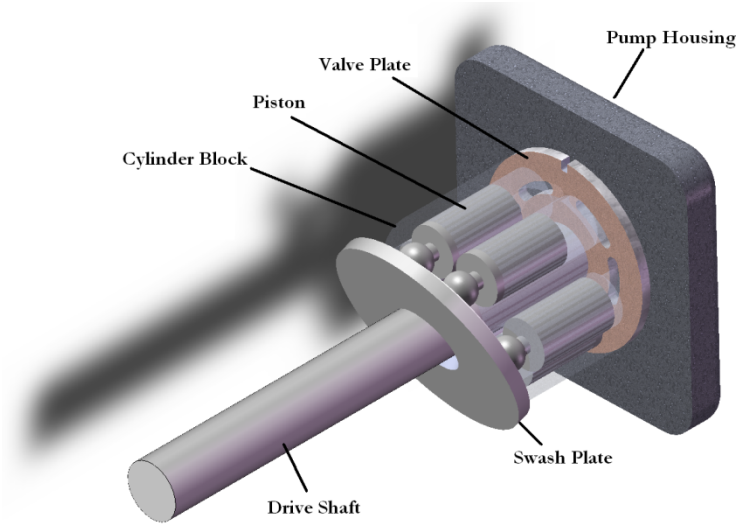


**Figure 3. Arrangement of the basic components of an axial piston pump.**

The axial piston pump works in the same manner as all positive displacement pumps. As the cylinder block rotates, the stationary angled swash plate allows the force of the fluid from the low pressure inlet to expand the chamber by moving the piston axially (Figure 4). As the cylinder block continues to rotate, the angle of the swash plate forces the chamber to reduce in volume, forcing the fluid through an outlet port. In a variable displacement pump, the distance these

pistons travel from top dead center to bottom dead center, and thus the volume displacement of the pump, depends on the angle of the swash plate.

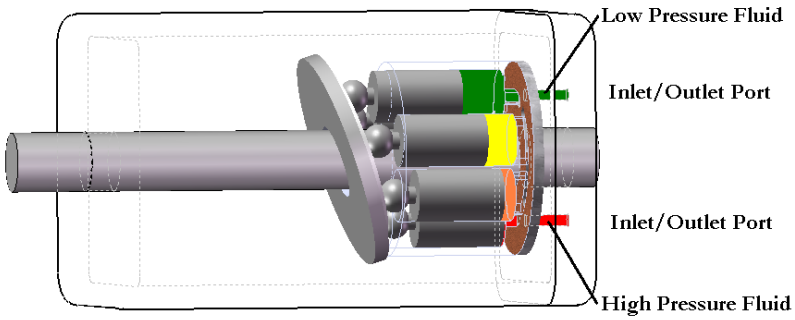


**Figure 4. Fluid flow in an axial piston hydraulic pump.**

The swash plate angle is controlled by an operator, and its angle is typically limited to 18 degrees for satisfactory mechanical operation (Akers et. al., 2006). When the swashplate is at its greatest tilt, the volume difference between the pistons over the outlet valves and inlet valves is at its maximum and the pump is delivering maximum volume. If the swashplate is moved to the zero position the volume difference is zero, resulting in no net fluid flow through the pump. Pumps of this type can reverse the flow of the hydraulic fluid by simply rotating the swashplate through the zero position. This changes which port sees the larger volume as the cylinders rotate over the valve plate so that the pumping direction is reversed.

### 2.1.3 Valve Plate and Cylinder Block System Design

The valve plate of an axial piston pump, shown in Figure 5, is a component that serves several critical tasks. The primary design of the valve plate is that of a thrust bearing. It must provide a bearing surface on which the cylinder block can rotate with minimal friction and wear. The valve plate must also deform to the cylinder block to provide a crude sealing surface that prevents leakage between the high and low pressure ports. The valve plate must do this while allowing fluid to flow efficiently into the cylinders on the low pressure side and out of the cylinders on the high pressure side.

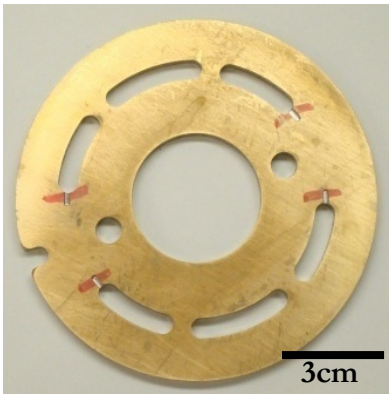


**Figure 5. The valve plate from an axial piston hydraulic pump.**

The valve plate is designed to remain stationary within the pump to provide a sliding surface for the cylinder block. It therefore has keyways to retain its position and an open center through which the driveshaft of the pump passes unimpeded. In order to reduce friction between the cylinder block and valve plate, the valve plate has what is known as a circumferential recess design (Khonsari, et.al. 2001). In this arrangement, hydrostatic lubrication is provided through kidney-shaped, recessed ports in the surface, as shown in Figure 6. These ports allow hydraulic fluid to create a hydrostatic film between the valve plate and cylinder block. The system pressure maintained on the low and high pressure side partially support the load of the cylinder block. In the case of the piston pump, the design of the kidneys is also such that fluid can flow through the pump efficiently without undermining structural integrity of the plate.

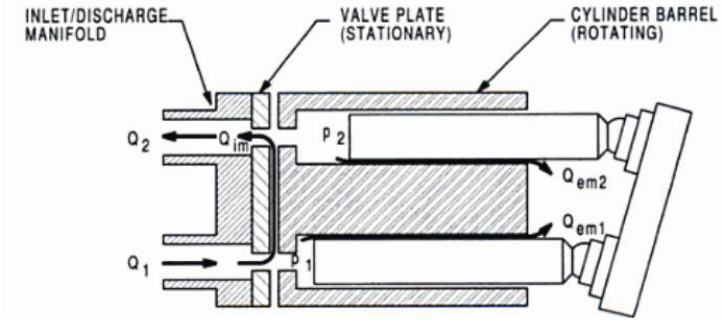


**Figure 6. Fluid leakage paths in an axial piston hydraulic pump. (Akers et. al., 2006)**

## 2.2 Tribological Systems and Engineering for Wear

As part of its critical function, the valve plate must provide a bearing surface on that the cylinder block can rotate with minimal friction and wear. In order to design for these conditions, the engineer must consider not just a single material but the assortment of components and environmental conditions making up a tribological system. This system must take into account the properties of the mating surfaces, their interaction, and their surroundings. The tribological system consists of variables including load and sliding speed (PV factor), third party wear particles, lubrication, and environmental conditions such as moisture, contaminants, temperature, and corrosives. In order to design the best system to cope with all of the variables, it is important to know and understand the wear mechanisms that can lead to failure. Proper selection and design of lubricants, components, and materials is critical to creating an effective tribological system.

### 2.2.1 Wear Mechanisms and Classification

The aim of bearing design is to reduce the friction and increase the wear resistance of the bearing material as well as part that is sliding against it. Within the context of the axial piston pump, an important tribological system is the lubricated interface between the cylinder block and the valve plate. In this system, wear may occur by contact with the mating surface or by interaction with the hydraulic fluid. Wear can occur by many mechanisms that are categorized in various ways by different authors. Zum Gahr uses a major classification system for the possible wear modes, including fluid related wear, as shown below in Figure 7 (Zum Gahr, 1987).

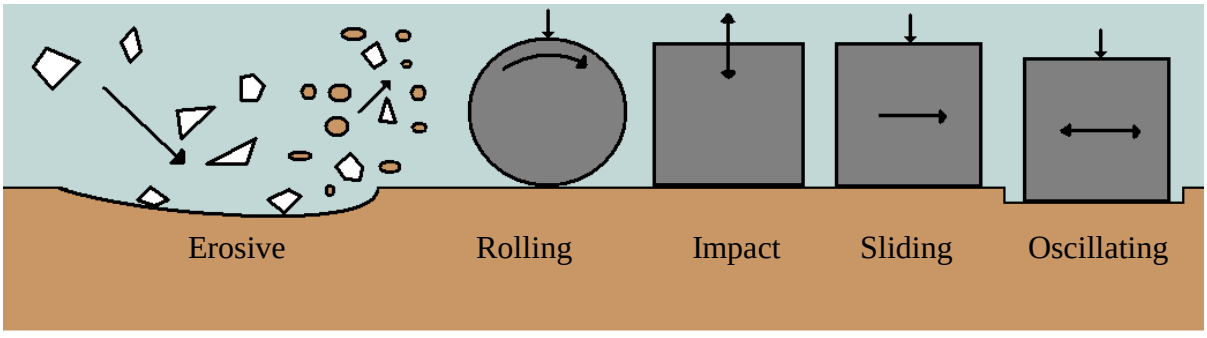


**Figure 7. Classification of wear types by wear modes.**

In the case of the interface between the cylinder block and valve plate, it can be reasoned that sliding wear will be the dominant wear mode as their relative rotation velocity is high. Bisson categorizes the forms of contact wear as adhesion, abrasion, surface fatigue, corrosive, and a special case known as fretting (ASTM, 1969). Fretting involves two surfaces in contact that are designed to be fixed but actually undergo small relative displacements caused by oscillating loads. This is of little relevance to the current situation and will not be discussed in detail. The remaining four may all play a role in the valve plate/cylinder block tribological system.

Theories of friction and wear have been in a constant state of development, with many researchers contributing to the work. These theories are based upon the fact that although surfaces may be defined as being macroscopically smooth, there are asperities on nearly every surface that play a vital role in both friction and wear. They are generally 0.1μm to several microns in size, and it is the tips of these asperities that support the load on the surfaces (Lansdown et. a., 1986). An example of these asperities is shown in Figure 8. While the bronze surface (left image) appears smooth macroscopically, in reality the surface appears as shown in the right image when viewed under high magnification.

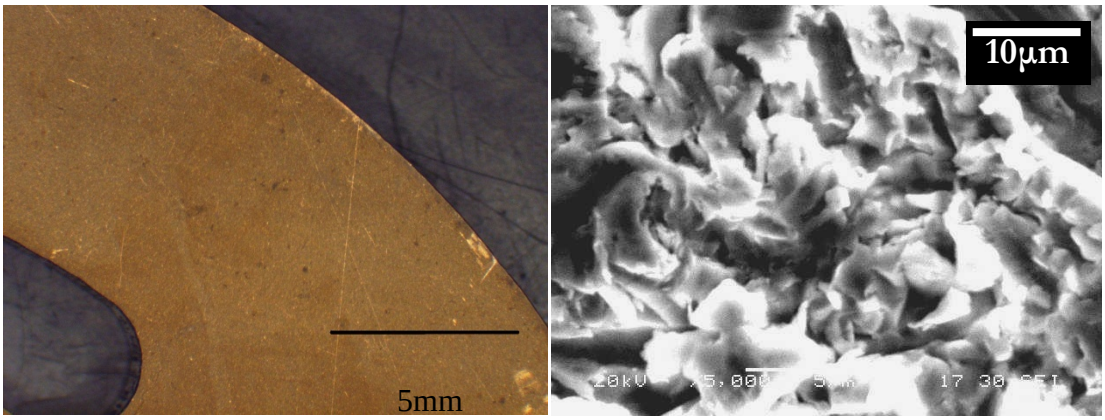


**Figure 8. Asperities on a macroscopically smooth surface.**

The tips on the surface represent a small fraction of the overall surface area, giving rise to the concept of "real" area of contact. Under a light load, only the tips of the asperities contact (Figure 9), creating a contact area that is significantly smaller than the macroscopic dimensions of the contact area. The stress created by the load applied is significantly magnified by the true area of contact, so much so that the asperities are quickly loaded beyond their yield stress (ASTM, 1969). The resulting plastic deformation exposes "clean" material that, when combined

with the increased pressure at the tips of the asperities, means that the material is likely to adhere or microweld at the contact point. The system will reach a sort of equilibrium of deformation when the real contact area is increased sufficiently by the deformation of the asperities. This is helped along by the increased number of asperities coming into contact as the original asperities deform plastically.

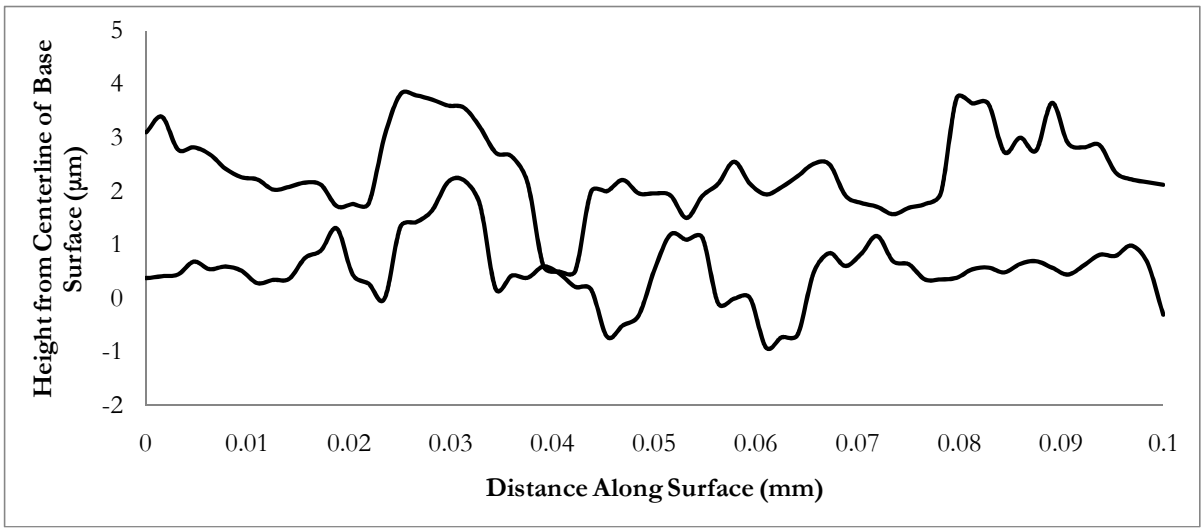


**Figure 9. Profile of the surface in Figure 8 in contact with surface of similar roughness.**

Subsequent relative movement of the faces will cause the joined asperities to shear and new junctions to form. If the force of adhesion between the two surfaces is less than cohesion, the connection will shear at the microweld and the two surfaces will remain relatively unchanged. On the other hand, if the cohesion that is less than the adhesion at the junction, the shearing can occur at the base of one of the asperities. This would result in material from one surface being transferred to the second, a process known as adhesive wear. In practice this occurs more frequently than would be expected even though the interface between the asperities typically contains contaminants, oxidation, and mismatched crystal or grain structure that would normally lead to poor adhesion (Lansdown et. a., 1986).In reality, shear often occurs very close to the original interface but not at it, thus transferring a small amount of material from one surface to the other. This is not to say that contaminants do not have an influence on adhesive wear. Solids (e.g. oxide films), liquids (e.g. lubricants), and even gases (e.g. adsorbed oxygen) can significantly reduce the friction between a sliding pair (ASTM, 1969).

For those cases where material is transferred, two things may happen with that material. The first is that the adhered material is knocked off by further contact by the opposing surface and becomes a loose wear abrasive. This is aided by fatigue as the asperity is repeatedly contacted by, adhered to, and sheared from in the sliding pair. The second situation that may occur upon material transfer is that the relocated material can remain firmly attached to the mating surface. In some situations, this exacerbates adhesive wear by providing a mating surface that is similar to its counterpart and thus has a strong affinity for it (Lansdown et. a., 1986).

An alternative interaction of asperities gives rise to what is known as abrasive wear or cutting wear. According to Bisson, the two are essentially the same, but cutting wear typically occurs when the asperities of one surface are harder than those on the mating surface (ASTM, 1969). If the toughness of these asperities is sufficient, they may then cut or plow through the softer mating material. Tribological pairs where the sliding surfaces possess similar hardness can still display abrasive wear, especially those that are relatively hard and brittle. In this case, the removal of asperities is primarily a function of the transmission of stresses and the properties of the specific asperities involved (Lansdown et. a., 1986). Both of these situations describe two-body wear wherein the cutting body is an asperity on one of the surfaces. Some scenarios involve an abrasive medium between the surfaces of the mating pair, a situation that Bisson describes as abrasive wear. The particles create what is known as three-body wear, and can originate from several different sources. In the context of hydraulics, they can be dust and grit in the hydraulic system, wear debris from other components, or from the valve plate/cylinder block tribological system itself. Damaging wear debris can be created within the tribological system by several mechanisms; particles may be broken free from a hard mating surface, ductile wear debris from a surface can be work hardened until it is sufficiently hard enough to become an abrasive, or corrosive wear products may be produced that contribute to wear. (Lansdown et. a., 1986; Zum Gahr, 1987).

Whether it is two-body or three body, the wear in these situations is characterized by material removal from the surface by a cutting or plowing-type action that results in a machined, scored, or grooved appearance. The various interactions the asperities or abrasive particles can have with the opposing surface are shown below in Figure 10.

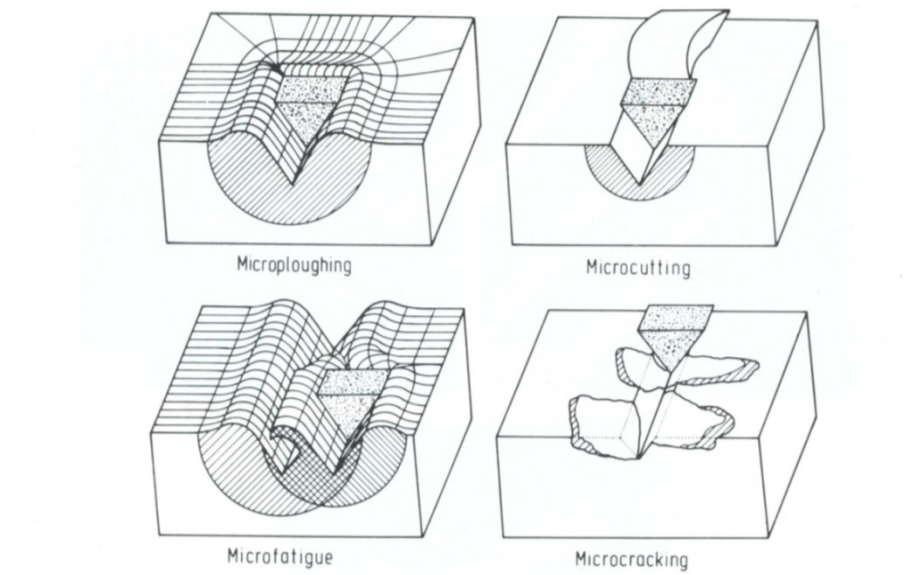


**Figure 10. Physical interactions between abrasive particles and surfaces (Zum Gar, 1967)**

The first of these interactions, microplowing, does not create wear debris by itself, instead displacing material by plastic deformation. However, two slightly offset asperities traveling through the same area repeatedly can cold work the material between them, causing microfatigue. This may eventually lead to the creation of a free wear particle of relatively high hardness as a result of that cold work performed on the material before it releases from the surface. The hardness of this debris can reach a point at which it is harder than bulk material of either surface. Particles can then become embedded in the softer surface and form a cutting tip that will wear the opposing one, further increasing wear.

Microcutting is another form of abrasive wear where material is removed, as the name suggests, in a cutting manner. This mechanism of wear in a ductile material such as steel or bronze results in wear debris similar to machining swarf, especially at low temperature (Lansdown et. a., 1986). At higher temperatures, the resultant wear debris may take on a partially melted appearance and may reattach to the surface (Lansdown et. a., 1986). In brittle materials, wear debris is generated in the form of chips or chunks generated by local fracture as the asperity moves along the surface. The resulting particles are especially detrimental to the wear resistance of the system as their sharp, rough edges make them more abrasive. Their lack of ductility also makes it difficult for the particles to deform and adds to their destructive nature.

These types of specific properties associated with wear particles have significant effects on wear and this must be accounted for in the design of the tribological system.

In addition to adhesion and abrasion, a third surface wear mechanism can produce wear debris in significant amounts in some systems. Corrosive wear is, by definition, the reoxidation of a worn surface (Lansdown et. a., 1986). There are times when this is a desired outcome such as when the oxidation forms a protective film that reduces the rate of loss of material. This is particularly true of lubricated situations where it is required for the action of extreme pressure or load carrying additives in lubricants. (Zum Gahr, 1987; Simons, 1972). The undesirable version of corrosive wear arises when the corrosion is actively removed by another wear mechanism such as abrasion. The repeated sequence of removal of the freshly corroded surface can increase the wear rate by several orders of magnitude (Summers-Smith, 1994). This mechanism of wear can be present in hydraulic systems, especially with older or contaminated oil where the environment is more chemically reactive. The bronze valve plate can be particularly sensitive to the presence of water in the oil. While not ordinarily seriously corrosive to bronze, the semi-protective oxide/hydroxide layer is easily friable (Lansdown et. a., 1986). The subsequent removal of this layer by the sliding action of the mating surface leaves fresh material open to attack by the water and other corrosives. This process is further hastened by the increased temperatures that are common in hydraulic systems. Chemical reactions progress at a higher pace at elevated temperatures. In fact, the rate of reaction doubles for every ten degree Celsius rise in temperature (Lansdown et. a., 1986).

In contrast to the three previously described wear modes, the last remaining major instrument of wear is a subsurface mechanism. The phenomenon is known as surface fatigue because the resulting damage is affects the surface. Surface fatigue is a form of wear in which fluctuating stresses applied to the surface create cracks. The cyclic loads that drive surface fatigue can originate from direct physical contact of the opposing face, transmission through the lubricating fluid, or from cavitation of the lubricant on the surface. If the loading condition persists, the cracks will propagate as the product of fatigue - eventually resulting in a separation of material from the surface (Lansdown et. a., 1986). Initiation of these cracks does not have to begin at the surface; they may nucleate at an imperfection such as an inclusion or a pore. The resulting damage often appears as pitting once the cracks breach the surface and allow a small

volume of material to separate from the bulk. Figure 11 shows the process by which the damage is created on the surface.

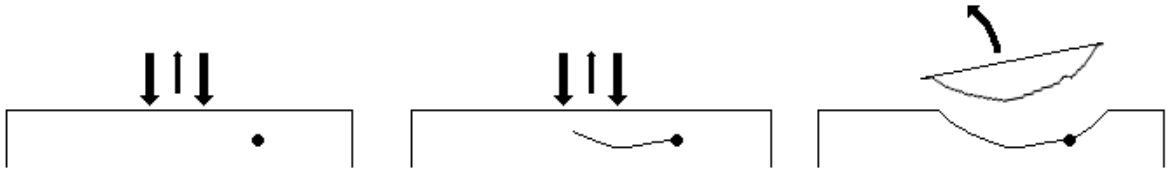

**Figure 11. Fatigue wear process.**

### 2.2.2 Lubrication

Wherever possible, lubrication is used to prevent the wear and friction that results from contact of the asperities on the opposing surfaces. The ideal case is that the peaks and valleys on each surface do not touch at all. If the surfaces are entirely separated by the lubricant, the only force required to move the component is the force required to shear the lubricant (Bannister, 1996). Not only is the force of friction eliminated, lack of contact between asperities on the mating surfaces means there is little to no wear on the materials.

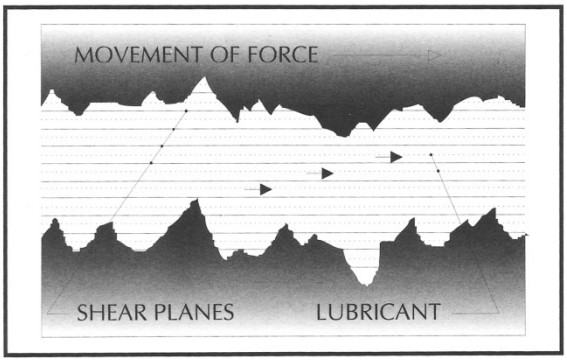


**Figure 12. Two surfaces separated by a full lubricant film (Bannister, 1996).**

The ideal case is known as full film lubrication. A supporting film of lubricant can be created in two ways. The first is a hydrostatic film. Keeping the lubricant under pressure by external means can force the sliding pair to separate (Summers-Smith, 1994). The ability to provide the necessary pressure is unusual in most bearing applications. In axial piston hydraulic pumps, hydrostatic films are possible because their very purpose is to pressurize the hydraulic

fluid that acts as their lubricant. This is essential to maintain a low coefficient of friction between the valve plate and cylinder block.

The second way to create a full film is to design the bearing to develop it by the relative motion of the two surfaces. Hydrodynamic films, as they are known, are much easier to create in bearings and are thus used extensively. The most common method is to create a restriction between the two surfaces. Generally this is done by creating a wedge shape in the bearing. Since no slip occurs between a liquid and solid, the fluid is drawn into the wedge and trapped there, increasing the pressure and lifting the surface (Summers-Smith, 1994). Axial piston hydraulic pumps also utilize this type of lubrication in areas not directly under pressure from the hydraulic fluid, including the outer edge of the valve plate.

Whether the bearing is lubricated hydrostatically or hydrodynamically, the full film supports the load of the bearing and prevents contact between the metallic surfaces. In this case, the material and surface of each half of the sliding pair are inconsequential. However, hydrodynamic fluid films are difficult to maintain. A simple way to describe the required parameters is the Sommerfield Number. The Sommerfield Number is defined as ZN/p where Z is the lubricant viscosity, N is the rotational speed of the bearing, and P is the pressure on the surface (Lansdown et.al., 1986). If the Sommerfield number is high enough for a given application, the full film condition is maintained.

In most applications it is not possible to maintain the conditions necessary to form the hydrodynamic film at all times. In axial piston hydraulic pumps, the lubricant viscosity is essentially fixed simply by the requirements of the hydraulic system. Since hydraulic systems frequently operate at temperatures of 130°C, the viscosity can be quite low, leading to a lower Sommerfield Number. In addition, the rotational speed of the interface drops every time the pump is started or stopped. This is generally infrequent in variable displacement axial piston pumps, but does present a problem. Of even greater concern in axial piston hydraulic pumps is the pressure on the bearing surface. Since axial pumps are under pressure, they can produce high normal loads on the bearing surface. Mechanical imbalances in the rotating cylinder block, including those arising from the varying piston heights, can apply further loading to the bearing surface.

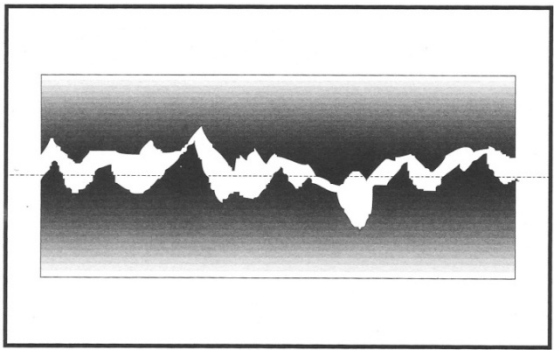

**Figure 13. Two surfaces in boundary lubrication (Bannister, 1996).**

When conditions like these decrease the Sommerfield Number enough, fluid film lubrication breaks down (Pugh, 1973). The interface transitions to what is known as boundary lubrication as shown in Figure 13. In boundary lubrication, the surfaces of the material are close enough that contact begins to occur between the asperities. There is still lubrication present, but it is trapped in the valleys of the surfaces and contact between the metal surfaces can still occur so the friction level increases sharply as shown in Figure 14. (Bannister, 1996). In addition to the general loss of the lubricating film, the ability of the lubricant to dissipate heat is also decreased. As the heat build-up increases, the effect of wear mechanisms is increased. Higher temperatures increase adhesive wear, increase abrasive wear in sliding pairs with differing hardnesses by increasing their relative hardnesses, and increase fatigue wear, especially in multilayered bearings.

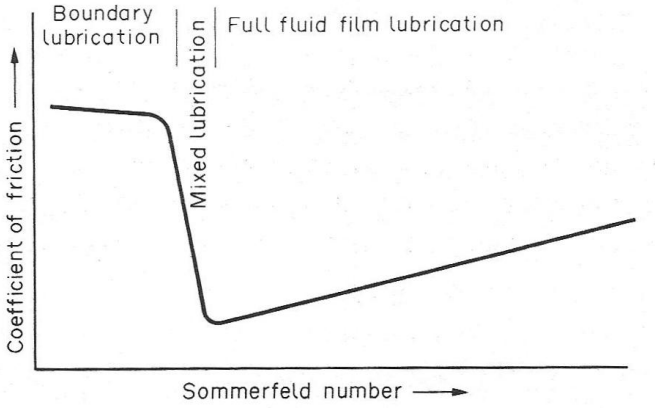


**Figure 14. Relation between friction and Sommerfield Number (Lansdown, 1986).**

### 2.2.3 Material Selection to Resist Wear

According to Lansdown, it is important to identify the cause and nature of the wear before selecting a material to improve the system. Lansdown simplifies the more than thirty classifications to seven categories that promote the selection process. Each of these categories is derived based on an easily recognized wear situation and clear guidance can be given with regards to the appropriate wear resistant materials (Lansdown, 1986). The categories are: sliding wear, fretting, three-body abrasion, gouging wear, low stress abrasion, erosion, and corrosive wear. The first category, sliding wear, is most representative of the wear likely to be present in axial piston hydraulic pumps. It is broken into two subcategories. The first is adhesive wear that is apparent when at least on one of the surfaces has a welded or torn appearance, or has a melted, wiped, or smeared appearance. The second is abrasive wear that is usually found in applications where one surface is harder than the other. It is evident when the softer material has scratch or score marks that correspond to the roughness on the opposing face.

To resist adhesive wear, Lansdown suggests using dissimilar metals, using harder materials, surface coatings, and more readily oxidized materials. A chart showing summarizing research of metal compatibility is shown in Figure 15.

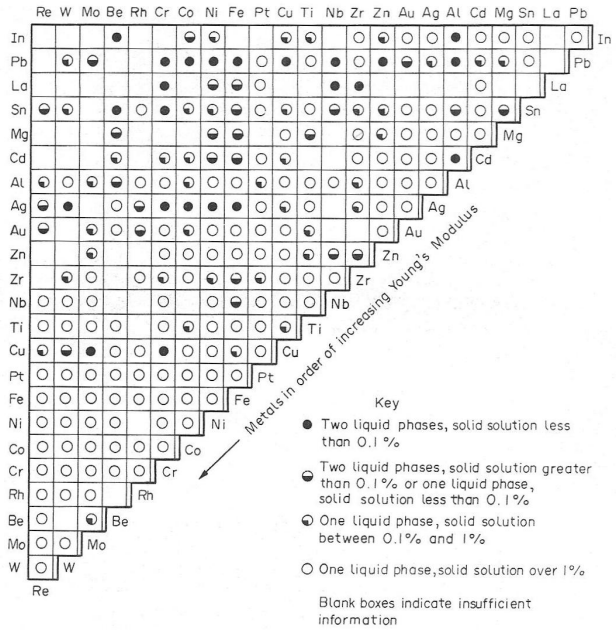


**Figure 15. Materials to resist adhesive wear (Lansdown, 1986).**

Abrasive wear, subcategorized as plowing or cutting wear, occurs when a hard asperity plow or cuts through a softer material. Avoiding abrasive wear requires two things, decreasing the roughness of the harder material and increasing the hardness of the softer metal (Lansdown, 1986). The most common situation for abrasive wear is in lubricated systems where the less critical component is the sacrificial surface and is made of a softer metal. This is generally done to "improve running-in, to embed any deleterious particles that may be present in the lubricant, and to minimize wear of the more critical component" (Lansdown, 1986). Although it would seem that the softest material would be the best for applications like these, it's been shown that the wear rate of the softer material generally decreases as its hardness approaches that of the harder surface (Lansdown, 1986).

### 2.2.4 Materials For Lubricated Sliding

The materials considered suitable for lubricated sliding conditions fall into a fairly short list. It includes steels, cast irons, copper-based alloys, white metals (babbits), aluminum, and to a lesser extent zinc, silver, chromium, molybdenum, and nickel. The most common of these are the iron based-alloys (steel and cast iron), copper-based alloys (brass and bronze), and white metals (lead and tin).

#### 2.2.4.1 Iron-based alloys

Steel is one of the most common tribological metals, if only because it is the most common structural material. Steel is used for so many applications because of its high strength, high elastic modulus, and low cost. Steels are particularly useful in tribological systems where heavy loads and tight clearances are present for long periods of time. The wear resistant applications of steels are journals, gears, ball and roller bearings, tools, wheels, rails, fasteners, etc. (Bhushan, 2001).

In lubricated conditions, the most taxing conditions are in the mixed and boundary lubrication regime. Here, the hardness and surface finish of the materials determine the type and rate of wear. Steels are known for their machinability and surface finish. It is also possible to alter the hardness from ~1.0GPa to 3.0GPa, allowing the wear characteristics in boundary conditions to be dialed in (Bhushan, 2001). When direct contact does occur, the toughess of the

steel prevents significant damage. In addition, the discontinuous structure of carbon steels prevents seizure or large scale damage to the sliding face (Lansdown ,1986).

Cast irons are similar to steels in their uses, being inexpensive structural materials themselves (Bhushan, 2001). They are typically used for wheels, rails, brakes, clutches, piston rings, gears, and rollers. Depending on the microstructure, cast irons can be designed for specific wear issues. Gray cast irons with free graphite are excellent for applications where they are sliding against themselves or steel, even in unlubricated conditions (Lansdown, 1986). The free carbon forms a graphite layer between the sliding surfaces, reducing the coefficient of friction from 0.8 to 0.4 (Bhushan, 2001). In the nodular form, the grey cast irons provide excellent fatigue resistance for rolling bearings.

White cast irons contain carbides that provide high resistance to abrasive wear (Bhushan, 2001). This is further enhanced by the addition of phosphorous that forms a continuous, hard phosphide eutectic. Additions of chromium and silicon also improve the wear resistance of cast irons. The increased wear resistance of white cast irons comes with a price, however, as its low fracture toughness results in very low impact and fatigue resistance (Peterson et. al., 1980).

#### 2.2.4.2 Copper-based alloys

Alloys of copper serve well as bearing materials and are deservingly widely used. They exhibit good strength, ductility, thermal conductivity, and oxidation resistance. In lubricated conditions such as axial piston hydraulic pumps, the ability of copper alloys to conform to the opposing surface is of significance to prevent excessive loss of efficiency and create a full hydrodynamic film (Glaeser, 1992). In addition to conforming to the steel cylinder block, copper alloys work exceptionally when paired with steel in boundary lubrication conditions (Glaeser, 1992). This is due, in part, to the phenomenon known as selective transfer that occurs as the alloying elements of bronze are selectively evolved from the surface (Shpen'kov, 1995). This forms what is known as the servovite copper film – a nearly pure, oxide-free layer of copper that exhibits abnormal plasticity (Shpen'kov, 1995; Totten et. al, 2004). The copper is then partially transferred to the steel forming a low shear layer that lowers the real contact pressure. In addition, the copper film provides for effective adsorption of surface-active compounds formed

by tribochemical processes, thus providing lubrication by a polymolecular film (Totten et. al, 2004).

Alloying additions to copper have been shown to have significant influence on the wear capabilities. For instance, 10 wt. % additions of aluminum, silicon, tin, and indium result in reduced wear rate and friction (Kohsari et. al., 2001). Other additions such as zinc improve the strength of the copper. Under low loads, the oxide of brass creates a low friction sliding surface. If the loads are high enough to break up the oxide layer, however, the material is likely to fail by adhesion. This can be prevented by using a two-phase ($\alpha+\beta$) brass with greater than 37 wt.% zinc (Lansdown, 1986).

Additions of tin (usually 10-14%) to copper form the most common, and the oldest, alloy (Lunn, 1965). Bronze has been used for millennia to reduce friction and wear, starting as early as the 4th century B.C. (Lunn, 1965; Dowson, 1998; Davis, 2001). The addition of tin to copper increases the strength of the alloy. This is important when developing a tribological system against steel, so its strength must be sufficiently high. At the same time, the bronze bearing is generally used as the sacrificial surface, designed to conform to the opposing surface and any misalignment so that the contact area is maximized. The ability of the bronze to conform to the steel surface helps distribute the bearing load and assist the formation of a hydrodynamic lubrication film. As an added bonus, the addition of tin to copper strongly increases ability to adsorb active materials aiding in lubrication when the hydrodynamic film breaks down (de Gee et. al., 1971).

The strength of bronze is achieved primarily by the $\alpha$ phase matrix of copper and tin in solid solution that provides a tough support structure. Additional strengthening and hardness can be created with fast cooling rates in cast alloys. This produces a tin-rich, $Cu_{31}Sn_8$ $\delta$ phase that provides a hard, wear resistant structure distributed throughout the material (Lansdown, 1986). Thus, the microstructure of the tin bronze can be tailored to provide wear resistance against harder materials.

Other additions can be made to bronzes to increase strength and other mechanical properties. This includes aluminum, manganese, beryllium, silicon, and phosphorus (Bhushan, 2001). Aluminum bronzes (8-13 wt. % Al) are excellent for high load conditions with lubrication (Lunn, 1965). Otherwise, they become more susceptible to galling (Bhushan, 2001). Small

additions (2 wt. %) of beryllium can increase the hardness of the bronze to that of steel (Peterson et. al., 1980). This decreases deformability but makes them useful in places steels cannot be used.

A common addition made to bronze to improve its strength is phosphorus. It is also found in alloys as residual impurities from phosphor copper ($Cu_3P$) used by foundries to deoxidize the copper melt. Even the strictest standards allow for about 0.05% phosphorus content (de Gee et. al., 1971). In larger amounts, it has been shown that phosphor bronzes (up to 10% P) have lower wear rates. A stronger supporting structure created by hard particles of $Cu_3P$ increases wear resistance during sliding (Lansdown, 1986). Although phosphorous has been shown to increase wear resistance in certain applications, studies have also demonstrated that higher amounts can inhibit boundary lubrication by causing desorption of the lubricant molecules. The exact mechanism is still under debate, however it has been suggested that excess phosphorus prevents the oxidation of copper at the interface, thus decreasing the chemical potential and causing adsorption (de Gee et. al., 1971).

While many additions are made to bronze to improve its hardness and wear resistance, some additions are designed to do nearly the opposite. Additions of lead up to 40% are added to copper based alloys to increase the deformability of the alloy. Cast leaded bronze alloys take advantage of lead's near insolubility (0.003 at. %) in copper to create free globules of lead in the copper-tin matrix (Glaeser, 1992). These precipitates prevent seizure during lubrication starvation and are smeared across the surface to form a low shear solid lubricant at high sliding velocities (Lunn, 1965). When supported by the solid solution of copper and tin, this combination of the soft lead and supporting copper-tin solid solution make leaded tin bronzes a popular choice for many applications.

#### 2.2.4.3 Babbits (white metals)

Bhushan reflects a common philosophy in tribology, that is; "When a bearing system is expected to run in a state of hydrodynamic lubrication with oil, an unexpected solid contact is generated by the introduction of hard abrasive particles, misalignment, high load, or slow speed at the sliding interface." (Bushan, 2001). For these applications, a material is required that is able to deform to mitigate the damage. Soft metals such as lead and tin have been successfully

utilized to do just that because of their low strength. In addition to their ability to deform to the mating surface in this scenario, these soft alloys are able to flow or even melt to protect the surfaces from damage (Bushan, 2001).

The first of these alloys were the lead-based metals. The typical composition is 10 wt.% tin, 15 wt.% antimony, and the remainder lead. The antimony and tin form a cuboidal intermetallic in the lead structure. During solidification, this face can easily segregate in the bearing, severely reducing the fatigue strength of the alloy. In 1839, Isaac Babbitt patented tin-based alloys containing copper and antimony to refine their strength in an attempt to bridge the gap between the soft lead bearings and the much tougher bronze (Khonsari, 2001). Together with lead-based alloys they became known as babbits or white metals and are still in use today.

Tin-based babbits are generally considered superior to lead-based babbits despite their high cost. When copper and antimony are added, fine intermetallic dispersoid phases are formed that increase the fatigue strength of the alloy while having no detrimental effect on the bearing properties (Lunn, 1962). Copper is added to introduce a hard primary $Cu_6Sn_5$ intermetallic and the antimony content of the alloys is manipulated to add a secondary SbSn at antimony levels over 7.5 wt.% (Lunn, 1962). Each of these is known to increase the fatigue strength below a temperature of 130˚C (Glaeser, 1992).

# CHAPTER 3. PHASE I: EVALUATION OF PB AND BI BRONZES

## 3.1 Introduction

Sauer Danfoss is looking to replace the leaded bearings in their hydraulic pumps with an alternative because of concerns about lead in engineered applications. Specifically, they are looking to replace the Cu-10Sn-10Pb surface layer on the valve plates utilized in Series 15 and Series 40 (M46) axial piston hydraulic pumps. One of these, the M46 pump, is shown schematically in Figure 16.

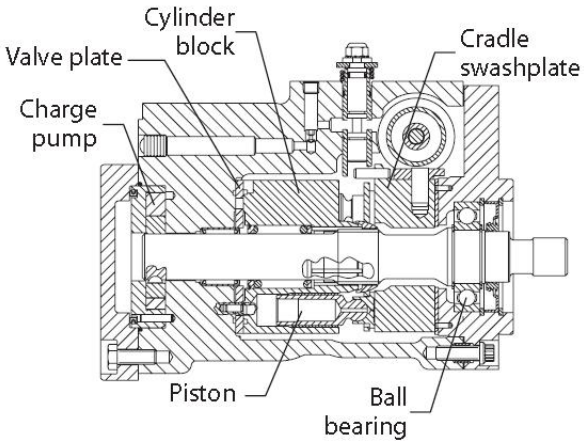


**Figure 16. Sauer Danfoss M46 axial piston hydraulic pump.**

The valve plate in the Sauer Danfoss Series 15 and 40 pumps provides a low friction sliding surface for a cylinder block comprised of a proprietary copper-infiltrated P/M steel cylinder block. The cylinder block steel is entirely pearlitic, and the composite material has a minimum apparent hardness of 89HRB. The production valve plates are comprised of low alloy steel disks with a leaded bronze cladding. The bronze is produced from water atomized, prealloyed Cu-10Sn-10Pb powder. The powder is roll-pressed onto the steel backing plate and liquid phase sintered to allow the formation of soft lead phase pockets. After sintering, the valve plates are lapped to a uniform surface finish (Ra=6.26 μm, RzDIN=6.416μm, Rmax=6.952μm, Rq= 0.817μm). In doing so, the bronze surface layer is reduced to a thickness of approximately 500μm.

While looking for alternative materials, the research sponsor chose to try a Federal Mogul designed bismuth bronze. The alloy, Cu-10Sn-3Bi (wt.%) was also produced by powder metallurgy with the direct intent to replace P/M Cu-10Sn-10Pb. The cu-10Sn-3Bi material was chosen because the composition demonstrated increased wear resistance during in-situ tests in automotive engines, along with increased fatigue and corrosion resistance after laboratory testing (Saxton, 2006). The Cu-10Sn-3Bi material was designed to take advantage of the insoluble bismuth second phase similar to the leaded bronze alloys (Saxton, 2006). There were a few changes, for instance, Federal Mogul reduced the amount of the insoluble metal from 10% to 3% in order to improve the strength of the alloy. The experimental bismuth bronze valve plates were produced using powder metallurgy by Federal Mogul. The result is a 250μm thick, Cu-10Sn-3Bi cladding on a low alloy steel backing plate, similar to the production models; however, certain aspects of the production process are unknown (Sauer, 2008).

To evaluate the valve plates with the experimental Cu-10Sn-3Bi cladding, they were run through a proprietary test in hydraulic pumps. In contrast to the Cu-10Sn-10Pb valve plate equipped pumps, those equipped with Cu-10Sn-3Bi clad valve plates failed to reach the end of the test due to significant decreases in pump efficiency (Sauer, 2008). The alloy was therefore deemed unsuitable as a replacement for the Cu-10Sn-10Pb surface layers. A study of the wear damage on each valve plate material was required to understand why the bismuth bronze failed in the axial piston hydraulic pumps. By doing this study, not only was explanation for the failure be developed, but the information was used (Chapter 4) to develop an acceptable replacement for axial piston hydraulic pumps.

## 3.2 Methods and Procedure

### 3.2.1 Sample preparation

The axial piston hydraulic pump valve plates with Cu-10Sn-10Pb and Cu-10Sn-3Bi surface layers used for this study were taken from pumps that had undergone a proprietary test procedure at Sauer Danfoss. Since the test is normally used to evaluate the efficiency and performance of the hydraulic pump, it was used to evaluate a newly developed replacement for

the production leaded bronze. The bench test ramps up the pumps in 10 minute steps from 2500 RPM at 15 MPa working pressure to 4500 RPM at 50 MPa (Table 1).

**Table 1. Test Parameters for Axial Piston Hydraulic Pump Testing (Sauer, 2008)**

| Step # | RPM | Delta Pressure (bar) | Displacement (%) | Time (min) |
|---|---|---|---|---|
| 1 | 2500 | 150 | 100 | 10 |
| 2 | 2500 | 200 | 100 | 10 |
| 3 | 3000 | 200 | 100 | 10 |
| Measure Surface Finish and Flatness | | | | |
| 4 | 3000 | 250 | 100 | 10 |
| 5 | 3000 | 250 | 100 | 10 |
| 6 | 3500 | 310 | 100 | 10 |
| Measure Surface Finish and Flatness | | | | |
| 7 | 4000 | 310 | 100 | 10 |
| 8 | 4000 | 400 | 100 | 10 |
| 9 | 4500 | 500 | 100 | 30 |

The testing protocol shown in Table 1 is ordinarily used to test the efficiency of the hydraulic pump, not to cause premature failure of the components. As such, the production pumps with the Cu-10Sn-10Pb leaded bronze valve plates routinely completed the trial without a hitch. However, when the Cu-10Sn-3Bi clad valve plates were used in hydraulic pumps, the test was halted early due to a drop in pump efficiency. Samples were retained of leaded bronze valve plates and the failed bismuth bronze valve plates for a comparative study to determine the reason for the failure. The samples included two worn Cu-10Sn-10Pb leaded-bronze valve plates, an unused leaded bronze valve plate, and a samples of a Cu-10Sn-3Bi valve plate both as-manufactured and after in-situ testing. In addition to the valve plates, a mating copper infiltrated steel cylinder block surface was also obtained after being run through the test routine with a leaded bronze sample.

### 3.2.2 Evaluation methods

#### 3.2.2.1 Profilometry

A HommelWerke LV-50 (Hommel Werke-Thyssen, Germany) stylus profilometer (Figure 17) was used to determine the surface roughness of the lapped valve plates and profile

the wear tracks on the worn valve plate surfaces. Profilometry data was analyzed using Omnisurf software (Digital Metrology Solutions, Inc., Indiana, USA). Traces for roughness data were taken over a minimum distance of 10mm. Parameters for cutoff lengths were set for shortness (ls) at 2.5μm and roughness (lc) at 2.50mm.

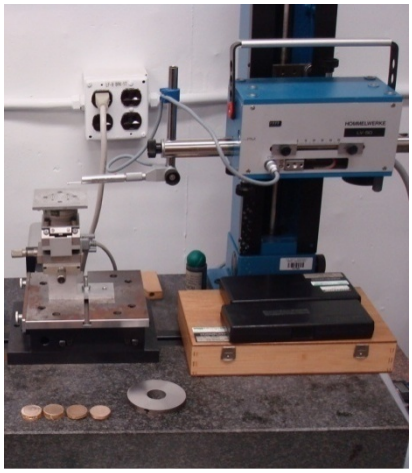

**Figure 17. HommelWerke LV-50 profilometry.**

#### 3.2.2.2 Scanning Electron Microscopy

A scanning electron microscope was used for an initial look as it provided a view of the physical nature of the wear. The SEM has a larger depth of field than optical microscopes and allowed for elemental analysis with backscattered electrons and x-rays. Using the secondary electron (SEI) and backscattered electron (BEC) capabilities of the scanning electron microscope (SEM), detailed analysis of commercial Cu-10Sn-10Pb and experimental Cu-10Sn-3Bi clad valve plates was performed.

#### 3.2.2.3 Metallography

Studying the surface of the valve plates only exposes the effect of the new valve plate material, leaving the cause for the wear behavior unknown. Development of a new material required knowledge of what effect material properties and microstructure had on the performance of the valve plate surface layer. In order to correlate the differences in wear performance to the composition, metallographic examination of the two materials was performed both optically and using the SEM. Vickers hardness tests give a measure of the

bronze prior particle strength and EDS compositional data were also used to characterize the two materials.

### 3.2.2.4 Pin on disk wear tests

To verify findings produced using scanning electron microscopy and reported in literature, pin-on-disk wear studies were conducted on chill cast Cu-10Sn-10Pb and Cu-10Sn-3Bi materials according to the standard ASTM G99-05. Chill cast samples were prepared by induction melting the alloy under 1/3 atm of argon. The melt was drop-poured into a 25.4mm diameter water chilled copper mold. After solidification, the ingots were sectioned into disks approximately 6mm thick. Each sample was polished to a surface finish matching that of the lapped valve plates. Hemispherical pins 6.35mm in diameter were electrical discharge machined and plain machined from the proprietary P/M steel cylinder block. Wear tests were then performed using the Falex ISC250PC tribometer shown below (Figure 18). Several samples of both the Cu-10Sn-10Pb and Cu-10Sn-3Bi material were tested using a 500g load on the pin and 17.5cm/s for 50m, creating a wear track 16mm in diameter.

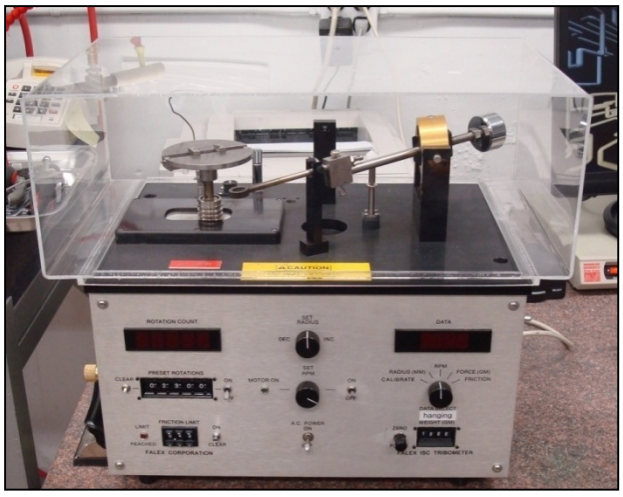


**Figure 18. Falex ISC250PC pin-on-disk tribometer.**

## 3.3 Results

### 3.3.1 Unworn Valve Plates

Prior to their application in hydraulic pumps, the surface of each the valve plates was lapped for flatness and surface finish that are each critical to pump operation. In the unworn condition, the surface of each material (Figure 19) appeared as a uniform distribution of asperities, the result of being lapped to a consistent surface roughness.

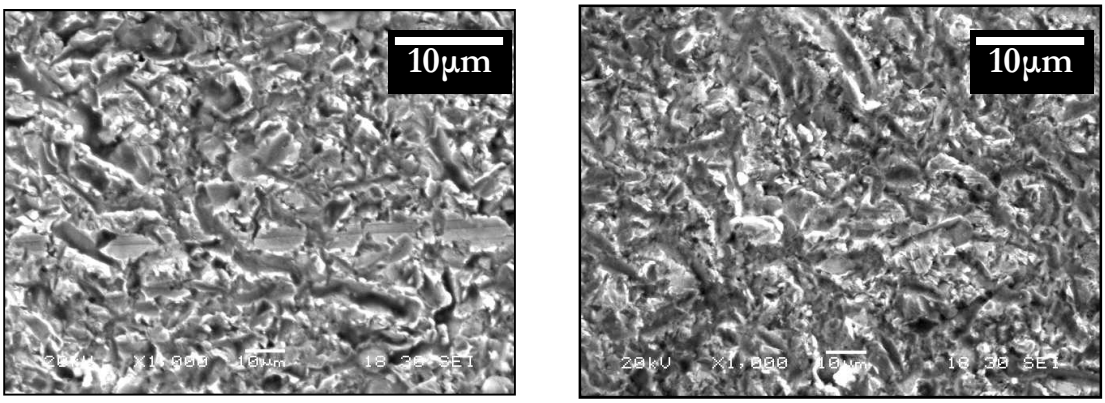


(a) (b)

**Figure 19. Surface condition of an unworn a) leaded and b) bismuth bronze valve plate.**

The surface roughness of each valve plate was measured with a profilometer to acquire a nominal roughness value for the valve plates that could be used to create lab specimens with the same surface properties. A typical primary and waviness profile is shown below in Figure 20. Analysis of multiple profiles resulted in a roughness measured as: Ra=6.26 µm, RzDIN=6.416µm, Rmax=6.952µm, Rq= 0.817µm.

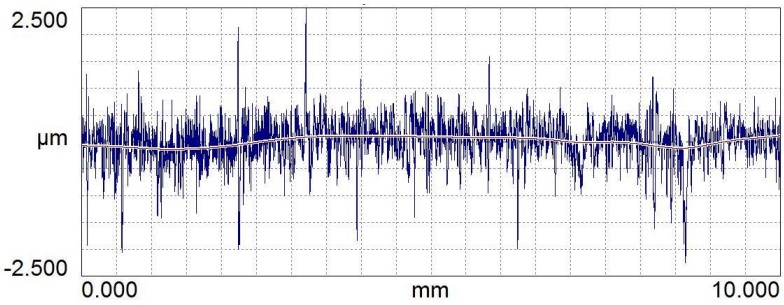


**Figure 20. Surface profile of a lapped valve plate.**

### 3.3.2 Characteristic Macroscopic Wear Pattern

Valve plates that had been used in axial piston hydraulic pumps had a characteristic wear pattern derived from the design of the pump. This was also true of the valve plate samples that were run through the previously described proprietary test procedure. These valve plates had an appearance exemplified by the leaded bronze valve plate shown in Figure 21 after being run through the test procedure.

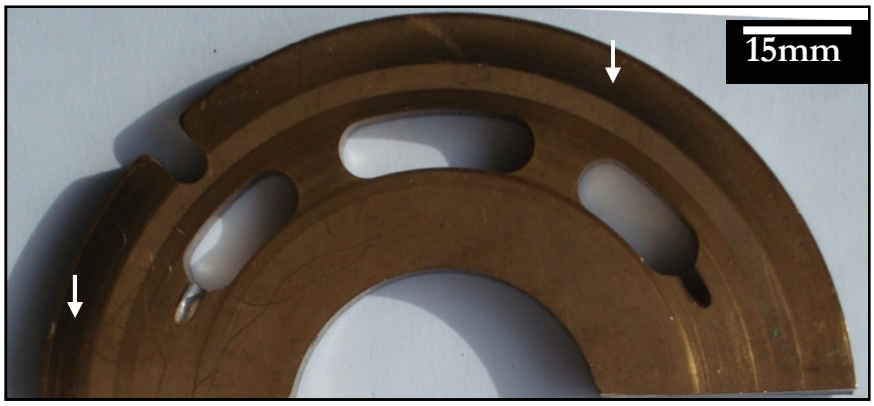


**Figure 21. Half a worn valve plate showing a representative wear pattern.**

Contact between the cylinder block and valve plate must be tight enough to create a sealing surface between the low and high-pressure sides. Preserving this pressure differential is required to preserve efficiency. However, having the entire cylinder block face in contact with the valve plate would cause greatly increased friction and make for an inefficient pump. In order to reduce power loss at the cylinder block and valve plate interface, the contact area is limited to two rings on the cylinder block face known as "balance lands" indicated with white arrows in Figure 22a.

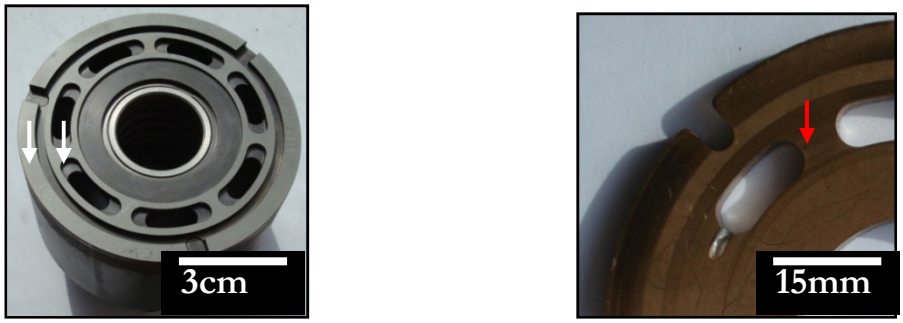


(a) (b)

**Figure 22. The mating surfaces of the a) P/M cylinder block and b) P/M valve plate.**

The inner balance land (right arrow in Figure 22a and red arrow in 22b) on the cylinder block encompasses the kidney-shaped ports of the cylinders that correspond to the similarly shaped low and high pressure inlets on the valve plate. At the inner balance lands, the valve plate acts as a thrust bearing with a circumferential recess design. At rest, the system pressure maintained in the hydraulic circuit creates a hydrostatic film of oil at the balance land that partially supports the cylinder block. Regions under hydrostatic lubrication are subject to lower amounts of wear since the surfaces are never in direct contact during operation. Wear at the inner balance land results only from contact with the largest of the asperities on the cylinder block surface. In fact, some regions of the inner balance land on the valve plate are indistinguishable from the areas of the valve plate untouched by the cylinder block.

The outer balance land (left arrow in Figure 22a and dark outer ring on Figures 21 and 22b) is not supported by a hydrostatic film of oil. Instead, the motion of the cylinder block creates a hydrodynamic film under the outer balance land with oil that leaks from the inner balance land. The worst wear conditions coincide with the hydrodynamic lubrication regions of the valve plate-cylinder block interface. This portion of the interface experiences the highest sliding speeds, lubrication starvation, and increased normal loads. The hydrodynamically lubricated outer balance land is the region where the Cu-10Sn-10Pb and Cu-10Sn-3Bi clad valve plate showed a marked difference in appearance after the bench tests in hydraulic pumps (Figure 23). The surface of the bismuth bronze (Cu-10Sn-3Bi) clad valve plate (Figure 23b) showed much greater surface damage than the leaded bronze plate (Figure 23a).

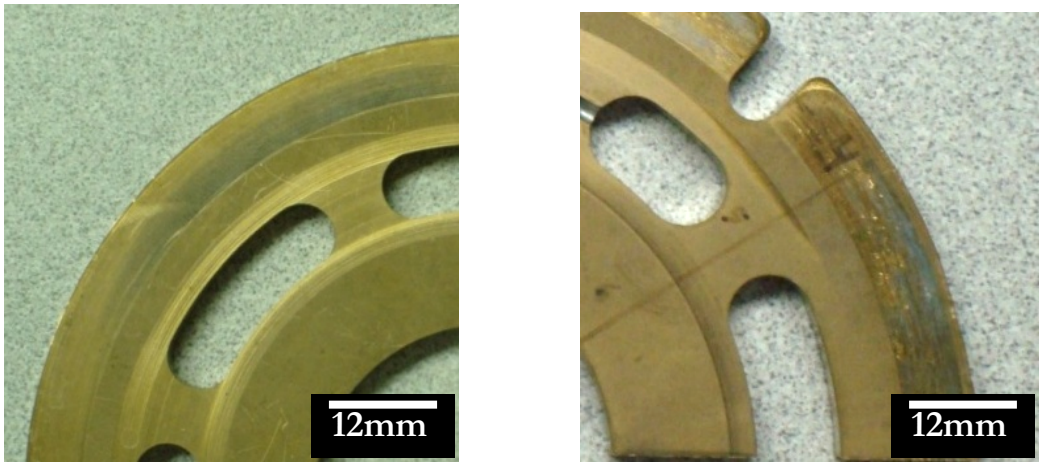


(a) (b)

**Figure 23. The as-worn appearance of the a) leaded and b) bismuth bronze valve plates.**

### 3.3.3 Optical Microscopy and SEM Analysis

The region of most interest on the valve plates is the outer balance land, where the hydrodynamic lubrication leads to the most pronounced wear. Analysis of this particular region is representative of the worst conditions the material is likely to experience. Along the outer wear band, the damage varies in intensity around the circumference, which is visible in Figure 21 as a darkening of the surface over portions of the valve plate (white arrows) for the leaded bronze surface. The transition between these regions is evident (Figure 24) optically, and the difference in surface morphology became more apparent under higher magnification (Figure 25).

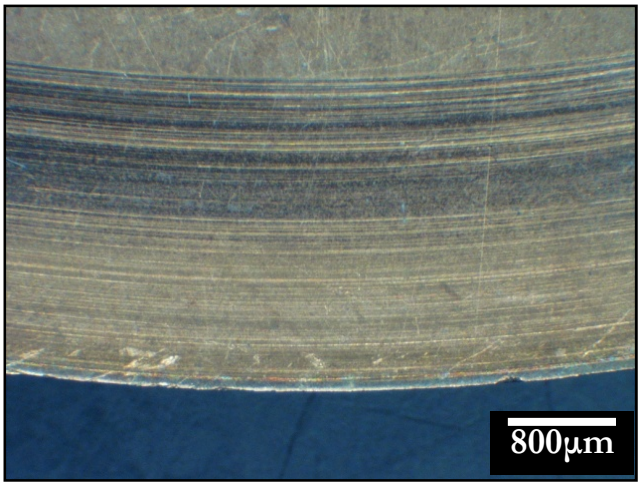


**Figure 24. Light to dark region transition on the leaded bronze outer balance land.**

The two optically contrasting surfaces shown in Figure 24 both exhibit the same continuous, circumferential score marks in the direction of rotation (Figure 25) as were noted at the inner balance land (not shown). These wear tracks again indicated abrasive wear by asperities on the mating surface of the P/M steel cylinder block. However, the change in color between the two regions was the result of drastically differing degrees of plastic deformation. This was the result of additional normal forces arising from a tilting moment on the rotating cylinder block and pressure variations within the pump.

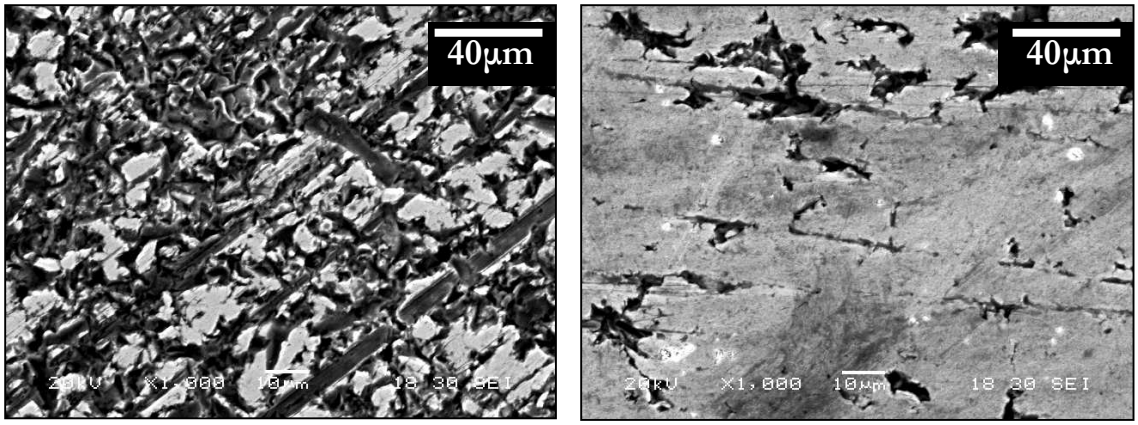


(a) (b)

**Figure 25. a) Light and b) dark areas in the leaded bronze outer balance land.**

The wear damage shown on the leaded bronze surfaces was present under normal pump operating conditions, such as those of the bench test, and was not an indication of failure. In fact, much the plastic deformation was created during the "break-in" period of pump operation where the bronze valve plate conforms to the cylinder block, reducing leakage and optimizing pump efficiency. The valve plate shown in Figures 21, 24, and 25 above is a representative sample of leaded bronze plates that pass the testing procedure.

In contrast to the leaded bronze valve plates, the Cu-10Sn-3Bi bismuth alloy valve plates did not pass the hydraulic pump bench tests. The valve plates showed a similar overall pattern of wear arising from the design of the pump. Under hydrostatic lubrication at the inner balance land, the Cu-10Sn-3bi valve plates showed wear behavior (Figure 26), comparable to the Cu-10Sn-10Pb valve plate (Figure 25a).

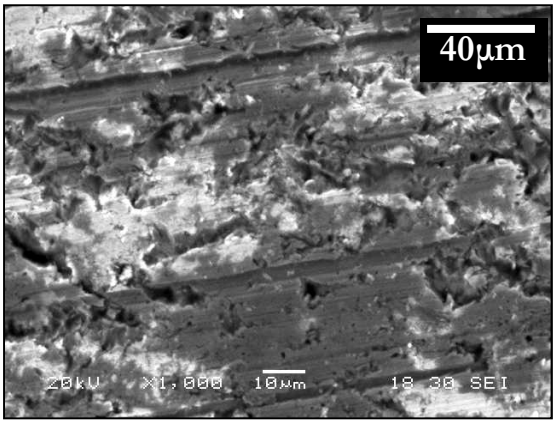


**Figure 26. Wear morphology of the inner balance land of the Cu-10Sn-3Bi valve plate.**

The wear morphology of the outer balance land (Figure 27) showed a significant departure from the wear damage found on the leaded bronze valve plates (Figure 25). The evidence for the poor performance of the Cu-10Sn-3Bi material is present in the hydrodynamically lubricated regions of the valve plate and cylinder block interface where elevated sliding speeds and increased normal pressures at the outer balance land apparently resulted in lubrication starvation and a pronounced temperature rise.

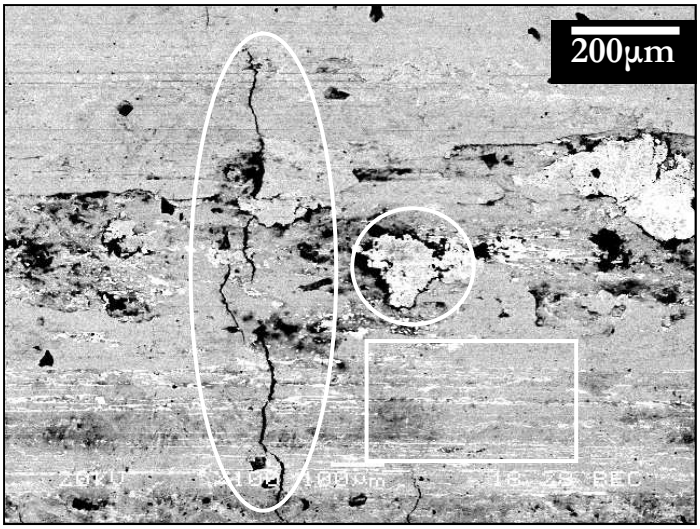


**Figure 27. Backscattered BEC micrograph of the outer balance land of the Cu-10Sn-3Bi.**

At the outer balance land of the Cu-10Sn-3Bi valve plates, the surface displayed three distinct damage phenomena. The first was radial cracking (white oval, Figure 27) perpendicular to the sliding direction, indicating the material may have been put in tension by intermittent contact by the mating surfaces. Second, plateaus of material partially separated from the surface by fractures were visible (white circle, Figure 27 and highlighted in Figure 28), again indicating possible adhesion between the two sliding surfaces.

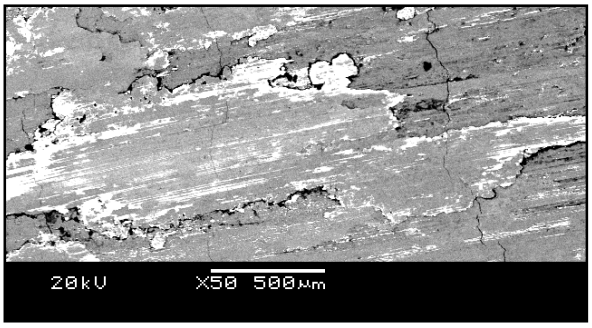


**Figure 28. Secondary (SEI) image of bismuth rimmed fractures on the outer wear track.**

The third failure phenomenon was identified by the appearance of the soft bismuth phase (white rectangle, Figure 27, highlighted in Figure 29) that appeared to have been drawn out of the surface pockets and spread across the surface in a discontinuous fashion along the sliding direction. The bismuth appeared to be present on the surface as a resolidified phase, suggesting that it reached its melting point when the pump was in operation. Furthermore, the shape of the solidified metal suggested that it partially wet on the bronze substrate.

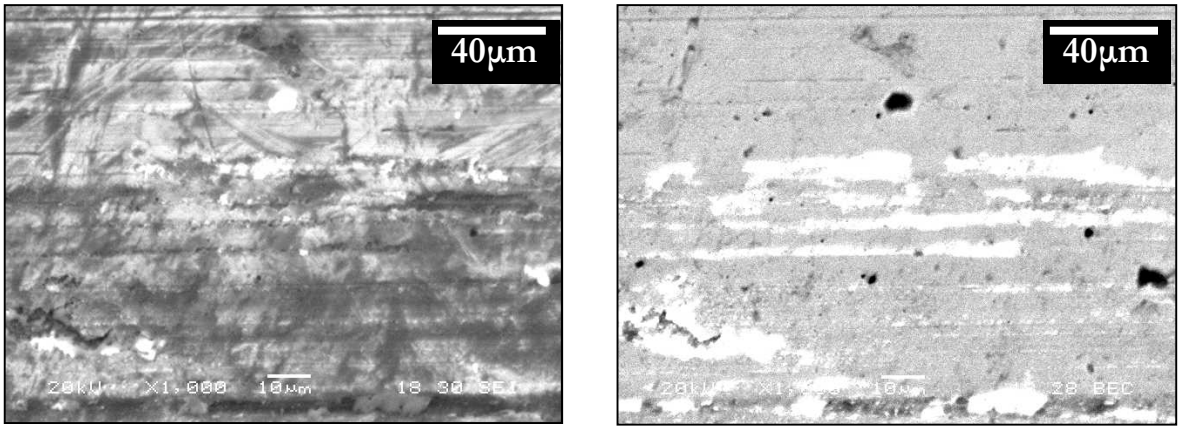


(a) (b)

**Figure 29. a) SEI and b) BEC images of smeared soft bismuth on the outer wear band.**

### 3.3.4 Quantitative Metallography

Metallurgical analysis of the valve plates was necessary to explain the variation in wear response for the two valve plate materials. The nominal microstructures of each material (Figure 30) have a significant difference in appearance after an identical etch. The leaded bronze (Figure 30a) shows a visible variation in the color of the grains, with two or three distinct color changes including heavily twinned darker grains. In contrast, the bismuth bronze has a moderate amount of twinning and fairly consistent color from grain to grain.

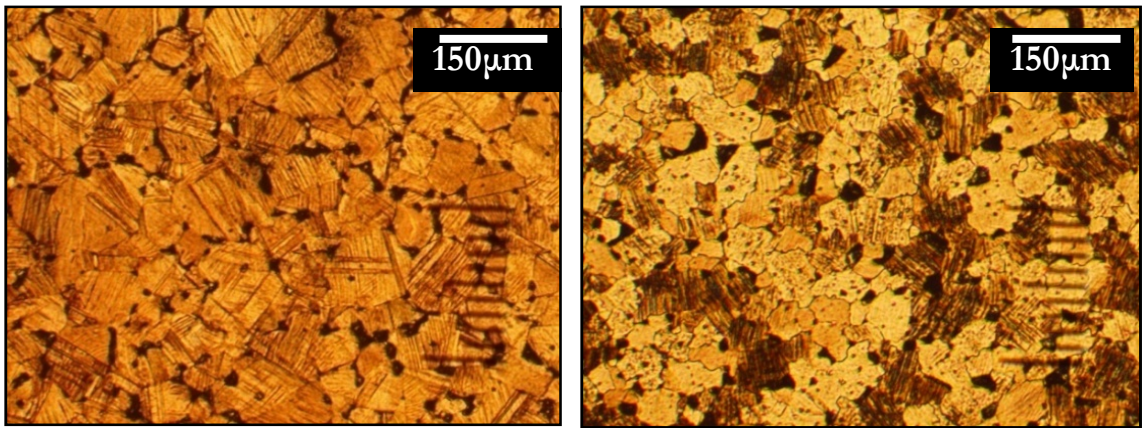


(a) (b)

**Figure 30. The a) bismuth bronze and b) leaded bronze after FeCl etch at 50x.**

Vickers hardness tests were performed to determine whether differences existed in the hardness between the various grains of the two materials. Within the leaded bronze sample, the dark grains averaged a Vickers hardness of 133 using a 100g load (HV0.1) and the light grains averaged 122 HV0.1. Thus, the dark and light grains in the leaded bronze showed a slight difference in hardness on average, but not enough to indicate a significant difference in structure or composition of the copper. Outliers in both samples overlap, indicating little statistical difference in the hardness values between the grains. The hardness of the leaded and bismuth bronzes were also similar, as the hardness of the random grains in the bismuth bronze averaged 131 HV0.1. Therefore, a difference in hardness likely can be eliminated as a cause of the failure of the bismuth material.

Subsequent study of polished and etched samples using a scanning electron microscope revealed that the difference in optical coloration of the grains was not due to chemistry. EDS results verified that the composition of the light and dark grains in the leaded bronze was around 88.6% Cu and 11.4% Sn (wt%), and that the uniform grains in the bismuth bronze were 88.9% Cu and 11.1% Sn (wt%).

Careful matching of SEI images with optical micrographs showed that the grains that appear optically dark do so because of the orientation of the slip planes. The dark color arises when they have the orientation indicated with the right arrow in Figure 31, i.e. when the twins are visible edge on. Those grains that appear light colored have the orientation shown with the left arrow in which the twins are visible end on.

SEM images of the bismuth bronze showed a more random orientation of grains due in part to the significant multiplication of annealing twins within the prior particles. The pattern of slip planes, and thus dislocations, exposed by the polish and etching results in the moderate coloring seen with the optical microscope in the bismuth bronze (Figure 30a). The average hardness of these grains in the bismuth bronze falls between the light grain and dark grain leaded bronze hardness values, which agrees with the correlation observed between slip plane orientation and optical color.

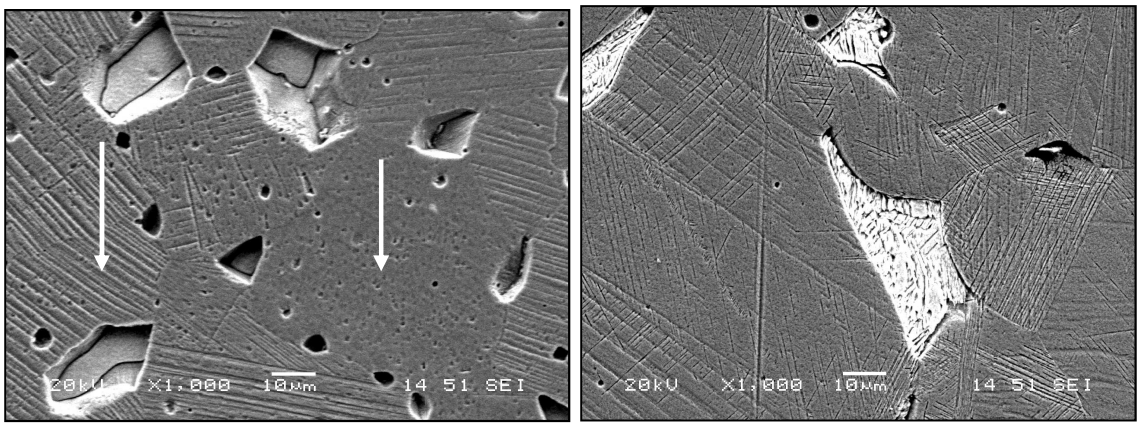


(a) (b)

**Figure 31. SEM image of the a) leaded bronze and b)bismuth bronze grain structure.**

To further characterize the P/M material, particle size measurements were performed using the line-intercept method. The bismuth bronze material is comprised of prior particles approximately of 53µm in diameter, slightly larger than the 37µm average for the leaded bronze. However, the difference in grain size is most likely not large enough to be the primary cause of the contrast in wear characteristics.

The distribution of the solid lubricant phase in the valve plates (Figure 33a) is similar in the two materials. Although the leaded bronze material contains 10% lead by weight, backscattered electron images show that the soft phase pockets comprise 4.75-5.5% of the structure by volume. In contrast, the bismuth bronze contains 3% bismuth by weight that accounts for 3-3.5% of the alloy by volume.

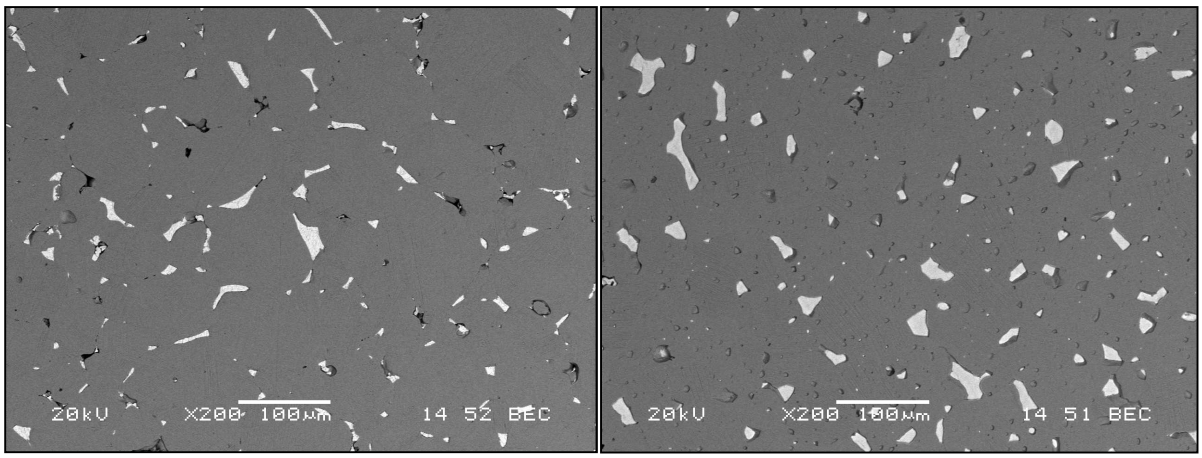


(a) (b)

**Figure 32. The a) bismuth bronze and b) leaded bronze soft phase distribution.**

The similar densities of lead and bismuth should result in similar weight percent to volume percent ratios. The disparity may arise from the processing technique. It is known that the leaded bronze alloy was produced from pre-alloyed Cu-10Sn-10Pb powder and liquid phase sintered to allow the lead to form the soft phase pockets. If this was not complete, some lead may still be trapped within the bronze prior particles, resulting in a lower visible volume fraction. If the bismuth bronze material was produced using Cu-10Sn powder that was blended with elemental bismuth powder, the volume fraction would be closer to theoretical.

Differences in the distribution of the soft phases also suggest possible differences in processing between the two alloys. In the leaded bronze (Figure 33), lead is found most commonly at the triple points (white arrows). Also of significance are small globular lead pockets within the grains (e.g. black arrow). The lead pockets at the grain boundaries are expected from lead segregating to these regions during partial melting with fairly poor wetting. This agrees with the established manufacturing process of liquid phase sintering of the leaded bronze powder.

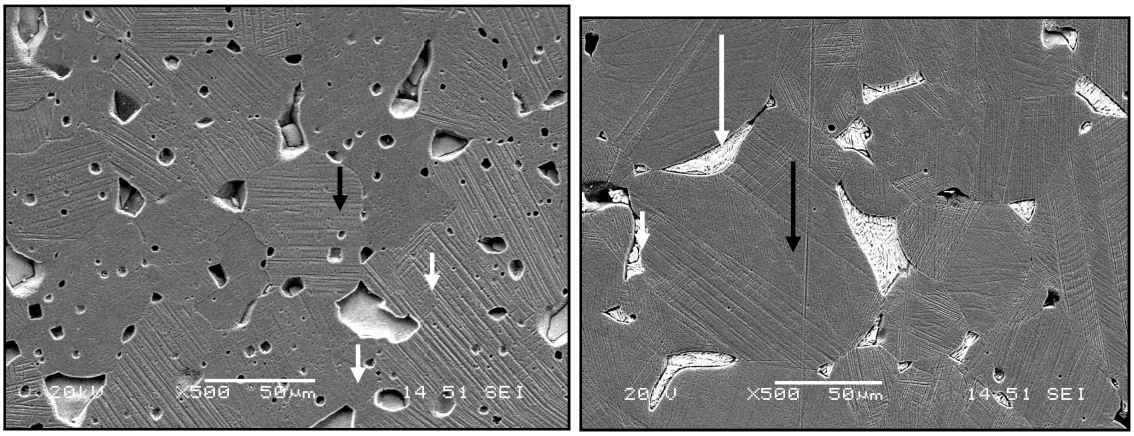


**Figure 33. Distribution of a) lead and b) bismuth in the bronze valve plates.**

The bismuth bronze (Figure 33b) alloy differs from the leaded bronze in that the soft phase is not found within the grains, an indication that bismuth was added as a blended elemental powder. In many places, the bismuth is found along the grain boundaries, as indicated with a white arrow. When the material is found at the triple junctions (black arrow), it appears to trace further along the grain boundaries, hinting at increased wetting during liquid phase sintering.

The solid lubricant phases themselves appear significantly different from each other after etching. As shown in Figure 34a, the lead pockets appear to be single phase, indicating a pure metal microstructure as expected. On the other hand, the segregated pockets in the bismuth bronze (Figure 34b) appear to have a two-phase microstructure. This material appears to have lamellar plates growing in from the particle interface, which is reminiscent of a coupled eutectic structure.

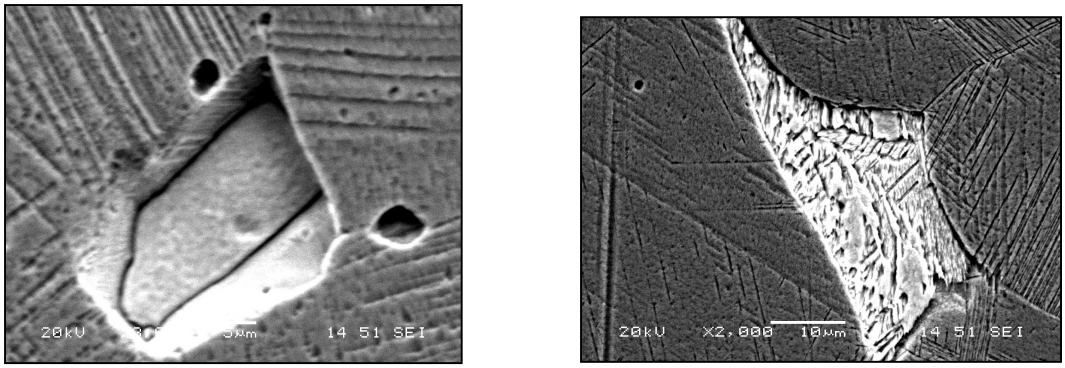


(a) (b)

**Figure 34. Pockets of a) lead and b) bismuth pockets after FeCl etch.**

## 3.4 Discussion

Initial microstructural comparison of the bronze portion of the Cu-10Sn-10Pb and Cu-10Sn-3Bi powder metal valve plates did not reveal substantial differences that would result in the increased damage observed in the bismuth bronze alloy. Similar prior particle size, hardness, and volume fraction of the "soft" phase pockets were observed in the alloys. The differences in the two alloys, then, lie directly with the composition and wear behavior of the soft phases.

Both lead and bismuth were chosen for their insolubility in copper, a practice that carries over from traditional production of these alloys by casting. However, the evidence for surface melting that was noted previously for bismuth bronze indicates an unforeseen problem with the substitution of bismuth for lead. Bismuth is known to be a cause of liquid and solid metal embrittlement of copper along the grain boundaries (Keast, 1999). During normal pump operation, ambient temperatures are high enough (about 130°C) to increase the ductility of the bismuth, but not high enough to induce melting of the bismuth pockets (pure bismuth melts at 271.40°C). However, the use of bismuth in bronze could introduce this problem due to the presence of tin that forms a simple binary eutectic with bismuth. Even at low concentrations of tin (3 wt. %), the 138°C solidus temperature of Bi-Sn could create a mushy, semi-liquid during normal pump operation. This particularly would be a problem along the interface between the bismuth pockets and the bronze particles.

Creation of a semi-liquid phase along the particle boundaries could result in the plateaus of material that were noted on bismuth bronze valve plates in Figure 24. As the soft phase material liquefies and is drawn out onto the surface, it is removing connecting structure thus weakening the sintered surface. The liquid containing bismuth could also promote liquid metal embrittlement (LME) along the grain boundaries. The combination of bismuth's intrinsic brittleness, the removal of molten material, and the embrittlement of copper (both solid state and LME) are likely responsible for the brittle appearance of the damage on the wear surface.

# CHAPTER 4. PHASE II: DEVELOPMENT OF THE ALLOY

## 4.1 Introduction

### 4.1.1 Premise of Work

In the previous chapter, it was shown that the Cu-10Sn-3Bi material designed to replace the Cu-10Sn-10Pb bronze as valve plate surface layer was not acceptable. As a replacement for the currently employed Cu-10Sn-10Pb alloy, the Federal Mogul designed Cu-10Sn-3Bi bronze was meant to utilize the insolubility of bismuth to create a soft second phase similar to the leaded bronze alloys (Saxton, 2006). The failure of the Cu-10Sn-3Bi material in axial piston hydraulic pumps illustrates that the limiting wear characteristics in this case were determined by the apparent melting of the soft phase. Selection of a new, lead-free approach was therefore critical for demanding operating conditions like the high loads and high speeds of the sauer danfoss axial piston hydraulic pump. While the attempt to use bismuth to reproduce a composite type of solidification microstructure using another insoluble phase was commendable, it was not required since other technologies are available in powder metallurgy and solidification processing. In fact, a novel combination of low density pressing and partial sintering, along with lead-free solder infiltration provided a basis from which to develop lead-free, bronze-based metal/metal composite bearings.

### 4.1.2 Lead-free Material Design

Perhaps inevitably, the solution for removing lead from this copper based application is similar to lead-free solder. In fact, both lead-free solders and soft bearing alloys share a common base metal, tin. Tin-based Babbit alloys have been used for decades nearly interchangeably with lead-based bearing materials. Although their cost is somewhat higher, tin-based babbits are generally considered superior to the lead-based alternatives.

The required microstructure would be virtually impossible to produce using admixed copper-tin bronze and tin alloy powder by liquid phase sintering. The relatively high temperatures and extended times required to sinter bronze powder would result in dissolution of the tin into the Cu-10Sn matrix. In fact this is a widely employed method of producing fully

dense bronze compacts. However, powder metallurgy offers alternate solutions to this problem. Infiltration is routinely utilized to fill interconnected porosity or surface porosity in powder metallurgical components. This is done for a number of reasons, not the least of which is wear properties. There are many examples of this, in various industries. For instance, refractory metals (W and Mo) are infiltrated with highly conductive metals (Ag, Cu) for heavy-duty electrical contacts; iron and steel are infiltrated with copper for strength and machinability; and, iron and copper are infiltrated with lead as low friction bearing materials (Thümmler et. al., 1993). Infiltration is considered either a special kind of liquid phase sintering or a finishing operation. In any event, the process requires first sintering a compact of the metal alloy with the higher melting point. The pores must necessarily be interconnected to allow full penetration of the lower melting metal by capillary forces. Infiltration of the second metal can be done at the end of the primary sintering treatment or in a separate process wherein the compact is reheated to the melting temperature of the infiltrant alloy. This alloy can be placed in contact with the sintered compact in various forms including powder, a slug, or already molten liquid.

### 4.1.3 Intermetallic Control

The selection of a tin alloy as a soft phase that can be infiltrated into bronze presents the opportunity for copper-tin intermetallics such as $Cu_3Sn$ and $Cu_6Sn_5$ to form where the tin solidifies in contact with bronze. In small concentrations, intermetallics have been shown to increase the adhesion of lubricating films and fatigue strength in babbit alloys; and to increase wettability and bonding between tin based alloys and copper substrates in solder applications (Deng et. al., 2005). The hardness of the copper-tin intermetallics is similar to that of pearlitic steel. This is a notable feature for use in axial piston hydraulic pumps. The P/M steel in the cylinder block is a eutectic steel containing this microstructure. Having a similar hardness reduces the wear rate of both sliding surfaces in many tribological systems. In this case, the similar hardness means the intermetallics should not cause significant wear of the cylinder block surface.

**Table 2. Mechanical properties of copper-tin intermetallics.**

| Property | $Cu_6Sn_5$ | $Cu_3Sn$ | Pearlitic Steel |
|---|---|---|---|
| Hardness (HV) | 378[1] | 343[1] | 270-350[2] |
| Toughness ($MPa \cdot m^{1/2}$) | 1.4[1] | 1.7[1] | 40[3] |

[1]Humpston et. al., 2004 [2]Herian et. al., 2008 [3]Aglan, Heshmat, 2006

Offsetting the advantages of the copper-tin intermetallics is their fracture toughness. In bulk form, $Cu_3Sn$ and $Cu_6Sn_5$ are rather brittle and are often considered to be detrimental to the strength of soldered joints. It must be noted that few reports definitively identify the intermetallic layers as the source of the failure (Humpston et. al., 2004). However, a continuous grain boundary network of a hard, brittle intermetallic phase could prove to be a detriment to both strength and wear properties. The reduced mechanical toughness of solder joints increases with thicker intermetallic phases (Deng et. al., 2005). To avoid breakup of the hard phase and resulting poor wear performance of the valve plate, the amount of intermetallics, particularly $Cu_3Sn$, at the interface need to be controlled. Initial reduction of the intermetallics can be achieved by limiting time at temperature during reflow. If the time is kept short enough, only the $Cu_6Sn_5$ layer forms. This layer slows the diffusion of tin into the bronze, slowing the growth of $Cu_3Sn$. Growth of the intermetallic layers can occur quickly, as shown in Figure 35. Thus a relatively precise processing technique had to be developed and some lead-free solder alloy developments had to be borrowed in order to infiltrate tin into the bronze compact with sufficient control of the intermetallic layers.

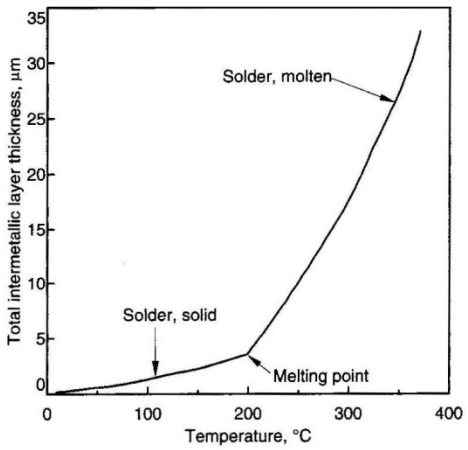


**Figure 35. Growth of copper-tin intermetallics after 100s at various temperatures.**

Another concern with copper-tin intermetallic is their growth at elevated temperatures. Hydraulic pumps can operate at temperatures of up to 130˚C, a temperature sufficient to cause the growth of the intermetallic phases during use. The rate of formation of $Cu_3Sn$ and $Cu_6Sn_5$ is determined by the rate of diffusion of the constituent elements (tin and copper) through the intermetallics (Humpston, 2004). The growth of these phases is well documented and summarized in Figure 36 below.

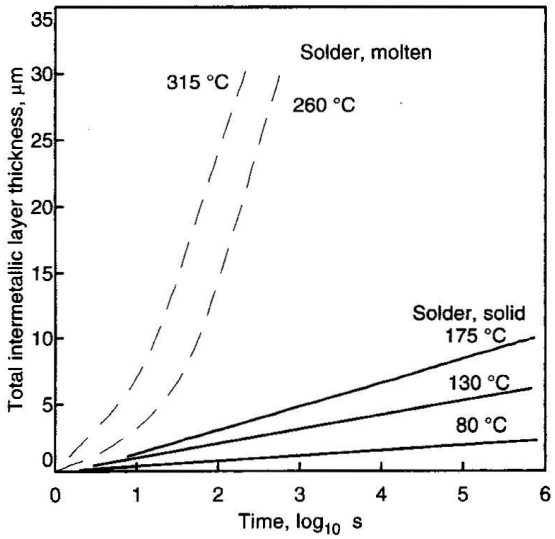


**Figure 36. Growth of copper-tin intermetallics in eutectic tin-lead solder on copper.**

Alloying additions can also be made that can suppress $Cu_3Sn$ formation, many of which are the subject of intense scrutiny in the lead-free solder arena. One of the elements under consideration for this purpose is manganese. Manganese has the additional benefit in this situation of forming a relatively high melting (230.97°C) eutectic with tin when alloyed at 1 to 9 weight percent. The melting point of this alloy is substantially higher than the tin-bismuth eutectic (138˚C) that was present in the Cu-10Sn-3Bi alloy. The addition of manganese creates a very dilute solid solution of tin and manganese with a slightly higher hardness than pure tin. More significantly, enough manganese will produce hard, needle-like $MnSn_2$ intermetallics that would be distributed in the soft tin manganese. This intermetallic phase would provide some benefit as they do in babbit materials for strengthening the soft phase.

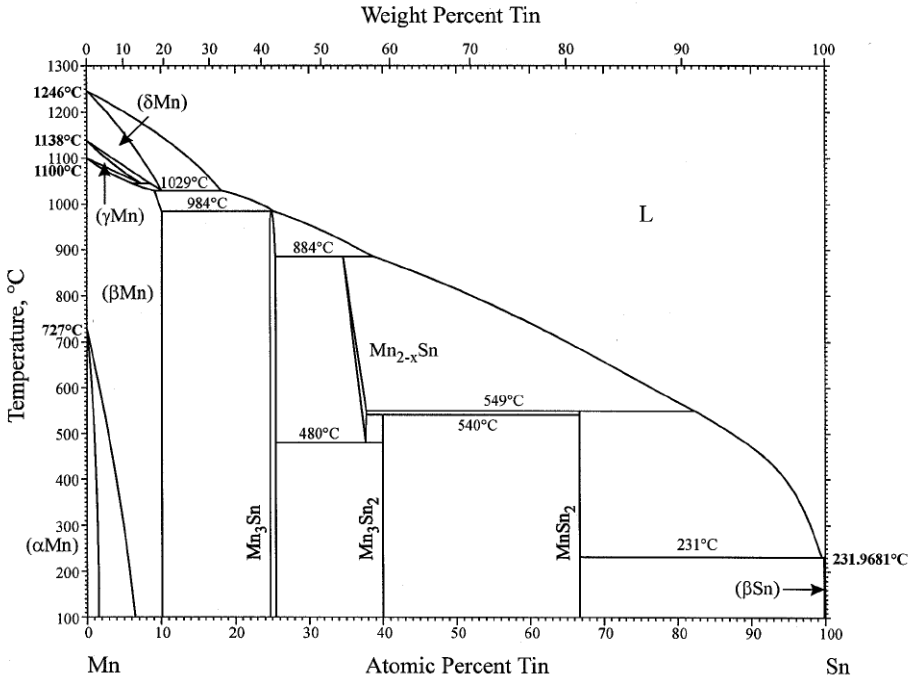


**Figure 37. Tin Manganese phase diagram (Okamoto, 1999).**

The optimum microstructure of the soft phase pockets depends on the proper processing techniques and alloying additions. The intent was to create a microstructure as illustrated in Figure 38. These soft phase pockets were to have a distribution at grain boundaries and triple junctions in the bronze matrix similar to the leaded bronze and the bismuth bronze alloy.

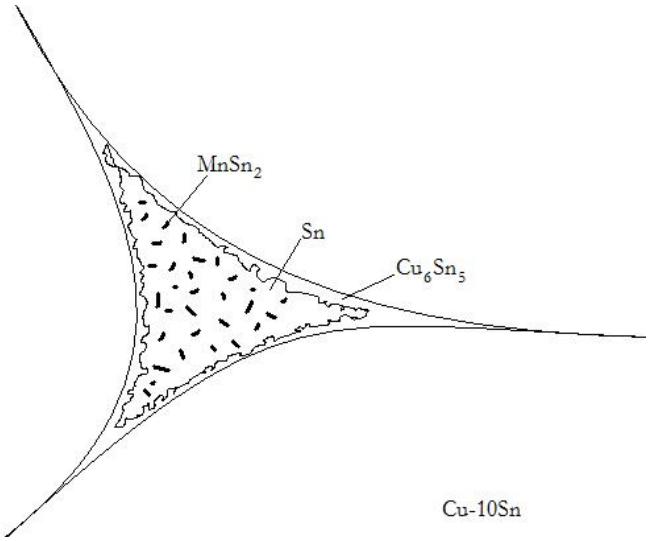


**Figure 38. Optimum soft phase microstructure.**

## 4.2 Materials

### 4.2.1 Tin-Manganese Infiltrant

For the current study, a powder form of the tin-manganese alloy was chosen to provide even coverage a partially sintered copper-tin bronze compact surface. The target tin alloy (1-9 wt.% Mn) was inert gas atomized in an argon atmosphere. The target size was less than 20μm, such that a carrier could be used to deposit the powder evenly on the surface of the bronze compacts. Atomization by HJE Company, Inc. (New York, USA) produced a tin manganese powder with a composition of 1.37% Mn (verified by Inductively Coupled Plasma (ICP) Atomic Emission Spectrometry). The Sn-1.37Mn powder (Figure 40) was sieved using -325 mesh to obtain a distribution with a d10 of 3.23μm, d50 of 7.81μm, and d90 of 15.48μm.

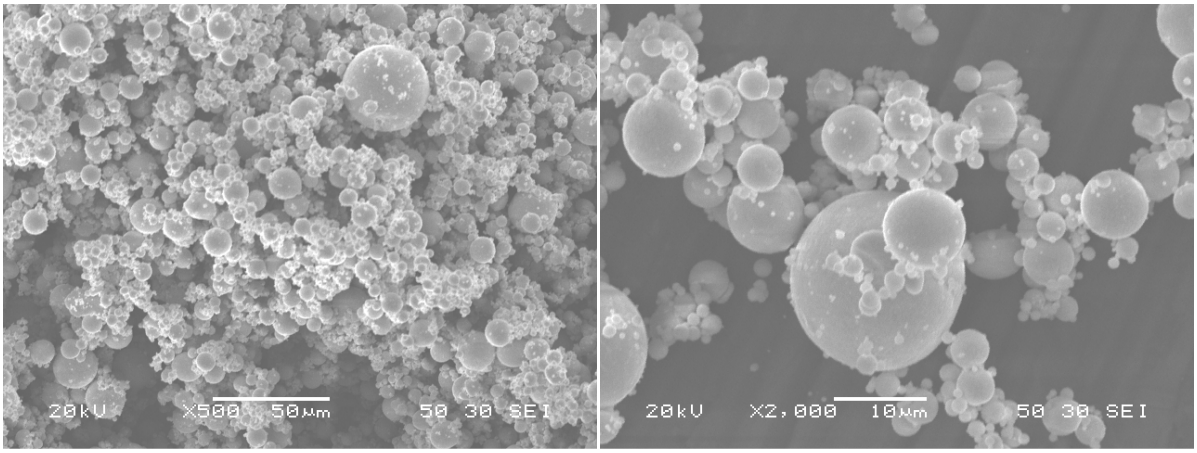


**Figure 39. Gas atomized Sn-1.37Mn powder.**

### 4.2.2 Tin Infiltrant

In addition to the tin-manganese powder, a gas-atomized (<25μm) pure tin powder (Figure 40) was also used to evaluate the effect of the addition of manganese to the infiltrant alloy. The tin powder size distribution appeared to contain less ultrafine powder than the tin-manganese powder, but the powder size distribution was not measured.

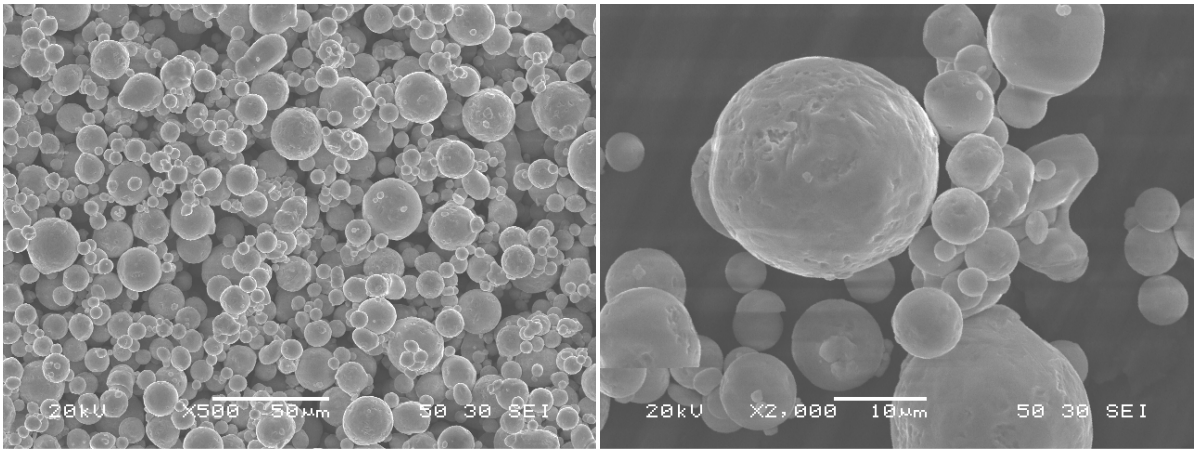


**Figure 40. Gas atomized Sn powder.**

### 4.2.3 Bronze Powder

The sintered bronze compacts used to develop the lead-free material were made from commercially available 90Cu-10Sn bronze powder. The bronze was ordered through Reade Advanced Materials (Nevada, USA) and produced by ACuPowder International, LLC (New Jersey, USA). ACuPowder listed the final product composition, determined by inductively coupled plasma spectroscopy (ICP) as 10.3 wt% Sn, 0.1 wt.% P, and the balance copper. Powder size distribution was 0.1% +200 mesh (>74µm), 94.8% -200/+325 mesh (44-74µm), and 5.1% -325 mesh (<44µm) as analyzed by ACuPowder (according to MPIF STD 05). It should be noted that the powder size distribution that was ordered was specified to correspond to the approximate grain size that was measured of the leaded bronze in Chapter 3.

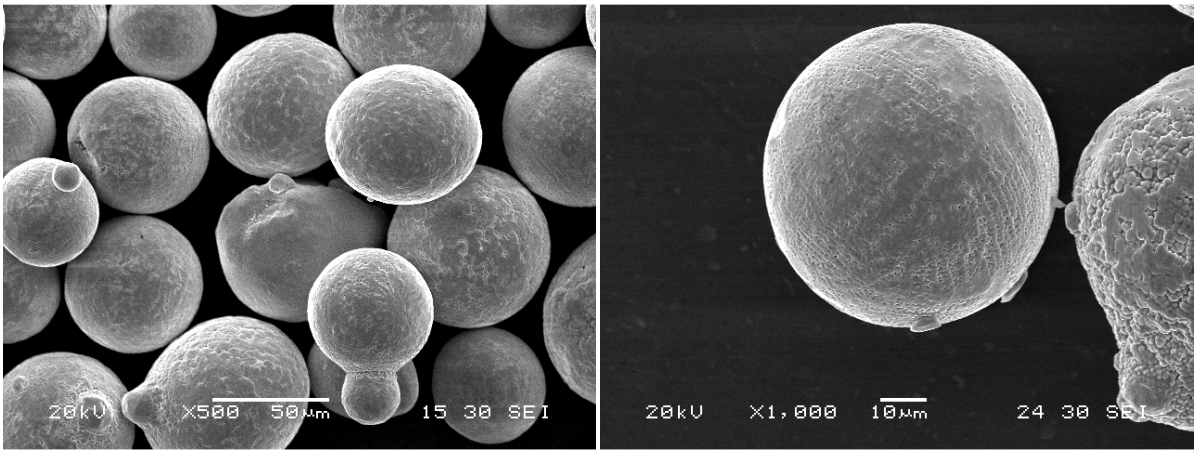


**Figure 41. Gas atomized 90-10Sn bronze powder.**

## 4.3 Sample Preparation Methods

### 4.3.1 Compaction

To create the bronze compacts for infiltration studies, 2.750±0.001g of the powder was weighed out. The powder was pressed in a 12.7mm diameter cylindrical single acting die comprised of a carbide sleeve press fit in tool steel. Compaction pressures from 100-700MPa were attempted to create compacts approximately 3.2mm thick with varying green densities. It was found that pressures less than 350MPa did not provide sufficient green strength for handling of the compacts. Samples compressed between 350MPa and 700 MPa (the upper limit of the die) were successfully created. Pressures within this range were used to press bronze compacts to develop the infiltrated bearing material.

### 4.3.2 Sintering

Green compacts to determine the effectiveness of infiltration were placed on alumina trays and sintered in a Lindberg/Blue STF54233C (240V, 30A, 60Hz) silica tube furnace. A vacuum was drawn on the furnace using a mechanical pump then a diffusion pump to a pressure of $5x10^{-5}$ Torr. The samples were heated at 20°C/min to the desired temperature, held at the desired temperature for two hours, then allowed to cool at a maximum of 30°C/min. The temperature program was managed by a Eurotherm 91P controller. By the end of sintering, the furnace vacuum typically reached low $10^{-7}$ Torr pressures.

Samples pressed at 550MPa were vacuum sintered at $10^{-6}$ Torr for two hours at 400°C, 500°C, 600°C, and 780°C (the latter chosen based on Nenakhov's 2003 work). It was found that temperatures below 600°C were not sufficient to create enough necking to provide adequate strength of the final bronze compact. At 600°C, necking increased to 30% of the particle diameter, ensuring adequate strength of the sintered bearing.

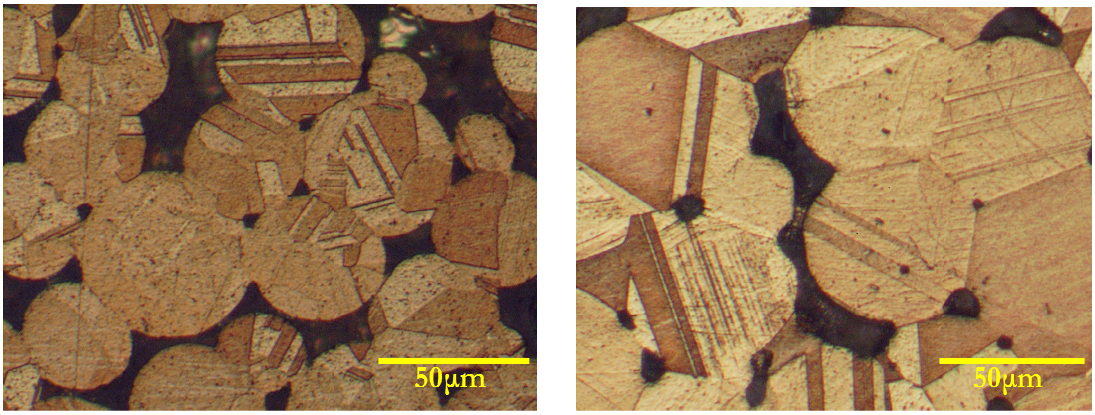


(a) (b)

**Figure 42. Necking in bronze pressed at 550MPa and sintered at a)600°C and b) 780°C**

## 4.4 Initial Infiltration

### 4.4.1 Methods

Samples pressed at 550MPa and sintered at 780˚C were chosen for initial experiments to determine whether the infiltrated material could be produced with a strength approaching that of conventional cast bronze. For initial study, the 12.7mm diameter presintered (550MPa/780˚C/ 2hr) bronze compacts were coating with a slurry of tin-manganese powder in methanol. The mixture was poured onto the sample surface until it was completely coated. The slurry was allowed to dry, resulting in a coating of powder approximately 1.5mm thick. The coated compacts were placed under a vacuum of $10^{-5}$ Torr for 12 hours, after which they were sealed in 15mm quartz tubes under 1/3 atm gettered UHP Argon. For the heat treatment, the quartz tubes were placed individually into a furnace preheated to 450˚C and held there until coalescence of the tin alloy was observed on the surface. When this condition was reached, the samples were removed from the furnace and the quartz tubes broken to allow a water quench of the sample.

Differential scanning calorimetry was also used to verify the melting point and solidification temperature of the Sn-1.37Mn alloy and pure tin. For the DSC runs, 14mg of powder was placed in pure copper DSC pans. The samples were held at 50˚C for 30 seconds, heated from 50˚C at 20˚C/min to 450˚C and held 30 seconds, then cooled at 60˚C/min to 50˚C to 50˚C.

### 4.4.2 Results

After being heated in quartz tubes under 1/3 atm of pure argon, initial samples displayed only partial coalescence (Figure 43) of tin-manganese powder on the surface even after reaching 425˚C. This is well above the 230.97˚C temperature the where the alloy would be expected to begin to melt.

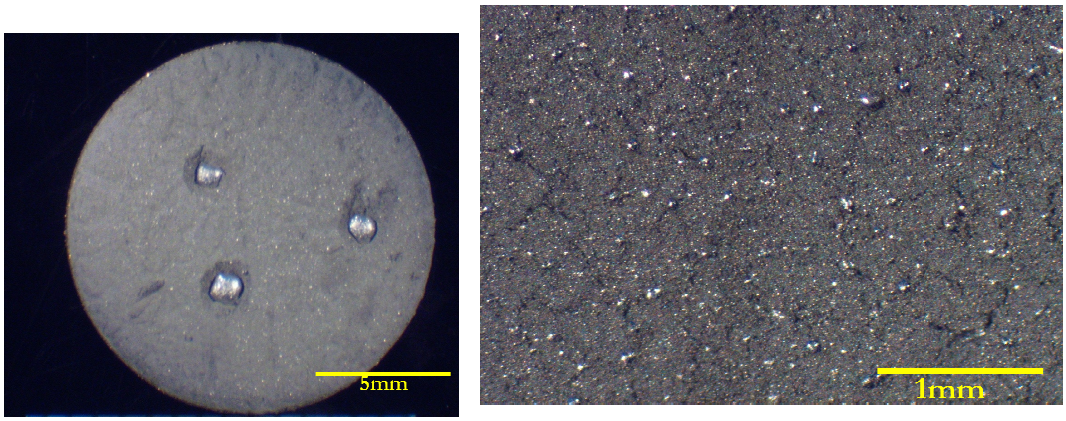


**Figure 43. Partial coalescence of Sn-1.37Mn on bronze compacts.**

A cross section of the compact (Figure 45) shows that the Sn-1.37Mn powder particles had only partially coalesced and a small amount of liquid made it to the surface for infiltration. A small pocket can be observed subsurface; however using the EDS capability of the SEM, it was determined that the pocket consists of $Cu_6Sn_5$ intermetallic (black arrow in Figure 44) separated from the bronze by a layer of $Cu_3Sn$ (white arrow in Figure 44). This morphology is not desired for a bearing alloy requiring a soft second phase. The excessive growth of the intermetallic phases were the result of the high temperature attained during the attempted infiltration.

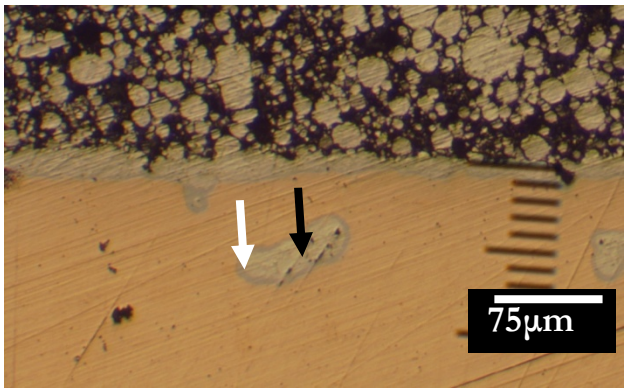


**Figure 44. A polished cross section of the sample shown in Figure 40.**

The small amount of liquid making it to the surface was a result of the partial coalescence of the tin powder. Effective infiltration requires full contact with, and wetting of, the presintered compact by the infiltrant alloy. Issues during the production of the Sn-1.37Mn alloy had previously suggested that atmospheric contamination, specifically with nitrogen and hydrogen, played a significant role in the ability of the material to melt. Here, this type of reaction may have created a shell on the molten tin-manganese powder particles, preventing them from coalescing. To test this theory in the context of infusion, the infiltration experiment was repeated with sub-25μm pure tin powder. As Figure 45 shows, there is a significant difference between the melting and coalescing capabilities of Sn-1.37Mn and pure Sn powders in a partial vacuum.

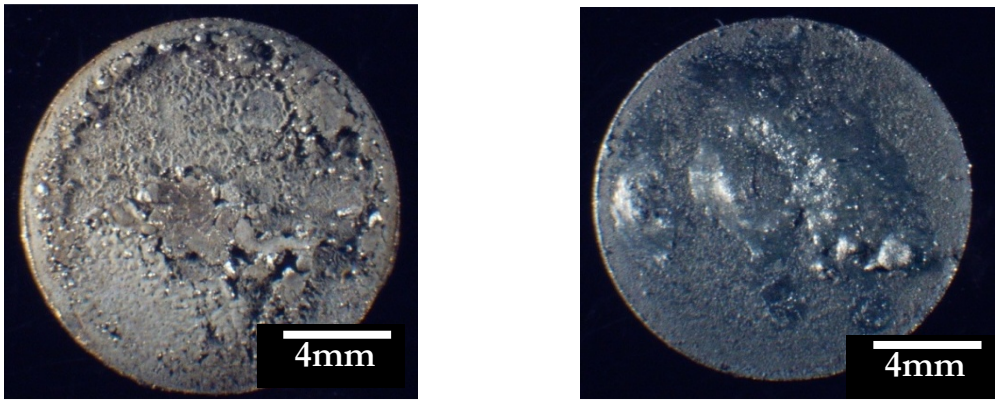


(a) (b)

**Figure 45. a) Sn-1.37Mn and b) Sn powders after equivalent heat treatment.**

Differential scanning calorimetry was used to determine whether the Sn-1.37Mn alloy was simply not reaching a liquid state during the procedure or whether the problem was with a lack of coalescence. The results (Figure 46) showed that the onset of melting for Sn-1.37Mn (230.97˚C) was only 0.2 degrees higher than that of pure Sn (230.6˚C). These temperatures compare reasonably well with that predicted by their respective phase diagrams - 230.85 ˚C for Sn-1.37Mn and 231.95˚C for pure Sn. Observation of the powders after DSC runs showed a similar result to that shown in Figures 46. The Sn-1.37Mn alloy coalesced significantly less than the pure Sn, suggesting that a reactive shell on the Sn-1.37Mn powder prevented coalescence required for proper infiltration of the bronze compact.

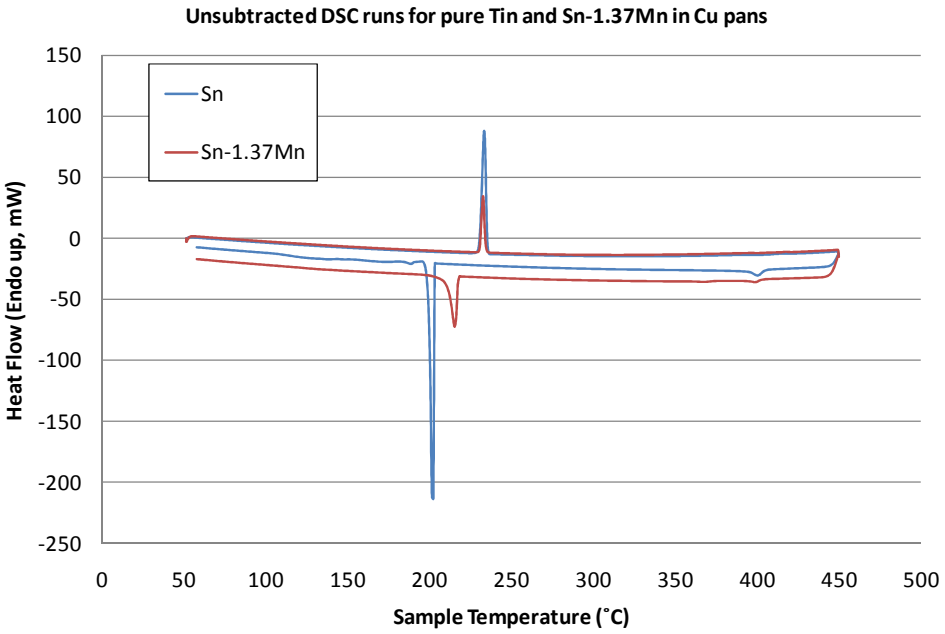


**Figure 46. Differential scanning calorimetry of Sn-1.37Mn and pure Sn.**

Although issues arose with coalescence of the powders and possible atmospheric sensitivity of Sn-1.37Mn, infiltration of the porous bronze with Sn-1.37Mn is possible given proper control of atmospheric conditions within the quartz tubes (i.e. ensuring a full vacuum was drawn and the quartz tube completely sealed). In the sample shown below in Figure 47, a presintered (780˚C, 2 hr.) bronze compact was successfully infiltrated to adequate depth (250-500μm) required for steel-backed sintered bronze bearing materials.

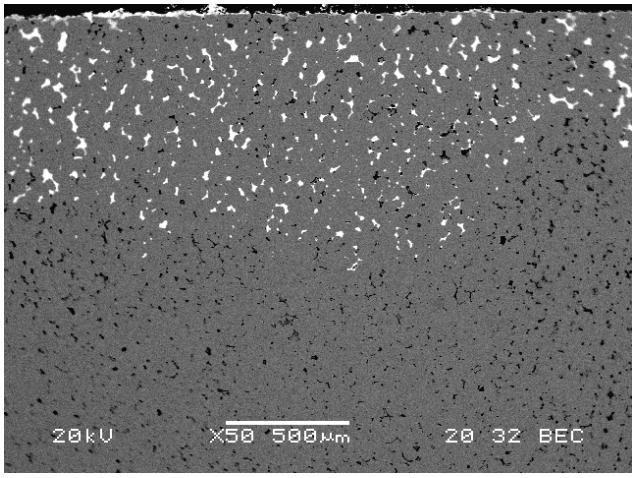


**Figure 47. Backscattered image of Sn-1.37Mn (shown as white) penetration depth.**

Although promising, the overview image in Figure 48 shows that the distribution of the tin is not even in the presintered (550MPa/780˚C/2 hr.) compact. There are pores visible that were not filled with Sn-1.37Mn upon infiltration, indicating a lack of interconnected porosity. In addition, the depth of penetration is not consistent across the entire surface of the 12.7mm presintered compact.

The filled pores of the sample shown in Figure 48 are shown in a larger view in Figure 49 below. The microstructure closely mimics that foreshadowed in Figure 38. The microstructure consists of a pocket of pure tin rimmed with $Cu_6Sn_5$ intermetallic. Energy dispersive x-ray spectroscopy (EDS) was used to confirm the identity of the phase at the pore boundary.

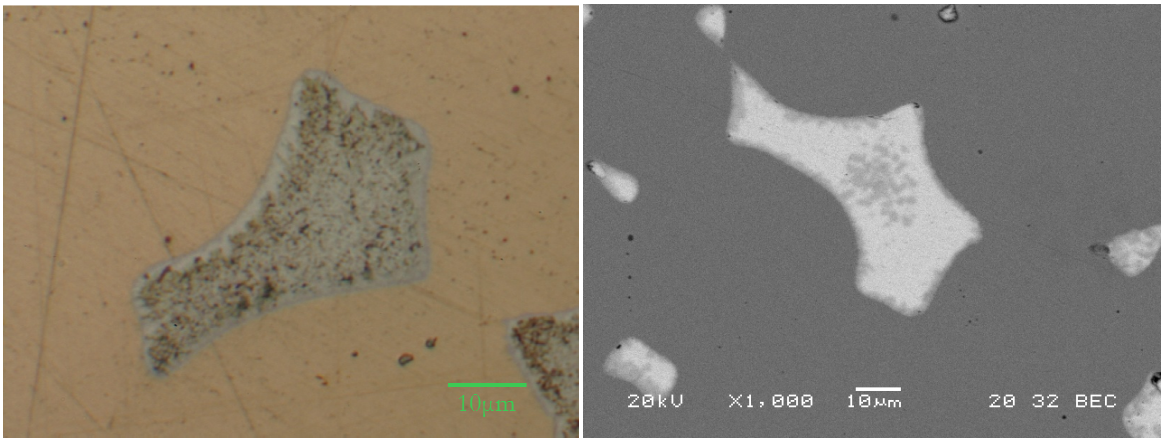


(a) (b)

**Figure 48. a) Optical and b) backscattered images of the infiltrated tin.**

Backscattered electron imaging in the scanning electron microscope shows $Cu_6Sn_5$ in the center of the pore. This appearance of this intermetallic is actually the result of a polishing into $Cu_6Sn_5$ "scallops" that grew normal to the image plane. A similar pocket is shown in Figure 49 without the soft tin phase present. The $Cu_6Sn_5$ scallops are visible around the rim of the pocket, and in several places, those that have grown on the "bottom" face have been polished into. An example of the lopped $Cu_6Sn_5$ scallops is highlighted in the inset image that represents a 300% enlargement of the junction of the three arms of the pocket.

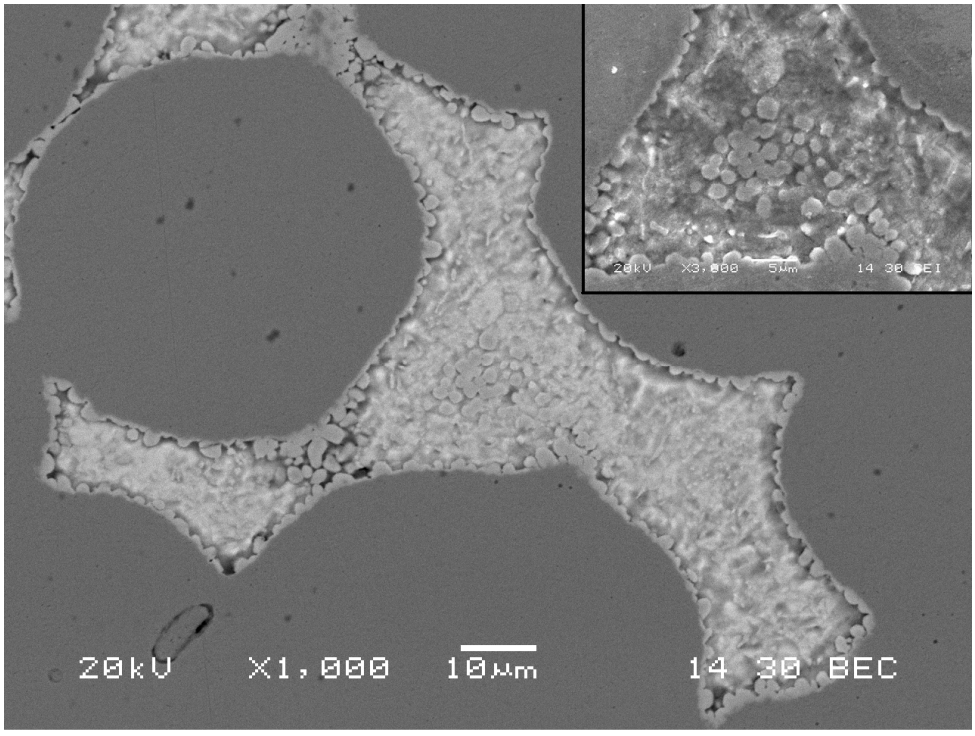


**Figure 49. Distribution of $Cu_6Sn_5$ intermetallics in a tin infiltrated bronze pore.**

### 4.4.3 Discussion

There are some obvious difficulties arising as a result of the method of production. Using the infiltrant in the form of powder creates problems with coalescence upon melting. In addition, the manganese containing powder shows signs of reaction with either the atmosphere or the ethanol powder carrier. Even so, infiltration of the bronze compacts was shown to be possible. However, the lack of fully interconnected porosity meant that not all the pores were filled. While the remaining porosity is not necessarily detrimental to the performance of the alloy in lubricated environments, an even distribution of solid lubricant in the bronze to a depth of approximately 500µm is desired for a steel-backed bronze bearing. Therefore, further refinement of the porosity in the bronze compacts was necessary.

## 4.5 Infiltration Refinement

### 4.5.1 Methods

#### 4.5.1.1 Compact Density

In order to study the infiltration of the bronze, it was decided to create porous compacts with the highest interconnected porosity possible at the expense of strength. This way, a best-case scenario was created for infiltration and the microstructure could be examined. To refine the interconnected porosity of the bronze compacts, the sintering study (4.3.2 ) was revisited. Based on the analysis, 12.7mm diameter, 3.2mm thick bronze compacts were pressed at the lowest compaction pressure (350MPa), then sintered at 650˚C for two hours.

Interconnected porosity is required to ensure full infiltration of the bronze compact. To alleviate this problem, subsequent samples were pressed at a lower compaction pressure (350MPa) and sintered at 650˚C for two hours. This heat treatment allowed for the maximum porosity (19 vol. % by optical microscopy) while still retaining significant strength. Closer examination of the microstructure in the bronze compacts previously used (550MPa/780˚C/2hr) shows that porosity was not fully connected in some regions of the compact. Porosity of these samples was determined to be approximately 10 volume percent.

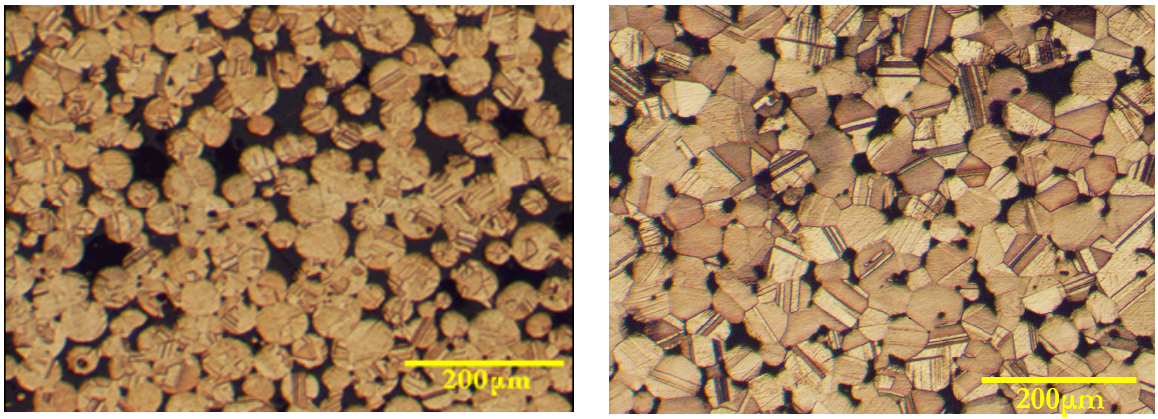


(a) (b)

**Figure 50. Porous bronze created by a) 350MPa/650°C/2hr and b)550MPa/780°C/2 hrs.**

#### 4.5.1.2 Flux

Improvements in available material and wetting were required to ensure full infiltration of the bronze compact. This meant the poor Sn-1.37Mn powder coalescence had to be addressed, so the decision was made to utilize a flux. Using a flux provides greater control over the final microstructure and prevention of intermetallic growth by decreasing the time for full coalescence of the bronze compact. Providing a clean bronze surface increases the wetting of the tin on the bronze, thus increasing the capillary force available to draw the alloy into the interconnected porosity.

Two thermally activated, zinc ammonium chloride based fluxes were acquired from Johnson Manufacturing Company (Iowa, USA). The fluxes, known by their proprietary names E127 and E130, were both initially used. However, E127 was a more aggressive flux used for industrial tinning of bearing shells prior to babbitting. Its effective nature was evident in early tests so it was selected for use in the remainder of the study. Using the E127 flux, pastes were created by mixing in the pure tin or Sn-1.37Mn powders. The pastes were formulated to contain 70-75 wt. % metal content, the weight ratio suggested by the manufacturer.

#### 4.5.1.3 Infiltration

After the pastes were mixed, drops of the pastes were placed on presintered (350MPa/ 650˚C/2 hr) compacts of the 90Cu-10Sn bronze. These samples were placed in a glovebag setup shown schematically in Figure 51. The bag was sealed and purged with ultra high purity argon until the oxygen levels were below 300ppm as measured with an Illinois Instruments Model 810 zirconia oxide oxygen sensor. A Thermolyne Type 2300 hotplate was then preheated to 250°C and allowed to stabilize. The temperature was monitored with a type K thermocouple placed in contact with the hot plate's aluminum heating surface. Once the proper temperature was reached, samples were placed on the hot plate until the flux activated and the tin alloy melted. Upon coalescence of the tin, the samples were removed from the hot plate and placed on a room temperature copper chill block for a mass quench. They were allowed to completely cool before being removed from the argon atmosphere.

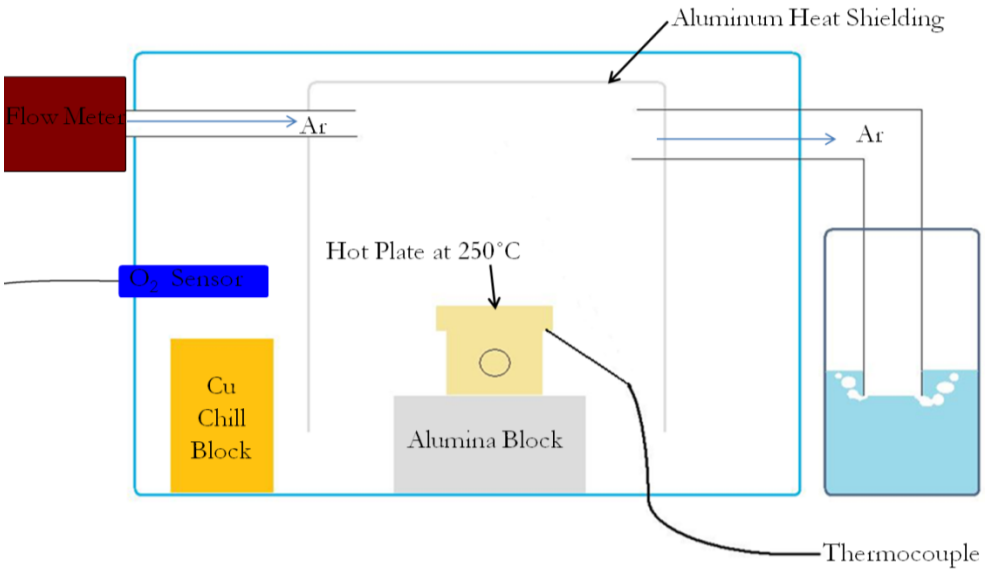


**Figure 51. Argon glovebox configuration.**

### 4.5.2 Results

After the sample was placed on the hot plate (Figure 52a), the paste bubbles as the solvent begins to boil off (52b), drying the paste as the temperature rose. At 110˚C, the flux is activated (52c) (verified by DSC). As the flux was activated, a white vapor was visible from the specimens (not shown). The vapor was more prominent in samples with pure tin in the paste. Within 45 seconds, the temperature rose to the melting point of the tin alloy, the metal coalesced (52d) and infiltrated the bronze (52e), and the sample was removed. The total time above the melting temperature for the 12.7mm disks was 5-10 seconds before they were cooled.


**Figure 52. a) Sn-1.37Mn and b) Sn powders after equivalent heat treatment.**

After infiltration, typical tin and tin-manganese infiltrated compacts had the appearance shown in Figure 53. The pure tin infiltrated samples were all nearly completely flush with the surface. Only the charred glycerin of the flux remains on the surface and that is water soluble. In the tin-manganese samples, a visible lump of metallic material remained on the surface along with the charred glycerin. This was fairly consistent across the manganese containing samples.

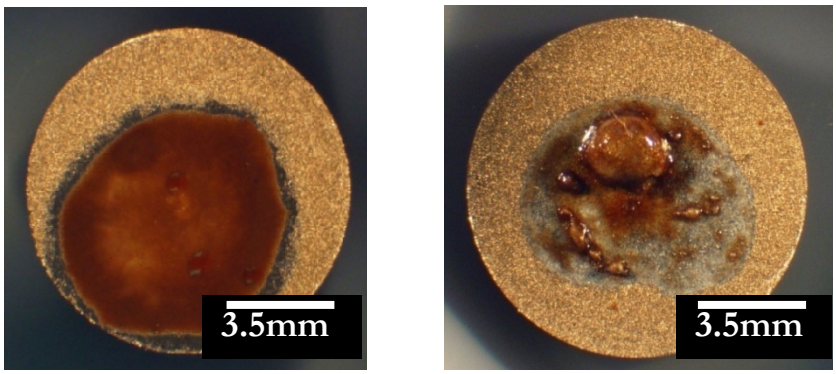


(a) (b)

**Figure 53. 350MPa/650°C/2hrs bronze compact infiltrated with a)Sn and b) Sn-1.37Mn.**

Cross sections of the bumps left on the tin-manganese samples (Figure 54a) showed that they contained gas pockets likely formed during the flux off-gassing. When removed from the surface and examined using SEM, they appeared as in Figure 54b. EDS shows the bumps contain elevated levels of manganese. This suggested that the manganese was reacting with the product of the flux's reaction with the bronze. Manganese is reactive with carbon, oxygen, nitrogen, and chlorine. Each of these may be present during infiltration. Oxygen and nitrogen can be present due to atmospheric contamination, and chlorine and carbon are both byproducts of the flux reaction.

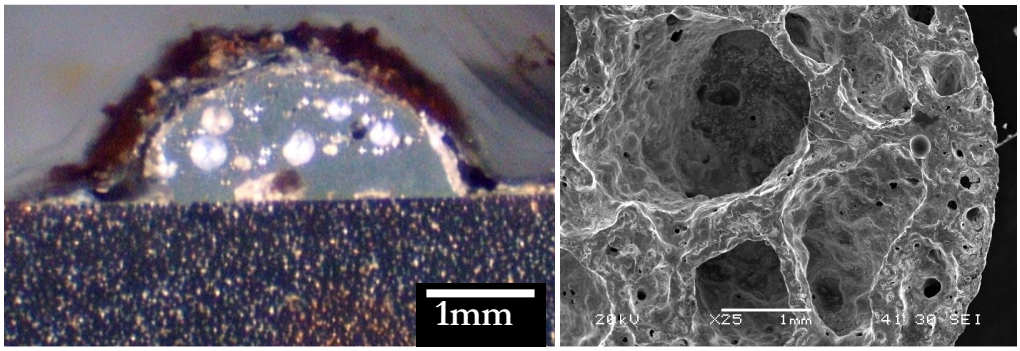


(a) (b)

**Figure 54. Residual Sn-1.37Mn a) cross section and b) from the underside of the bump.**

Although differences were noted in the surface appearance after infiltration of the Sn and Sn-1.37Mn samples, both infiltrated well into the sintered bronze compact as shown in Figure 55. Although a small amount of Sn-1.37Mn was placed on the sample, the metal infiltrated to a nearly uniform depth of 2mm under the area the contacted by the infiltrant.

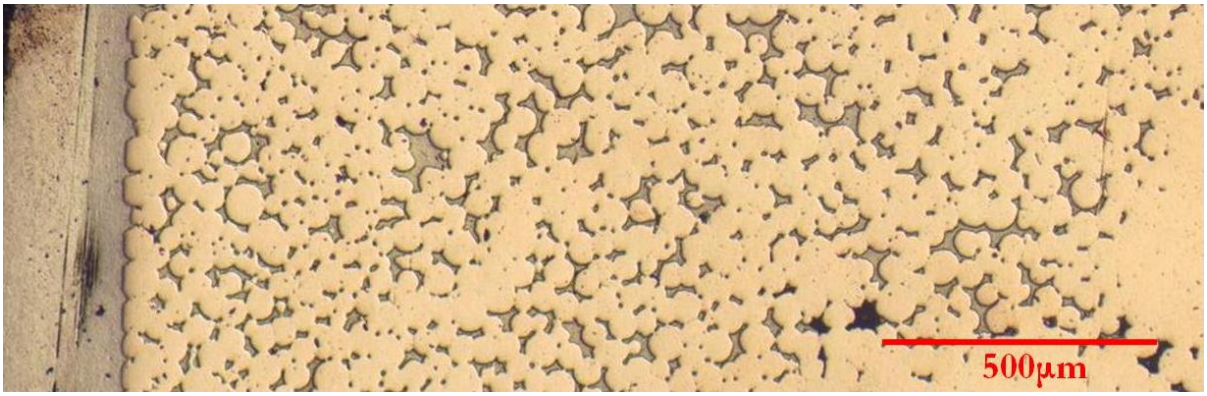


**Figure 55. Infiltration of Sn-1.37Mn alloy into a 90-10Sn compact using E127 flux.**

In addition to effective infiltration, the soft tin metal was evenly distributed in the compact and possessed the target morphology consisting primarily of the soft phase with minimal intermetallic rim as shown in the images in Figure 56.

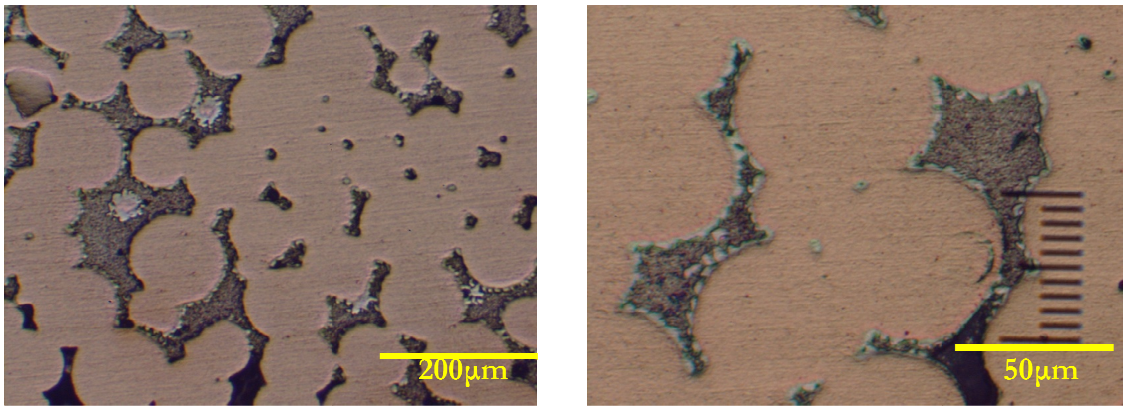


**Figure 56. Pockets of Sn-1.37Mn in Cu-10Sn bronze with $Cu_6Sn_5$ rims.**

When the morphology of the original Cu-10Sn-10Pb alloy, the Federal Mogul Cu-10Sn-3Bi, and the newly created Cu-10Sn/Sn-1.37Mn composite material are compared using secondary electron imaging in the scanning electron microscope (Figure 57), the similarities are clear. The size and distribution of the soft phase pockets in the new composite were very similar to that of the two previous alloys.

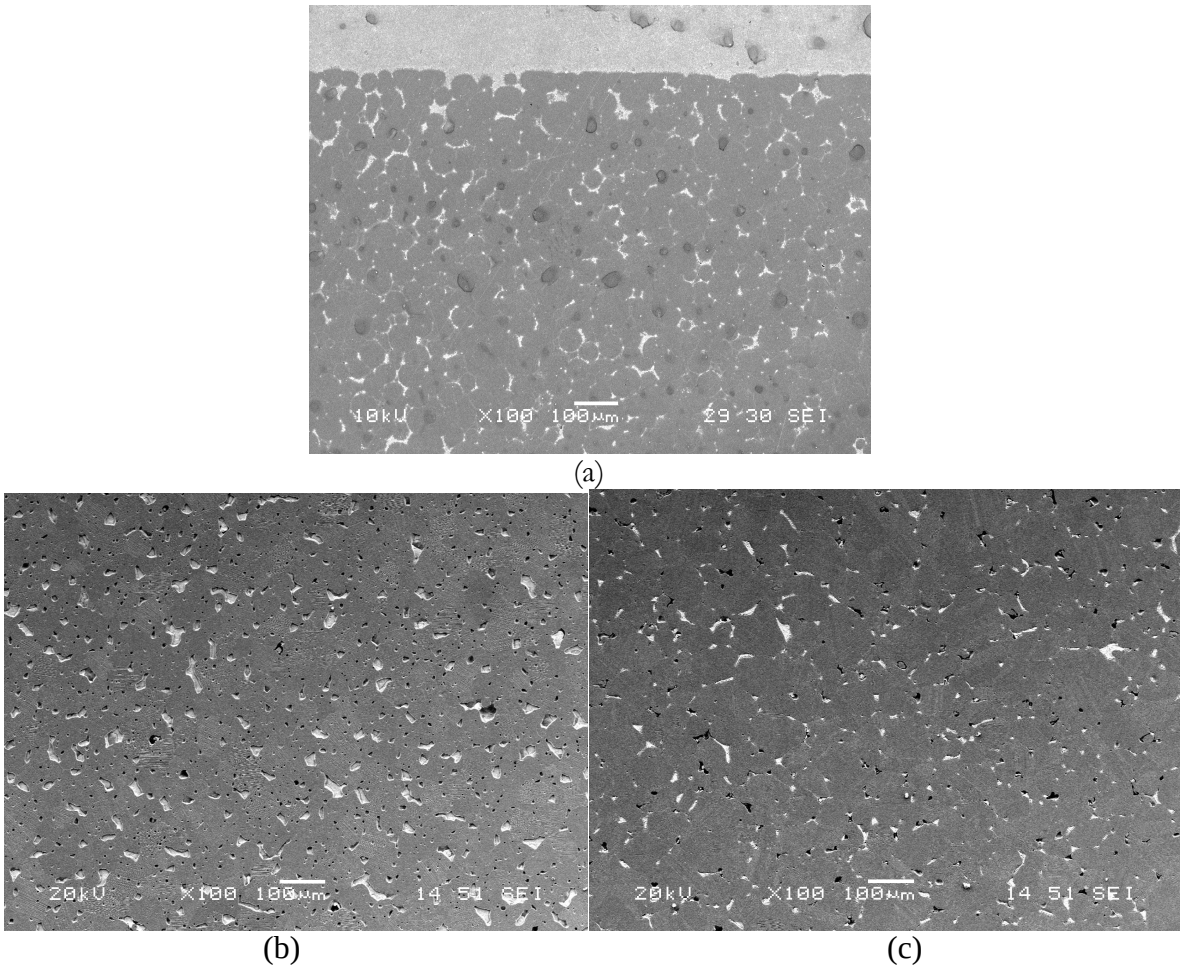


**Figure 57. Soft phases in a) Cu-10Sn-10Pb b) Cu-10Sn-3Bi and c) Sn-1.37Mn/Cu-10Sn.**

### 4.5.3 Discussion

The steps taken to address each of the three initial problems with the initial infiltration study worked as intended. By controlling the atmosphere, using a flux, and ensuring interconnected porosity, the ability to infiltrate the sample was greatly increased. In addition, each of these things led to lower time at temperature. In turn, this limited the formation of the copper-tin intermetallics around the pockets of tin.

# CHAPTER 5. PHASE III: MATERIAL VALIDATION

## 5.1 Introduction

The Cu-10Sn/Sn-1.37Mn and Cu-10Sn/Sn metal-metal composite materials show promise as a replacements for Cu-10Sn-10Pb leaded bronze in terms of microstructure. To evaluate their performance as bearing materials, characterization of the material in terms of mechanical, life, and wear properties was required. Ambient oil temperatures in the pump are high enough to promote the growth of intermetallics at the copper-tin interface. Therefore aging tests were critical to determine the lifetime of the soft phase and thus the effective lifetime of the bearing.

The action in the pump induces substantial stresses in the valve plate. It was important, then, to evaluate the strength of the new bearing material and gain an understanding of how that strength varied with porosity. The porosity and strength would eventually need to be balanced for the optimum bearing material design.

Finally, and most importantly, wear tests were required to evaluate the friction coefficient of the new material and its durability. The Cu-10Sn/Sn-1.37Mn and Cu-10Sn/Sn composites must provide adequate wear resistance while providing a low friction surface. Wear tests also bring to light unforeseen failure mechanisms such as those seen in the Cu-10Sn-3Bi material.

## 5.2 Methods and Procedures

### 5.2.1 Thermal Aging Testing

Axial piston hydraulic pumps are capable of running up to 10,000 hours. During this lifetime, the ambient oil temperatures are increased due to frictional and other fluid losses throughout the hydraulic system. It is not uncommon for the hydraulic fluid to reach temperatures of 130°C for extended periods of time. To understand the effect of this temperature on the new composite bearing materials, thermal aging tests were to performed on

the current alloy. Of primary concern was the growth of $Cu_6Sn_5$ and $Cu_3Sn$ intermetallics at the interface between the soft tin pockets and the porous bronze microstructure.

Sample preparation for the aging tests was identical to that used to create the specimens for initial metallography. Bronze powder was compacted at 350MPa to create a disk 12.7mm in diameter and 3.2mm thick. A small spot of premixed solder paste, consisting of sub 20μm tin or Sn-1.37Mn powder in Johnson number E127 flux, was placed on the surface. The sample was placed on a hot plate set at 250°C and allowed to reflow under argon before being mass quenched on a copper chill block.

These specimens were divided up into three groups: as-infiltrated, 100 hour, and 750 hour aging times. The first group was examined immediately after infiltration. For the aged specimens, a Thermolyne 21100 tube furnace (120V 11.3A, 60Hz) was set to 130°C and allowed to stabilize overnight. The temperature was profiled through the furnace to determine final sample placement. The second set of samples was then placed on a thin alumina tray and into the furnace for a period of 750 hours. A type K thermocouple was placed in direct contact with the alumina tray to ensure the temperature held at 130±1°C. After the specified time, the samples were removed and the second set placed in the furnace. The second batch was maintained at 130°C for 100 hours.

After aging, the samples were mounted in a conductive epoxy resin, cross sectioned, and examined using the backscattered electron imaging capability of the SEM. Relative measurements of the overall intermetallic layer as well as the individual $Cu_6Sn_5$ and $Cu_3Sn$ layers were made to gauge how the tin-alloy infiltrated bronzes age.

### 5.2.2 Strength Testing

For the initial development of the alloy, the lowest reasonably possible density was utilized to ensure open porosity and effective infiltration of the sintered compact. However, the application demands sufficient strength to prevent failure of the sintered surface. This is required to prevent the radial cracking that was present in the Cu-10Sn-3Bi valve plates. Eventually, it will be pertinent to optimize the compaction and sintering parameters to balance the level of porosity in the bronze while retaining the proper strength. Therefore it was useful to study the strength and porosity as a function of these parameters.

Strength tests were performed to measure transverse rupture strength (TRS) according to ASTM standard B528-05. A 2x2 full factorial experimental design was used with the two variables being compaction pressure (350MPa and 700MPa) and sintering temperature (650°C and 780°C). The samples are compacted in a Borg Warner single acting die. They are compacted to form rectangular prisms 3.18cm long, 1.27cm wide, and 6.35mm thick as per ASTM standard B925-03. The samples were place on alumina trays and sintered in a Lindberg/Blue STF54233C tube furnace (240V, 30A, 60Hz) silica tube furnace. A vacuum was drawn on the furnace using a mechanical and diffusion pump to at least $5x10^{-5}$ Torr before the temperature program, controlled by a Eurotherm 91P, was started. Typically the furnace reached $10^{-6}$ Torr before being ramped up at 20°C/min to the desired temperature. After sintering for the desired time, typically two hours, the samples were furnace cooled at a maximum of 30°C/min to room temperature. By the end of sintering, the furnace vacuum had reached low $10^{-7}$ Torr pressures.

In addition to the four sets of TRS bars, three other sets were created. The first set was designed to represent solid bronze and was prepared according to the ASTM standard. Each sample was pressed at 700MPa, then sintered at 780°C for four hours. The other two additional sets of samples were designed to determine the effect of tin infiltration on the strength of the sintered bronze compact. For this experiment, transverse rupture specimens were created according to the ASTM standard using the 350MPa compaction pressure and 650°C sintering temperature. After they were removed from the furnace, the samples were infiltrated with pure tin. A layer of paste (approximate one gram of <20μm Sn + Johnson E127 flux) was placed on the center third of the smoothest 3.18cm by 1.27cm side of the bar, as shown in Figure 58. Each sample was then placed on a hotplate set at 250°C under argon to reflow the tin and infiltrate the bar. The bars were then mass quenched using a copper chill block. Of the samples prepared in this manner, one set was aged 100 hours before testing, the other set was tested as-infiltrated.

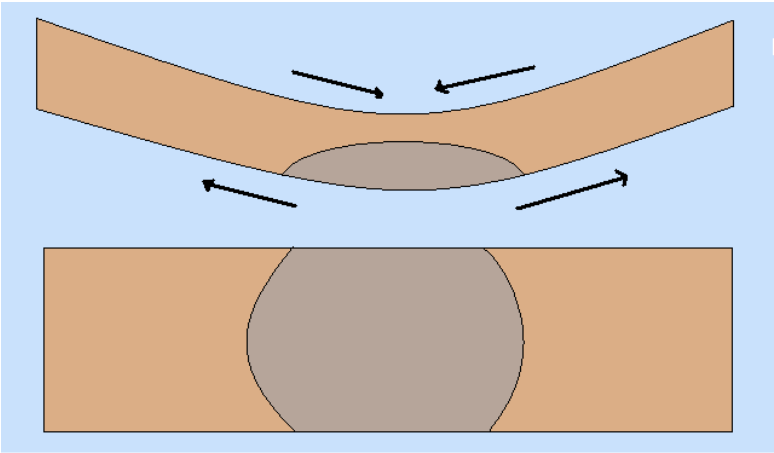

**Figure 58. Infiltration placement on TRS bars.**

An Instron model 55R1125 test frame was used to measure transverse rupture strength, using a fixture designed according to the ASTM specification. The Instron was set to deflect the sample at a rate of 0.05 in/min. The force required was recorded as a function of deflection distance and used to calculate the transverse rupture strength.

### 5.2.3 Lubricated Wear Testing

The most important qualification for a bearing material is of course its wear performance. In the current study, the objective was to replace the current Cu-10Sn-10Pb bronze used as valve plate surface layers in axial piston hydraulic pumps. The new material was to outperform the Cu-10Sn-3Bi material that was tried as a replacement. Comparisons between the materials are best made by standard test used for each material to eliminate external variables. In this case, larger specimens were created of the tin-infiltrated bronze material developed in Chapter 4. They were compared to the production leaded bronze valve plates and the experimental valve plates using pin-on-disk wear testing.

#### 5.2.3.1 Equipment

The basis for the test was the standard pin-on-disk test method as defined by ASTM G99-05. The wear tests were performed using the Falex ISC250PC tribometer described in Chapter 3. However, wear is very specific to the application (as exemplified by the anecdote of the Cu-10Sn-3Bi valve plates). The primary aim of the wear tests was to directly compare the

newly developed Cu-10Sn/Sn-1.37Mn and Cu-10Sn/Sn materials with the Cu-10Sn-10Pb and Cu-10Sn-3Bi materials. Therefore, it was more appropriate to mimic the conditions in the hydraulic pump than adhere to the ASTM standard.

The current ASTM standard and Falex tribometer limit the test parameters – load, sliding speed, distance, temperature, and atmosphere. The variables were limited to 500g, 300RPM and 80mm diameter, room temperature, and air, respectively. To replicate conditions in the hydraulic pump, the tribometer was modified (Figure 59) to provide increased loads, increased sample diameter, lubrication, and a new pin design.

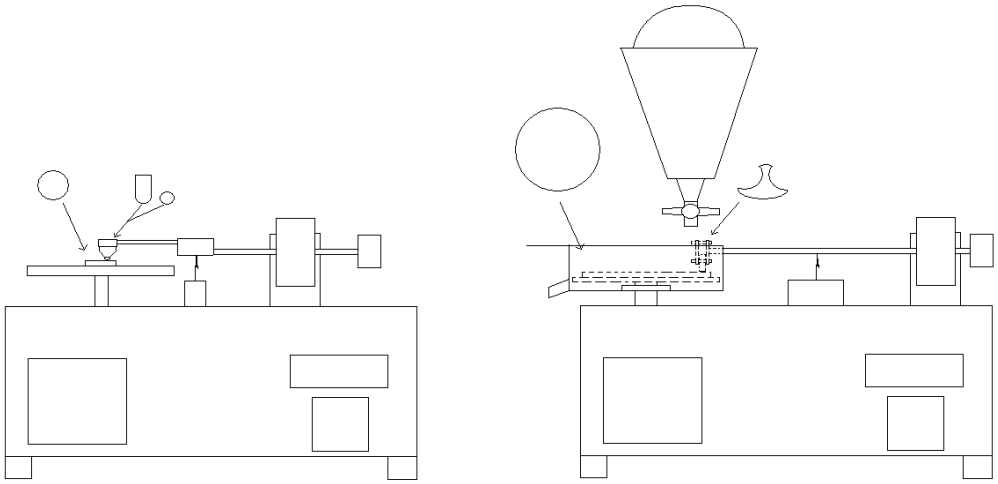

**Figure 59. Modified Falex tribometer schematic.**

Lubrication in axial piston hydraulic pumps is provided by the hydraulic fluid. For Sauer Danfoss, the standard test fluid is ISO-46 grade Shell Tellus Plus. For the purposes of this study, the hydraulic fluid for pin-on-disk testing was provided by Sauer Danfoss. The hydraulic fluid was held in two reservoirs adjacent to the Falex tribometer, as shown in Figure 60. The bulk of the fluid was contained in the lower reservoir, a 2000mL Erlenmeyer flask that rested on a hot plate to aid in maintaining fluid temperature. From this reservoir, the fluid was pumped to the upper reservoir using a Weaton Unispense Peristaltic Pump. The upper reservoir was a 1000mL separatory funnel where the oil was heated to its final temperature and permitted to flow onto the bearing disk surface at a controlled rate of about 500mL/min. Heating of the fluid was performed using a 190 W, 115 V Sigma Aldrich Heating Mantle to a temperature between 80-130°C. Temperatures in this range were selected because they represent normal operating

temperatures in hydraulic systems. Above 80-90°C, the polar molecules of the petroleum based oil lose their effectiveness and chemical additives designed to reduce wear become critical. To keep the temperature above the critical minimum temperature, an Omega CN7600 Temp Controller was used.

**Figure 60. Modified Falex tribometer.**

The oil flow was directed onto the disk surface immediately ahead of the pin to provide continuous lubrication, as shown in Figure 61. After hitting the sample, the hydraulic fluid was flung to the sides of an insulated oil catch pan, which is also visible in the image. It was then directed out a drain to the lower reservoir for reheating. Thus the hydraulic fluid was recirculated as it would be in a hydraulic system. The hydraulic fluid was replaced between tests of the various materials to ensure the results were not affected by the wear debris of previous materials.


**Figure 61. A lubricated wear test in progress.**

The arm of the tribometer was also modified to further enhance the capacities of the Falex tribometer. Normal loads in the axial piston hydraulic pumps used for this study range from 1.290 MPa to 2.54 MPa (Sauer, 2008). To achieve these loads on the surface of the disk, the arm had to be redesigned so that it was strong enough to handle the load. It also had to be modified so that the load was located greater than half the distance from the pivot point to the pin, creating a larger moment on the disk itself. This allowed more force to be applied with less weight hanging on the arm.

As a result of the arm lengthening, the pivot point had to be relocated. Since this relocation required a spacer block to be built, the capabilities of the pin-on-disk wear test machine would be further enhanced by allowing larger diameter specimens to be tested. By increasing the disk radius, higher sliding speeds could be achieved. The spacer block and arm were modified to allow testing of sample disks with radii up to approximately 80mm.

In addition to handling higher weight and larger disks, the arm was modified to hold a new pin design. It was determined that the traditional spherical pin design would not adequately represent the contact between the cylinder block and valve plate. To create the effect of boundary lubrication and simulate an area of contact rather than a point, a new pin was designed. This new pin, described in 5.2.3.2, had a square cross section where mounted to the arm.

#### 5.2.3.2 Sample preparation

In pin-on-disk wear tests, the pin material is as critical as the disk itself. Each of the candidate bearing materials is to be utilized in an axial piston hydraulic pump with a copper-infiltrated, P/M steel cylinder block. Therefore the pins for the pin on disk wear testing were electrical discharge machined (EDM'ed) from a production cylinder block as shown in Figure 62.

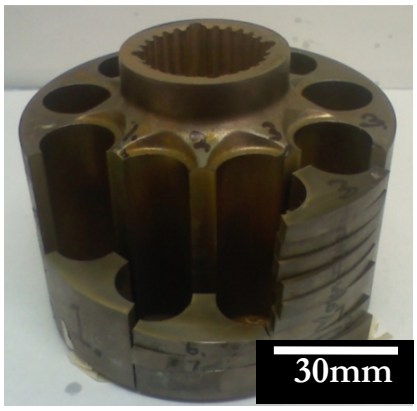


**Figure 62. Pins cut from an axial piston pump cylinder block.**

The design of the pins (Figure 63) was selected to provide a line contact when the wear test is started rather than the point contact of the traditional hemispherical pin. During wear testing, the shallow radius will be flattened slightly to provide an area of contact. The same shallow radius of the pin promotes the formation of a lubricating film of hydraulic fluid similar to that used to lubricate the cylinder block / valve plate interface in axial piston pumps. The face of the pins were ground to with 600 grit polishing paper parallel to the the sliding direction. This resulted in an average roughness (Ra) of 0.169µm (RzDIN 1.593µm, Rmax 2.954µm).

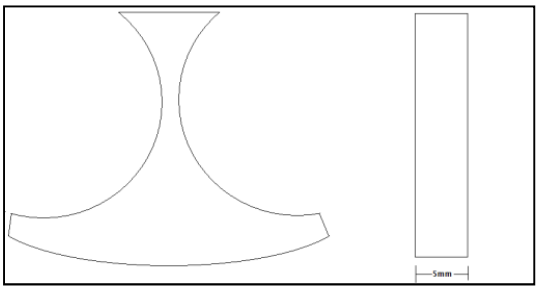

**Figure 63. Drawing of pin for pin on disk.**

The disks for the wear tests were comprised of the production, experimental, and newly developed valve plate materials. Wear testing samples of the Cu-10Sn-10Pb and Cu-10Sn-3Bi bearing bronzes were attained by utilizing production-ready valve valve plates. The leaded bronze valve plates used for the wear tests were production valve plates for Sauer Danfoss' 15 Series axial piston hydraulic pumps. These valve plates were manufactured as previously described and lapped to a surface finish shown in Table 3. The bismuth bronze valve plates used for the pin on disk were produced for the Sauer Danfoss M46 hydraulic pumps. They were flat honed to the surface finish shown in the table.

**Table 3. Surface roughness of the wear test samples.**

| Value(μm) | Cu-10Sn-10Pb | Cu-10Sn-3Bi | Sn/Cu-10Sn and Sn-1.37Mn/Cu-10Sn |
|---|---|---|---|
| Ra | 0.626 | 0.304 | 0.649 |
| RzDIN | 6.416 | 4.493 | 5.949 |
| Rmax | 6.952 | 5.949 | 8.394 |
| Rq | 0.817 | 0.449 | 0.933 |

Wear specimens of the Cu-10Sn/Sn-1.37Mn and Cu-10Sn/Sn materials were created in a manner similar to the smaller samples used for initial alloy development. Tin-bronze powder was pressed at 350MPa in a 40.6mm diameter double-acting carbide die. The samples were sintered under a vacuum of $10^{-6}$ Torr at 650°C for 2 hours to form 10mm thick disks. The disks were then coated with approximately 5 grams of pastes consisting of either Sn-1.37Mn or pure tin powder in Johnson's E127 flux. Each was placed on a hot plate at 250°C and allowed to reflow under argon before being mass quenched. After this process, the excess tin was ground from the surface and the disk was polished to a surface roughness shown in Table 3 by grinding through 600 grit polishing paper, then roughing the surface with 400 grit paper to ensure uniformity.

#### 5.2.3.3 Testing procedure

Before each wear test, the hydraulic oil was preheated to reach a minimum of 90°C. As the oil was heating, the sample was clamped onto a steel disk. The steel disk was designed to set onto retaining pins of the shaft of the tribometer. After the bronze sample was secured to the plate, it was placed on the tribometer and brought up to speed and the oil flow was started and

stabilized at about 500mL/min. This allowed the oil to bring the sample and catch pan up to temperature.

As this was happening, the pin was secured into the arm of the tribometer. Adjustments were made so that the pin lay as flat as possible on the surface of the disk. The arm was loaded with a 3kg weight. After the system was aligned this resulted in a load of 1745g on the pin. Calculation of the hertzian contact stress was performed using the equations from Stachowiak, assuming parallel contact of two cylinders (Stachowiak et. al. 2005). In this case the flat disk was assumed to be a cylinder of infinite radius. The load on the pin results in a contact area of 12.88mm$^2$ and an average contact stress between the pin and disk of 1.32MPa. The maximum contact stress was calculated to be 1.69MPa. Both of these values fell within the range of stresses (1.290 MPa to 2.54 MPa) present on the bearing surface in the axial piston hydraulic pumps used for this study (Sauer, 2008).

Once the system is warmed up, the radius of the wear track was set. The radius was set based on the geometry of the sample. Since the diameter of the tin infiltrated samples was limited to approximately 40mm, a slightly smaller diameter (17.6mm) was used to ensure full contact of the pin on the disk. The leaded bronze (Series 15 valve plate) samples were tested using the same radius. The M46 based Cu-10Sn-3Bi valve plates had a minimum radius of 28.1mm because of their design. Regardless of the radius of the wear track, each sample was set up to create a 50 cm/s sliding speed. Samples were then run for a 1000m sliding distance before being removed, cooled, and cleaned using a solvent.

Since the bismuth bronze wear track was necessarily of a larger diameter, the same 1000 meter sliding distance required fewer revolutions. In fact, the bismuth bronze sample turned only approximately 5600 revolutions. Compared to the 9750 revolutions the leaded bronze and tin-infiltrated bronze rotated to travel 1000 meters, the bismuth material experience far fewer passes by the Cu-infiltrated P/M steel pin. The pin and disk experienced the same sliding distance as the other two samples and are thus comparable for volume loss, but to make the wear on the disk comparable, an additional wear test of the bismuth bronze was performed to a sliding distance of 1750 meters. This provided nearly the same 9750 passes that the other samples experienced so the damage on the valve plate surface would be comparable.

#### 5.2.3.4 Sample evaluation

The 1000m wear test specimens of the leaded bronze and infiltrated tin bronze along with the 1740m bismuth bronze valve plate sample were evaluated optically and using scanning electron microscopy to determine the nature of the wear. Each of these samples had been passed over the same number of times by the pin. The 1000m wear test specimens of each material were used to determine volume loss of both the pin and disk specimens using profilometry. The HommelWerke LV-50 profilometer was used to profile across the diameter of the sample in three traces approximately 120° apart. The traces were then evaluated using the HommelWerke TurboRoughness software. Each trace was then used to determine the inner and outer radius of the wear track. The software was also used to calculate the area for each of the six wear track cross sections that resulted, as shown in Figure 64.

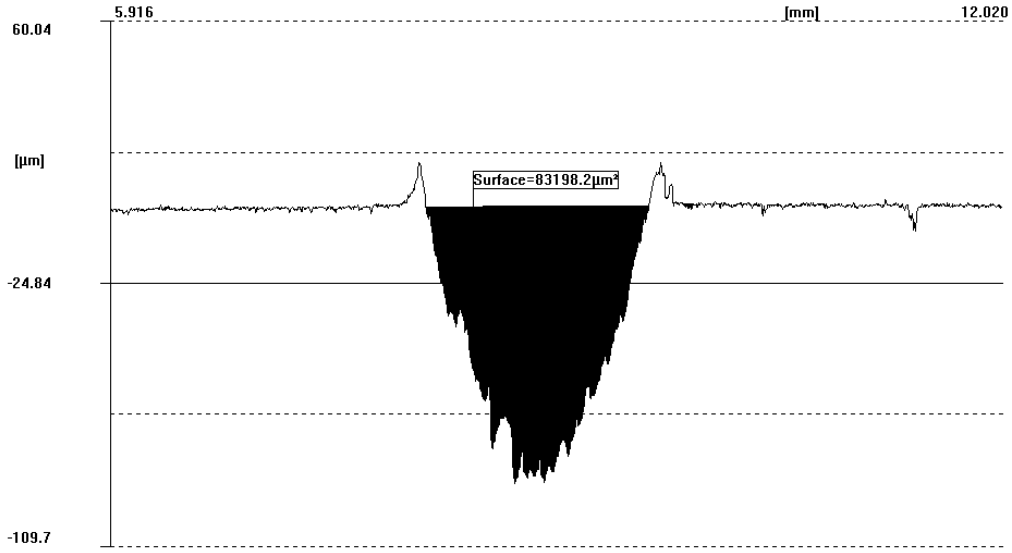


**Figure 64. Evaluation of the area of a wear track profile.**

The wear volume loss was calculated using each of those six areas. This was done by assuming a revolved rectangular cross section with the distance from the axis of revolution for its inner and outer edges being equal to the values of the inner and outer radii of the wear track (Figure 65). The volumes were then averaged for the final result.

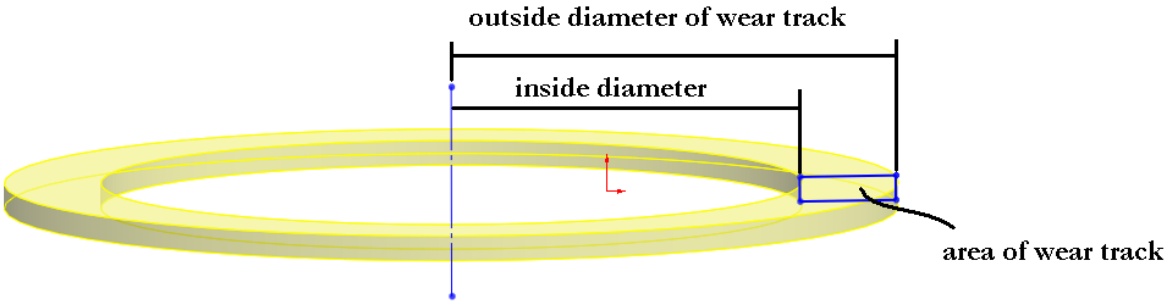


**Figure 65. Calculation of volume loss from wear tests.**

The volume loss for the lubricated pins was calculated by measuring the width of the wear scar. This measurement was used along with the known radius of the pin curvature to calculate the area of the missing cross section. That value was then multiplied by the measured width of the pin to calculate the volume removed.

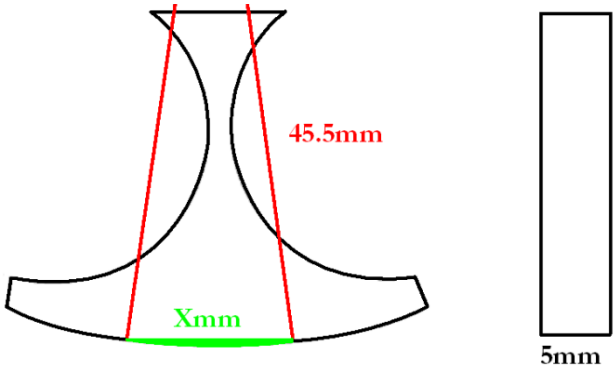


**Figure 66. Calculation of pin volume loss from lubricated wear tests.**

### 5.2.4 Dry Wear Testing

Further characterization of the tin alloy infiltrated bronzes was done using dry sliding wear tests. Two sets of tests were performed. The first was designed to be easily replicable using standard tribometers, and was performed according to ASTM standard G-99. The tests were performed sliding against pins made from 52100 bearing steel at relatively high loads and slow speeds. The second set was designed to test the sliding characteristics of the alloys against the proprietary copper-infiltrated P/M steel at high sliding velocities in completely dry conditions.

#### 5.2.4.1 Equipment

Samples were wear tested on the standard Falex ISC250PC tribometer shown in Figure 18. The tribometer is limited to approximately 320 RPM and hanging weights around 2kg. These values determined the maximum parameters for the wear tests.

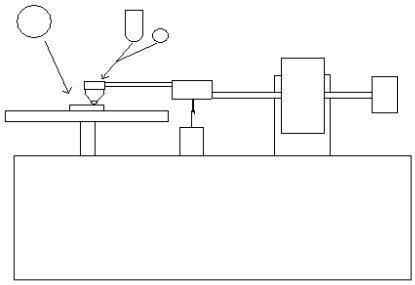

**Figure 67. Arrangement of the Falex tribometer for dry sliding tests.**

#### 5.2.4.2 Sample preparation

Disk samples for each set of tests were prepared in the same manner as those in the lubricated tests described in section 5.2.3.2. For the pins, standard 6.35mm bearing balls of SAE 52100 bearing steel. For pins of the proprietary copper-infiltrated P/M steel, rods were electrical discharge machined from a production cylinder block. Hemispherical ends were then machined in the rod and trimmed off to create the pin shown in Figure 68. These pins were then ground using 600 grit polishing paper in a lathe for proper surface roughness.

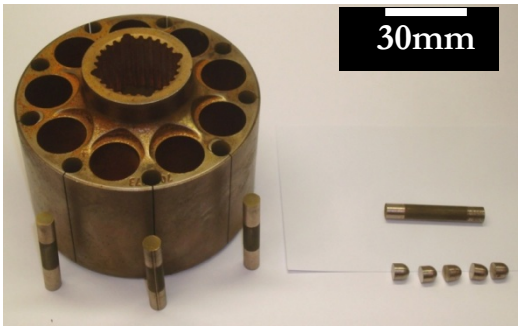


**Figure 68. Wear test pin made from the proprietary copper-infiltrated P/M steel.**

#### 5.2.4.3 Testing procedure

Although ASTM standard G-99 allows for any normal force, speed, and distance, interlaboratory tests used 10mm balls, 40mm disks, 10N of force, a velocity of 0.1m/s, and a sliding distance of 1km. An attempt was made to replicate these conditions for the first set of tests, however limitations prevented a direct match. The available SAE 52100 pins were 6.35mm in diameter, increasing the stress on the disk specimens. The calculated maximum hertzian stress for the 6.35mm pins with 10N of load is 402MPa, compared to 297MPa for 10mm pins. Since the exact conditions could not be replicated, the specimens were run for 500m at a velocity of 0.1m/s with 10N of force. Sample disk size varied slightly because of the geometry of the valve plates and compacted bronze specimens.

For the high speed tests, each of the materials was tested using a 6.35mm diameter pin of the proprietary copper-infiltrated P/M steel. The specimens were run at a velocity of 0.5m/s for a sliding distance of 1000m with 1N of force on the pin. The calculated maximum hertzian stress for this condition was 187MPa.

#### 5.2.4.4 Sample evaluation

Samples from the dry sliding wear tests were evaluated in the same manner as the lubricated tests. The methods are described in Section 5.2.3.4.

## 5.3 Results

### 5.3.1 Thermal Aging Testing

Porous bronze compact infiltrated with both Sn-1.37Mn and pure Sn had similar initial intermetallic layer thickness if processed properly, i.e. kept near the 250˚C reflow temperature for the shortest possible time. As-infiltrated tin-manganese samples (Figure 69a) had an average intermetallic thickness of 870nm that consisted entirely of $Cu_6Sn_5$. Samples infiltrated with pure tin had a slightly higher average intermetallic thickness of 1μm that was also $Cu_6Sn_5$. The pure tin infiltrated samples are shown in the as-infiltrated condition in Figure 69b.

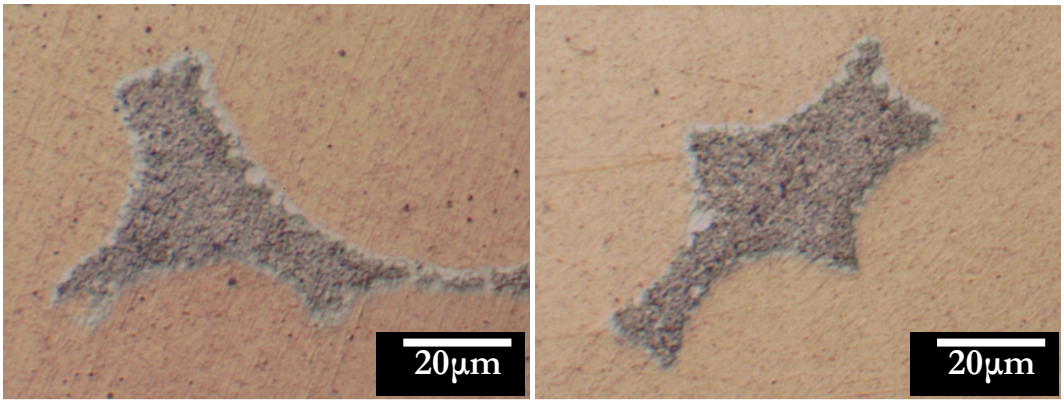


(a) (b)

**Figure 69. Unaged a) Sn-1.37Mn and b) Sn infiltrated pockets.**

After being aged for 100 hours, the pockets in the Sn and Sn-1.37Mn infiltrated samples appear as shown in Figure 70. The aged pure Sn infiltrated samples had an 3µm average intermetallic thickness. Of that thickess, approximately 1.4µm was comprised of the detrimental $Cu_3Sn$ intermetallic. In contrast, the aged Sn-1.37Mn pockets had an average intermetallic thickness of 2.6µm with a 350nm $Cu_3Sn$ intermetallic thickness, a significant reduction in $Cu_3Sn$ compared to the pure tin samples.

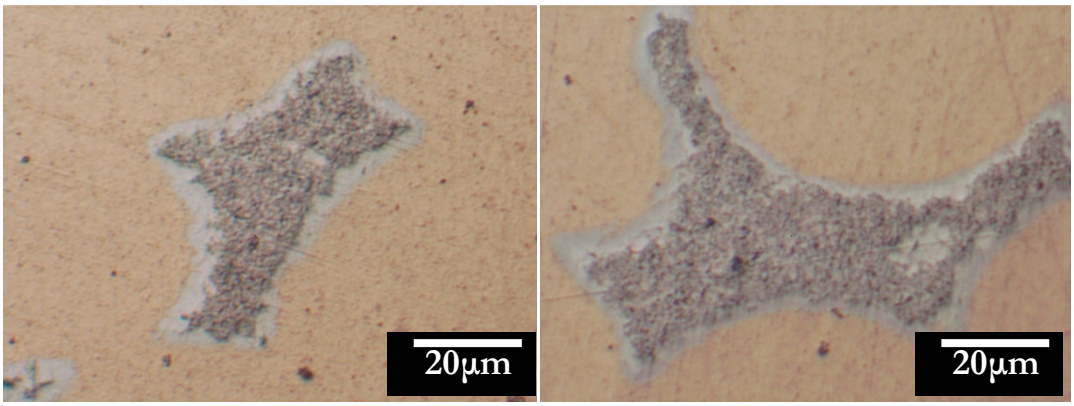


(a) (b)

**Figure 70. 100 hour aged a) Sn-1.37Mn and b) Sn infiltrated pockets.**

The 750 hour samples shown below in Figure 71 reflect a similar effect. Both the pure tin and the tin-manganese pockets have similar average intermetallic thicknesses. The pure tin pockets have an overall intermetallic thickness of 5.2µm and the Sn-1.37Mn pockets have an average thickness of 4.9µm. The more substantial difference comes in the suppression of the

$Cu_3Sn$ layer. In the pure tin pockets, this layer is 2.7μm thick. However the Sn-1.37Mn pockets have a $Cu_3Sn$ layer that is only 1.7μm thick.

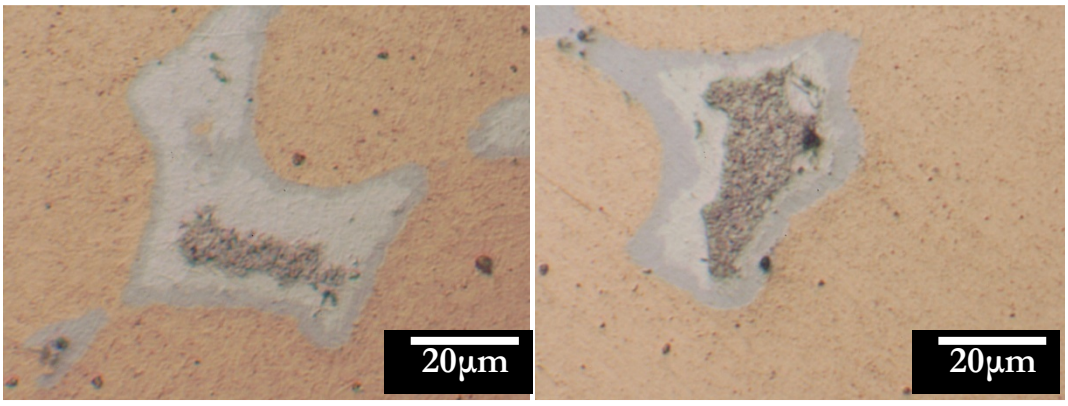


(a) (b)

**Figure 71. 750 hour aged a) Sn-1.37Mn and b) Sn infiltrated pockets.**

The results of the transverse rupture strength tests are tabulated in Table 4. There are two noticeable trends that arise from the data. The first is that the sample sintering temperature primarily affects the fracture toughness (and with it, ultimate strength). The second is that the compaction pressure has a large effect on the yield strength and elastic modulus, along with an increase in fracture toughness and ultimate transverse rupture strength, of the bronze.

### 5.3.2 Strength Testing

**Table 4. Mechanical data from TRS tests.**

| Sample | Elastic Modulus (GPa) | Ultimate Strength (MPa) | Yield Strength (MPa) | Elongation (%) |
|---|---|---|---|---|
| 700MPa/780C/4hr | 12.7 | 710 | 250 | 41 |
| 700MPa/780C/2hr | 11.8 | 670 | 240 | 41 |
| 700MPa/650C/2hr | 11.1 | 520 | 240 | 24 |
| 550MPa/780C/2hr | 8.0 | 600 | 235 | 41 |
| 550MPa/700C/2hr | 7.2 | 560 | 235 | 32 |
| 350MPa/780C/2hr | 5.3 | 375 | 160 | 28 |
| 350MPa/650C/2 hr | 6.0 | 245 | 130 | 13 |
| 350MPa/650C/2 hr/Sn-infused | 5.3 | 250 | 155 | 11 |
| 350MPa/650C/2 hr/Sn-infused/aged 100hrs | 4.5 | 230 | 180 | 7 |
| Cu-10Sn-10Pb | | 300 | 230 | 7 |
| Cu-10Sn-3Bi | | 410 | 280 | 22 |

### 5.3.2.1 Effect of Compaction and Sintering Parameters on Strength

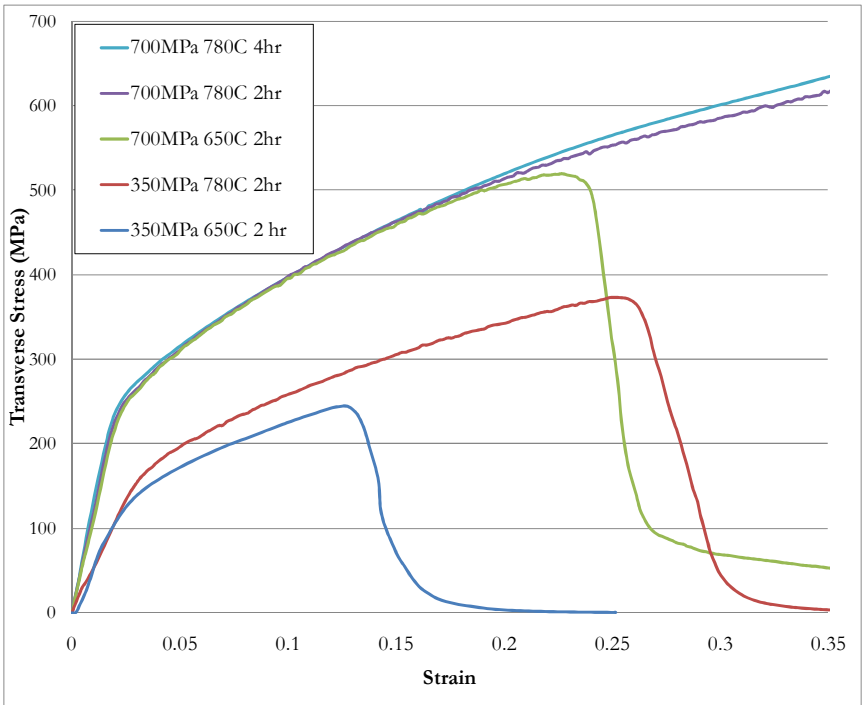


**Figure 72. Transverse stress vs. strain for various compaction and sintering values.**

The 700MPa/780˚C/4hr sample was created to be a full density compact representing the maximum achievable strength (in the as-sintered condition). Both this sample and the 700MPa/780˚C/2hr sample failed to fracture with a 5mm deflection (Figure 73a). According the ASTM specification, if any sample deflects more than 0.2in (5.08mm) without fracture, the results are questionable. At that point, the sample is partially supported by the fixture itself so the numbers reflect the strength of the fixture, not the sample. Each of the 700MPa/780˚C samples was able to withstand a stress of over 650MPa without fracture.

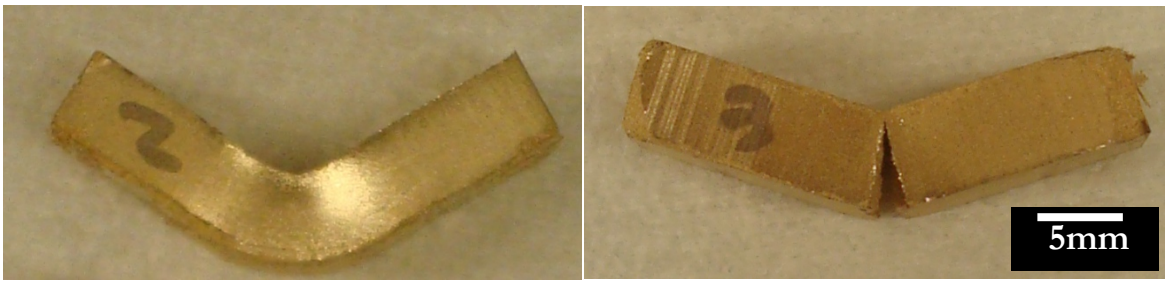


(a) (b)

**Figure 73. Example TRS specimens a) 700MPa/780˚C/2hr and b) 350MPa/650˚C/2hr.**

Decreasing the sintering temperature from 780˚C to 650˚C resulted in the same elastic modulus and yield strength but the samples fractured (Figure 73b) at an average stress of 520MPa at 24% elongation (on the lower face). The effect of lowering the sintering temperature was also evident in the samples compacted at the low, 350MPa pressure. Specimens sintered at 780˚C failed at an average of 370MPa and 28% elongation. When sintered at 650˚C, the transverse rupture strength dropped to 245MPa and the samples only achieved an elongation of 13%.

The increased fracture toughness in the 780˚C was likely the combined effect of a slight increase in particle contacts and neck size with more highly annealed copper prior powder particles. The increased sintering temperature can move the grain boundaries past the necked region, strengthening the connection. The smaller neck diameters in the 650˚C TRS bars act as a stress concentration that work hardens during fracture, aided by the intrinsic dislocations and grain boundaries, resulting in lower toughness. The difference in fracture morphology with sintering temperature is visible in SEM micrographs of the fracture surface (Figure 74).

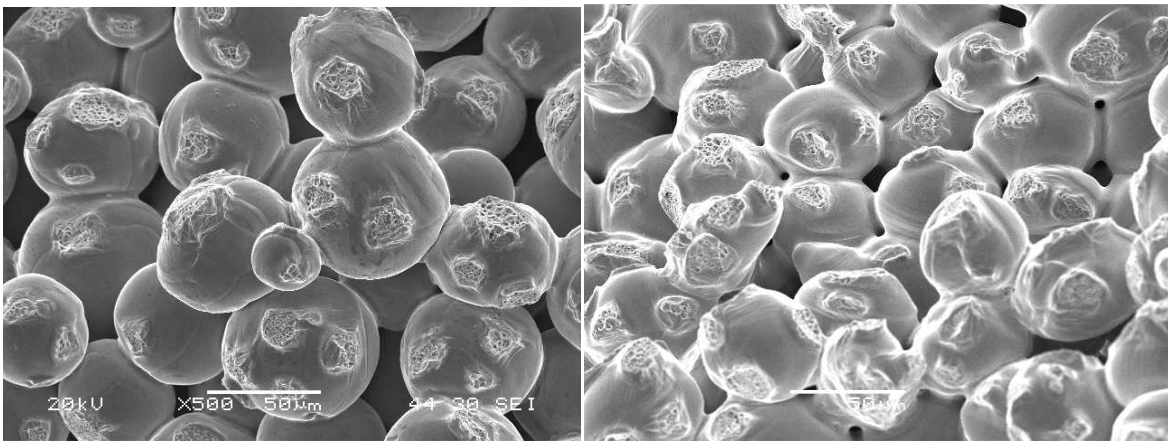


(a) (b)

**Figure 74. Fracture surfaces of 350MPa a) 650˚C and b) 780˚C sintered TRS bars.**

There was also a significant difference in the yield strength and elastic modulus of the transverse rupture specimens between the 350MPa and 700MPa compaction pressures. This was correlated with the increase with compaction pressure primarily because of the increase in the overall density of the specimen. Increased pressure deforms the powder to fill porosity during compaction. The deformation of the powder particles during pressing not only increases the number of particles per unit volume, but also increases the number of contacts these particles

have with their neighbors. Thus the increase in the thickness and number of sintered necks per unit area increases the elastic modulus in the same way a thicker spring requires more force to depress. Stress concentrations are also reduced by the increase in true area of contact, increasing the fracture toughness and ultimate transverse rupture strength.

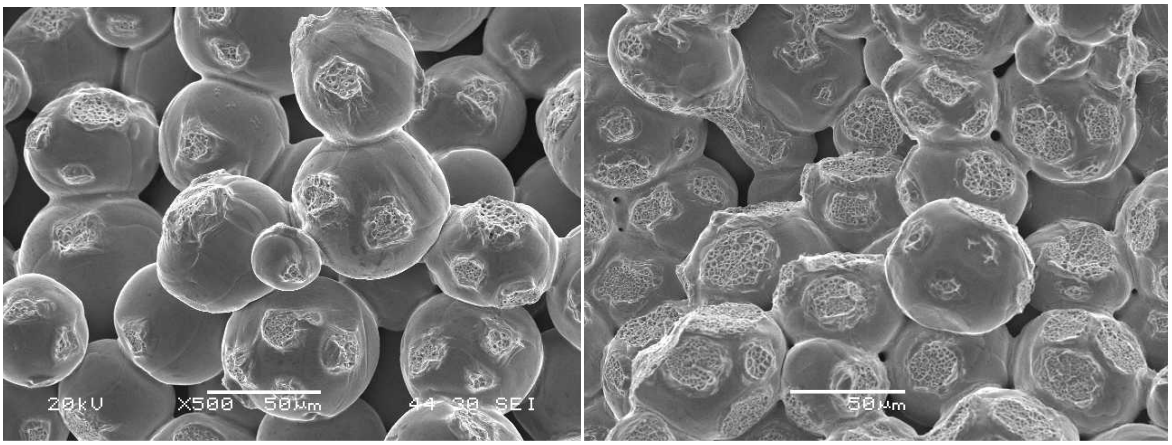


(a) (b)

**Figure 75. Fracture surfaces of 650˚C sintered a) 350MPa and b) 700MPa TRS bars.**

The results of the initial strength tests of sintered bronze compacts using the minimum and maximum compaction and sintering values showed that a large variation in mechanical properties was achievable. An understanding of these parameters would be critical to develop the correct balance of strength and porosity for a bearing alloy. The bronze used for the infiltration exercise in Section 4.5 were pressed at 350MPa and sintered at 650˚C for maximum interconnected porosity (as seen in Figure 75a) but have very minimal strength as a result.

#### 5.3.2.2 Mechanical Properties Achievable with Interconnected Porosity

It was shown in Section 4.4 that infiltration was possible in samples pressed at 550MPa and sintered for 2 hours at 780˚C. Strength tests of bronze specimens created in this manner are shown in Figure 76 to compare the effect of intermediate compaction and sintering parameters on the mechanical properties of the bronze. The data, shown in red, shows that 550MPa/780˚C/2hr samples have an apparent elastic modulus and yield strength that fall between those that result from compaction at 350MPa and 700MPa. Like the 700MPa samples sintered at 780˚C, the 550MPa/780˚C/2hr samples were strong enough to withstand the transverse rupture test without fracture.

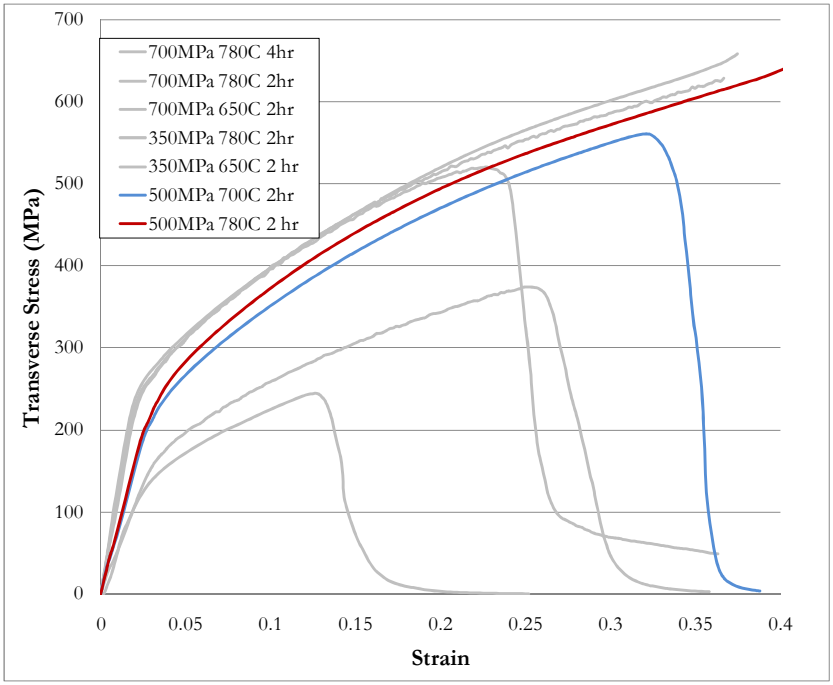


**Figure 76. Fracture surfaces of 550MPa compacted a) 780˚C and b) 700˚C TRS bars.**

This result showed promise for the increase in mechanical strength of future bearing bronzes. It was shown in Figure 48 (Section 4.4.2) that infiltration was not even throughout the sample because of partially closed off porosity visible on the fracture surface in Figure 77. Lowering the sintering temperature by 80˚C greatly increases the interconnected porosity in the sample and achieves a yield strength of 235MPa and transverse rupture strength of 520MPa (a 180% higher yield strength than the 350MPa/650˚C/2hr bronze that was used for infiltration in Section 4.5)

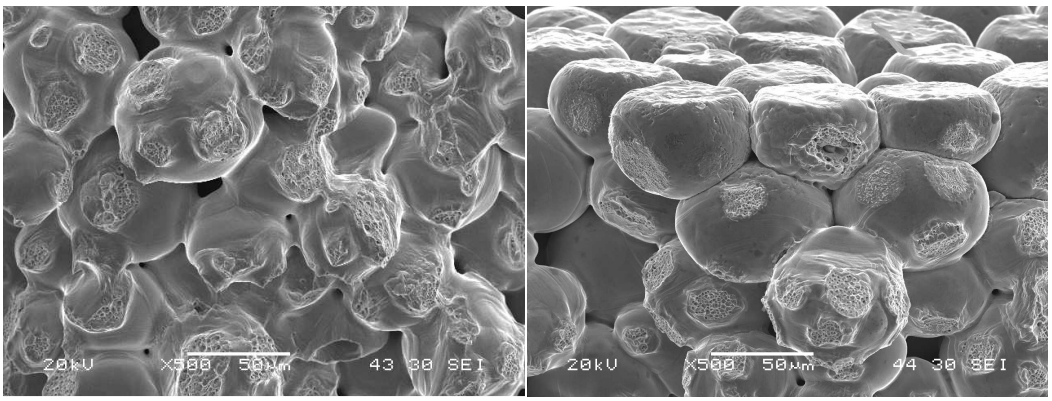


(a) (b)

**Figure 77. Fracture surfaces of 550MPa compacted a) 780˚C and b) 700˚C TRS bars.**

### 5.3.2.3 Effect of Infiltration on Mechanical Strength

It was also useful to understand the effect of tin alloy infiltration on the strength of the bearing material. The results of transverse rupture tests on infiltrated 350MPa/650˚C/2hr samples are shown in Figure 78. The as-sintered bronze compact had an transverse rupture strength of 245MPa and elongates 13%. When infiltrated with tin, the TRS was increased slightly. Increase of the effective area was most likely the cause for this increase. Although the strength improved, the ductility decreased in infiltrated samples.

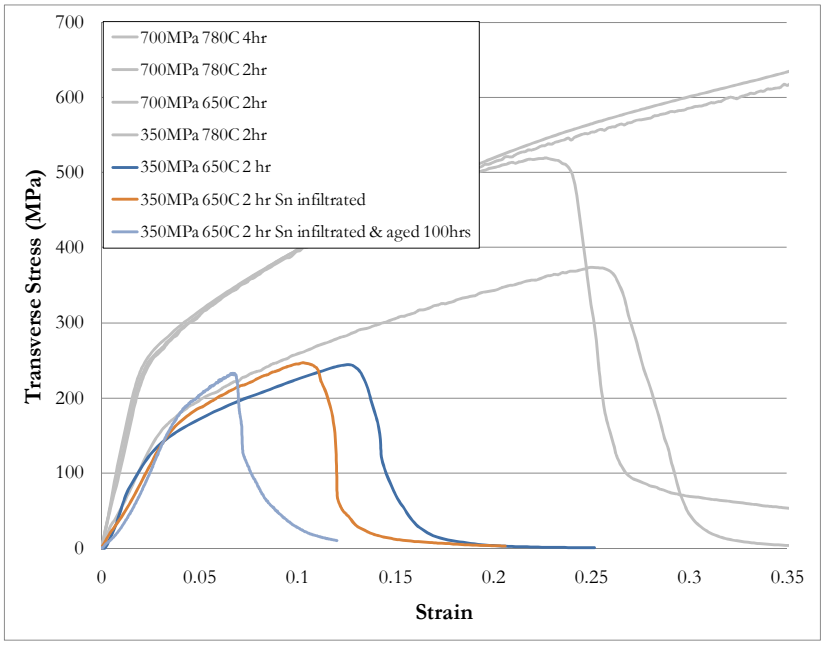


**Figure 78. Effect of tin infusion on transverse rupture strength.**

The decrease in ductility was the result of intermetallic $Cu_6Sn_5$ growth near the necks that created a fracture path for brittle fracture (Figure 79a). The effect of $Cu_6Sn_5$ and possibly $Cu_3Sn$ intermetallics was more pronounced after the samples were aged at 130˚C for 100 hours. This temperature is adequate to encourage the growth of these intermetallic phases. Figure 77 compares the fracture surface at the neck between bronze particles in two samples initially prepared by compacting at 350MPa and sintering for 2 hours at 650˚C. The samples that were infiltrated with pure tin and aged for 100 hours at 130˚C (Figure 79b) had a reduced ductile fracture contact that is surrounded by the brittle fracture surface of the intermetallics.

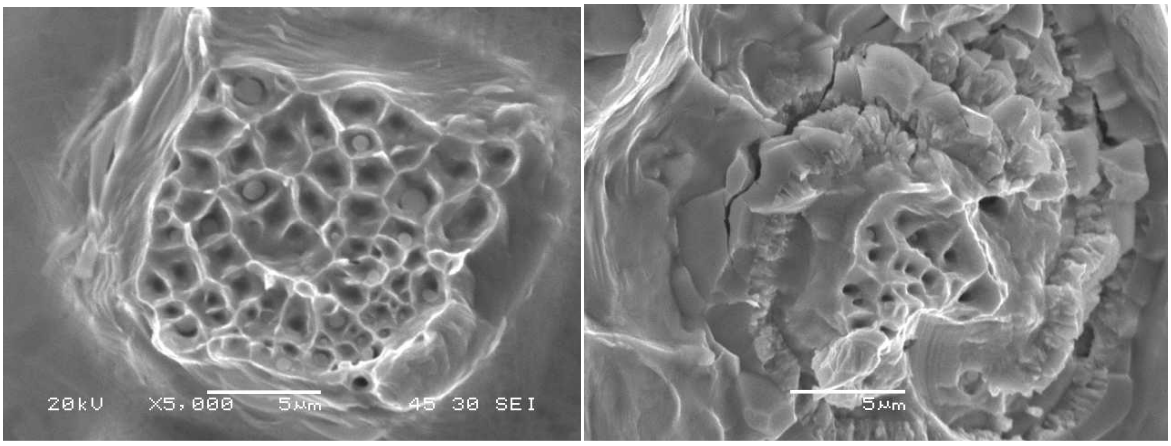


(a) (b)

**Figure 79. Necks of 350MPa/650˚C/2hr a) as sintered and b) infiltrated & aged 100hrs.**

#### 5.3.2.4 Powder Contamination

It was also noted, while examining the fracture surfaces of each of the specimens, that the fractured necks had a cup and cone appearance typical of ductile fracture. However, in laboratory grade bronze powder, one would expect to see very few dimples at each of the necks. In the sintered bronze TRS samples, there were many dimples (Figure 79).

At the center of nearly every dimple were very small (<1µm) spheres (Figure 80). An example of the contaminants in the fracture surface is shown below. Using the EDS capability of the SEM, it was determined that the spheres were comprised of 21.0 wt.% Sn, 18.5 wt.% O, 5.0 wt.% Zn, 0.6 wt.%Fe, 12.0 wt.% Pb, 8.58 wt.% P, and the remainder copper.

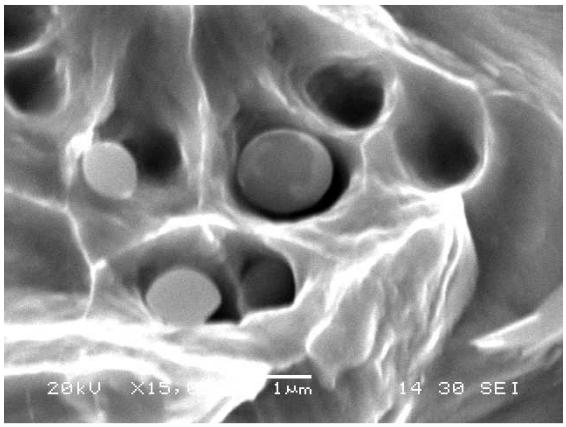


**Figure 80. Contaminants in the fracture surface.**

These contaminants were found to have been picked up during compaction or sintering of the bronze compacts. As-received powder was compared to sintered powder that had fallen off of pressed compacts and onto the alumina tray as they were being loaded into the sintering furnace. Energy dispersive spectroscopy (SEM-EDS) was used to determine the chemical composition of the bronze particles. As-received bronze contained 10.4 wt. % tin and the remainder copper. The composition determined by EDS agreed with that determined by ACuPowder (10.6 wt. % Sn). Phosphorous was not detected in the as-received powder. However as a lighter element, it is more difficult to quantify using EDS. After passing through both the die and the vacuum sintering furnace, EDS detected 1.0 wt. % lead on the bronze powder. The lead would almost certainly be present on the outside of the bronze particles because of its insolubility in copper. If the lead was caught between compacted bronze particles, its insolubility would cause it to spherodize in the neck region, resulting in the fracture morphology previously noted.

Evaluation of sintered bronze necks in a cross-sectioned and polished transverse rupture specimen using the scanning electron microscope shows signs of these contaminants. The backscattered electron images in Figure 81 show small pores along the prior particle boundary at the neck. EDS of the pores (black spots) picks up 1.85 wt. % P, 1.63 wt.% Pb, 15.1 wt. % Sn, and the remainder copper. These results support the theory of a segregating contaminant in the bronze picked up during compaction or sintering.

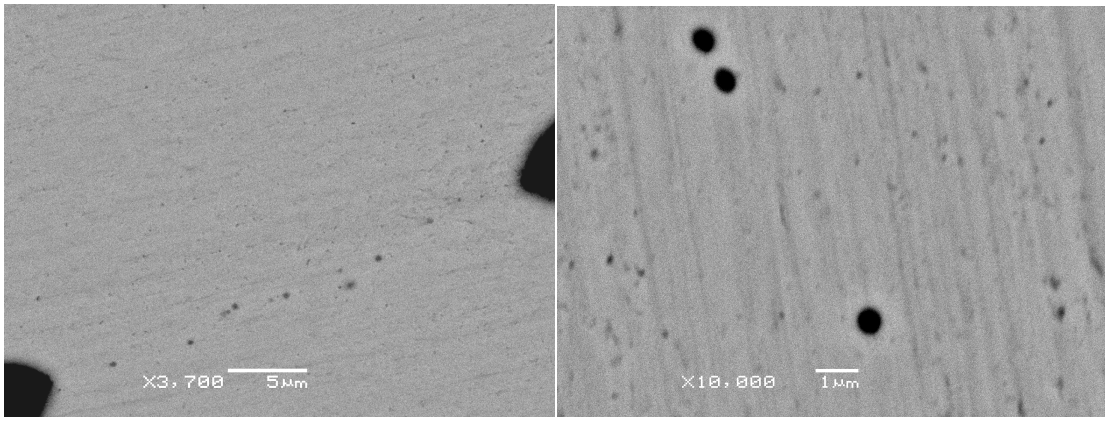


**Figure 81. Contaminants in the fracture surface.**

### 5.3.3 Lubricated Wear Testing

For the first set of wear tests, each material was run in the modified test rig according to the procedure detailed in Section 5.1. The plots below show the resulting friction as a function of time. All three samples exhibited a slight break-in period over the first few meters of sliding. Leaded bronze had the longest of the break in periods, followed by bismuth and tin bronze.

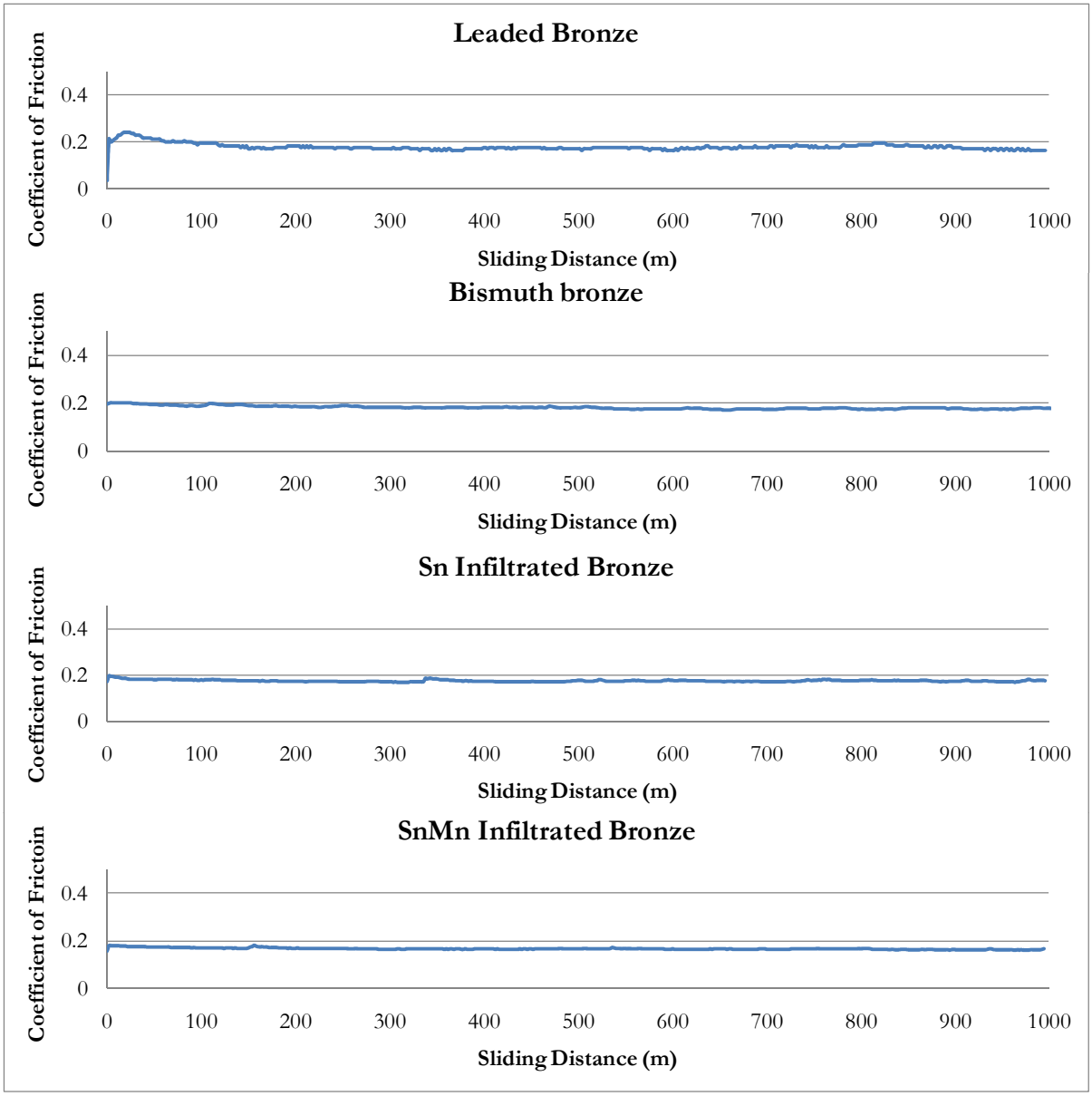


**Figure 82. Plots of friction vs. sliding distance for each of the bearing alloys.**

The average coefficient of friction for each of the materials was similar. The Cu-10Sn-10Pb valve plate material had an average COF of 0.18, the Cu-10Sn-3bi averaged 0.19, and each of the tin infiltrated samples had a coefficient of friction of 0.17. Each of these is comparable and within the error of the friction measurement.

The results of the additional wear test in which the bismuth sample was run for 1750 meters are shown in Figure 83. This test was performed to show the behavior of the wear material in a direct comparison to the leaded bronze and bismuth bronze. The data shows a slight rise in the coefficient of friction near the end of the test however it was deemed insignificant based on examination of the wear track.

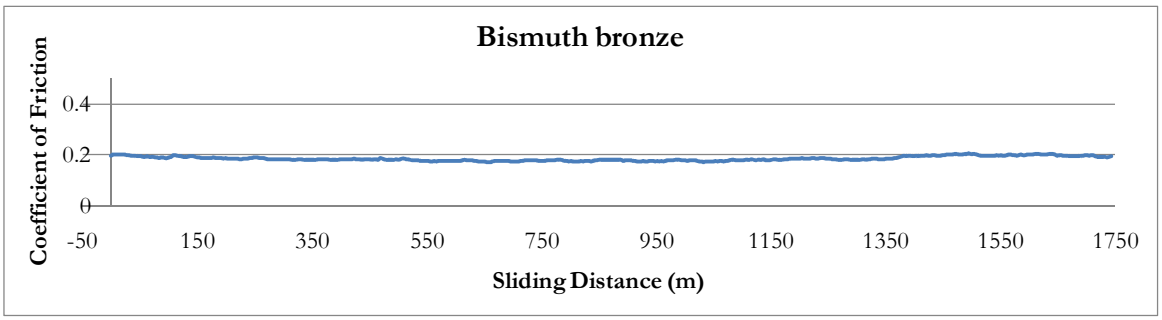


**Figure 83. Plots of friction vs. sliding distance for the long distance bismuth bronze.**

### 5.3.3.1 Optical Microscopy

A representative test specimen for each material is shown in Figure 84-87 after lubricated wear testing, along with the copper-infiltrated P/M steel pin used for the test. The infiltrated samples had similar wear behavior and were treated as one sample for the wear study.

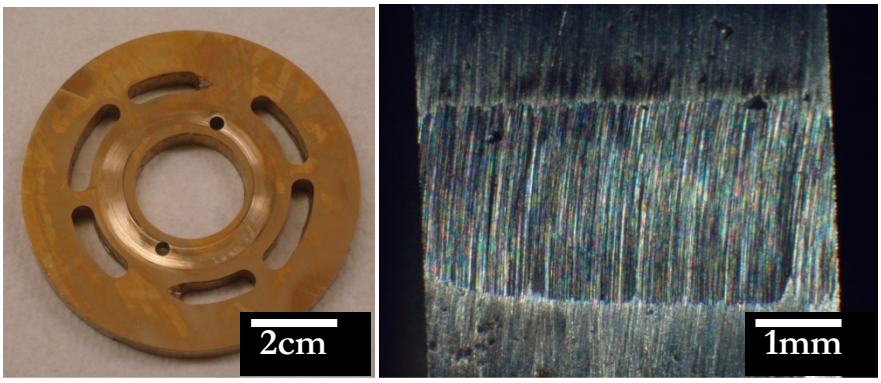


**Figure 84. Worn leaded bronze & Cu-infiltrated P/M steel pin.**

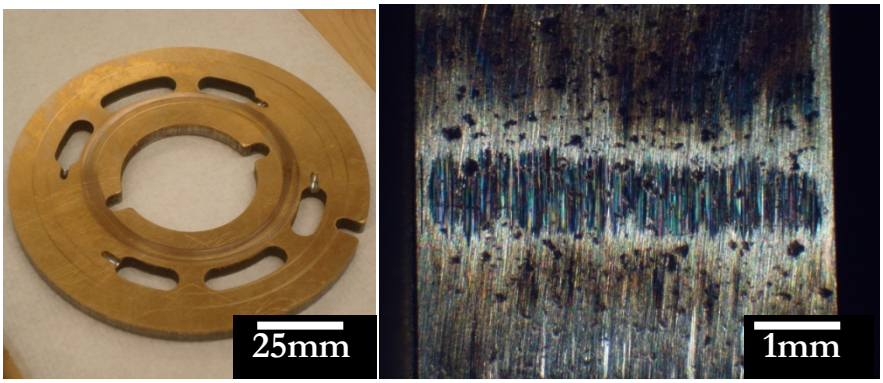


**Figure 85. Worn bismuth bronze & Cu-infiltrated P/M steel pin.**

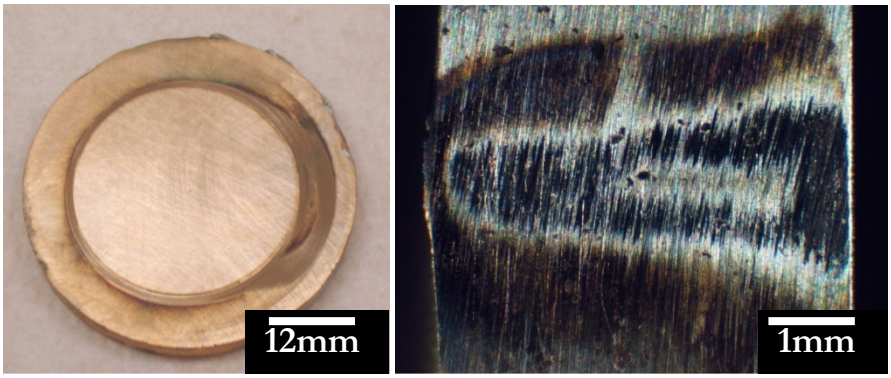


**Figure 86. Worn tin-manganese infiltrated bronze & Cu-infiltrated P/M steel pin.**

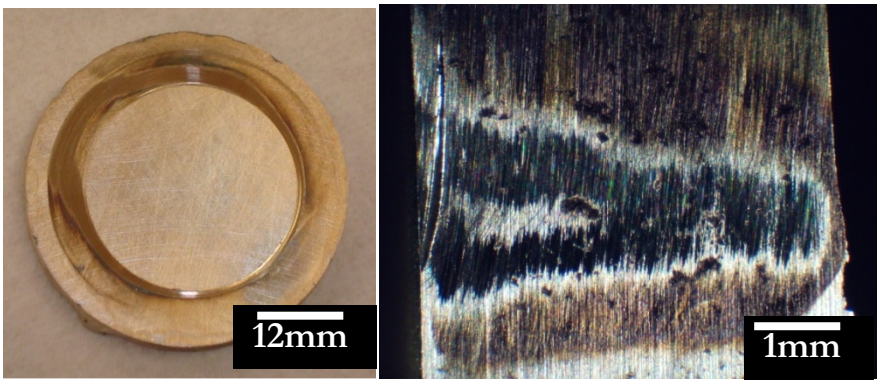


**Figure 87. Worn tin-infiltrated bronze & Cu-infiltrated P/M steel pin.**

#### 5.3.3.2 Profilometry

The results of the calculations of volume loss due to wear are shown in Table 5. The new tin infiltrated bronze (Sn/Cu-10Sn) had the least volume loss of the three materials under lubricated sliding, and resulted in less pin volume loss than the leaded bronze. The high volume

loss in the leaded bronze sample was likely due to deformation in the soft material. The asperities on the surface of the leaded bronze are much deeper than those of the other two materials, allowing the surface to deform more under load.

**Table 5. Lubricated sliding volume loss due to wear.**

| Sample Material | Disk volume loss ($mm^3$) | Pin volume loss ($mm^3$) |
|---|---|---|
| Cu-10Sn-10Pb | 0.612 | 0.201 |
| Cu-10Sn-3Bi | 0.446 | 0.063 |
| Sn/Cu-10Sn | 0.353 | 0.104 |

#### 5.3.3.3 SEM

Each material performed similarly under lubricated conditions. The primary form of wear for the Cu-10Sn-10Pb, Cu-10Sn-3Bi, and Sn/Cu-10Sn bearing alloys was a mixture of plowing and abrasive wear cause by the asperities on the opposing surface. There was, however, a difference in appearance for each of the worn surfaces. The leaded bronze sample, for instance, contained a fair amount of exposed porosity (Figure 88) that the other samples do not.

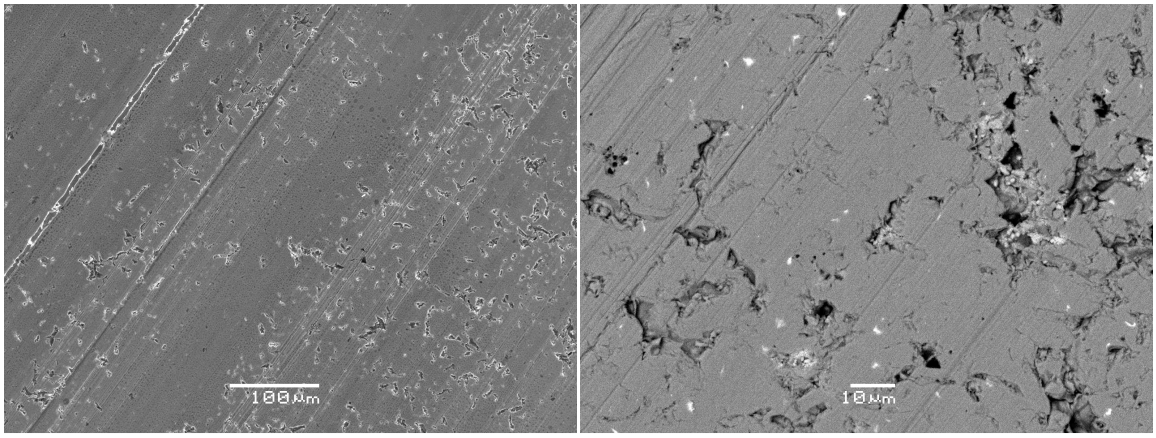


(a) (b)

**Figure 88. The leaded bronze wear track at a) moderate and b) high magnification.**

The exposed porosity on the surface was primarily the result of the surface roughness created by the lapping process used on the leaded bronze material. A profile taken across the wear track perpendicular to the sliding direction is shown in Figure 89. The deep valleys correspond to the visible score marks in Figure 88a. The roughness between those valleys is the result of the exposed porosity on the surface of the wear track. The wear track was shallow enough to have the deepest of the valleys of the surface asperities still present on the surface.

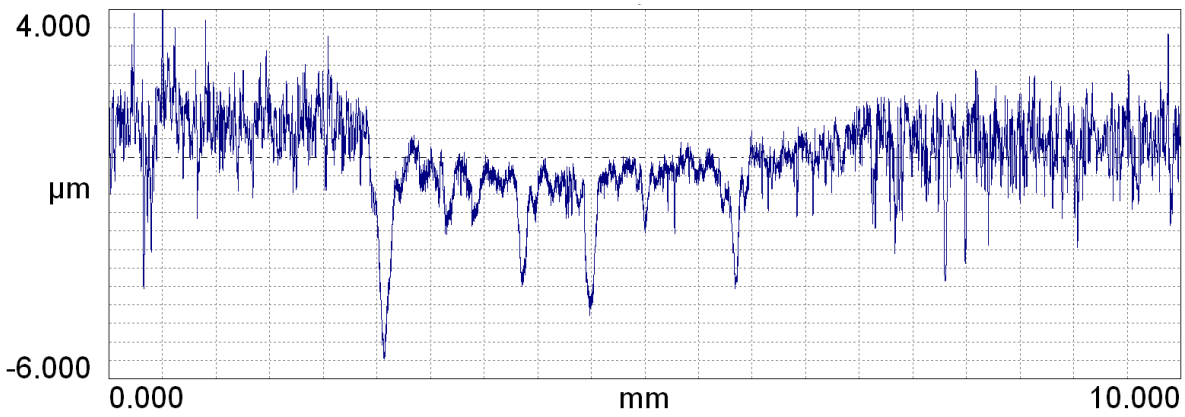


**Figure 89. Profile of the nominal wear track in the leaded bronze valve plate.**

The appearance of the bismuth bronze valve plate is similar under lubricated sliding. The wear track is dominated by abrasive and plowing wear. In this case, the wear scar was deep enough to be beyond the deepest of the asperities on the honed surface of the bismuth bronze (Cu-10Sn-3Bi) valve plate. There were no visible pores or pockets as found in the leaded bronze sample.

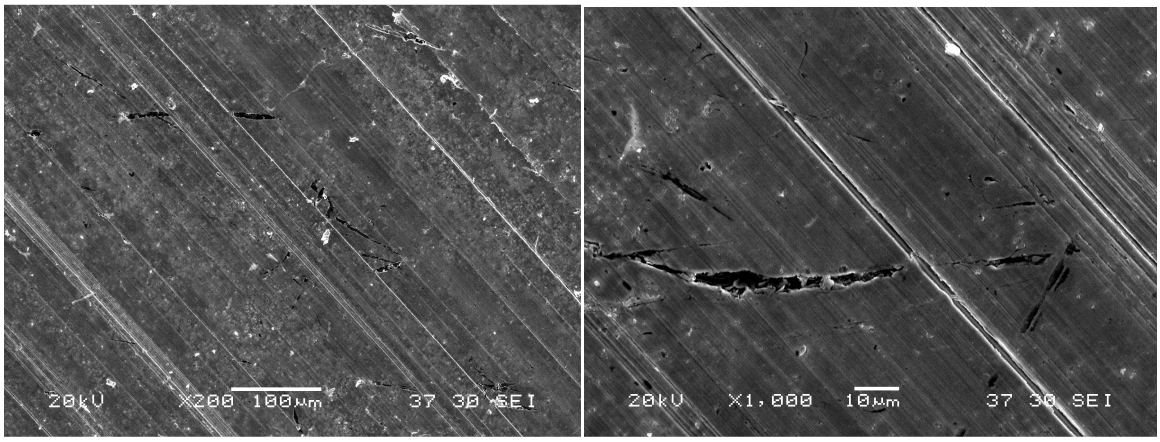


(a) (b)

**Figure 90. The bismuth bronze wear track at a) moderate and b) high magnification.**

Some extraneous damage was noted in the bismuth bronze valve plates. As shown in Figure 90b, fracture-like cracks were found on the surface. These cracks were generally normal to the sliding direction, indicating they may have been caused by the intermittent passing of the pin over the surface. This type of damage was similar to what was observed on the bismuth

bronze valve plates tested in axial piston hydraulic pumps. However, these features may be the result of a few extraneous valleys in the honed surface as seen at 3mm and 8.75mm in Figure 91.

The images in Figure 90 were taken at the deepest portion of the wear track. The surface finish of the honed bismuth bronze valve plates is smooth enough that the wear track was below the vast majority of the lowest valleys in the surface, although some of the deepest may still be present, so there was no exposed porosity as there was in the leaded bronze sample.

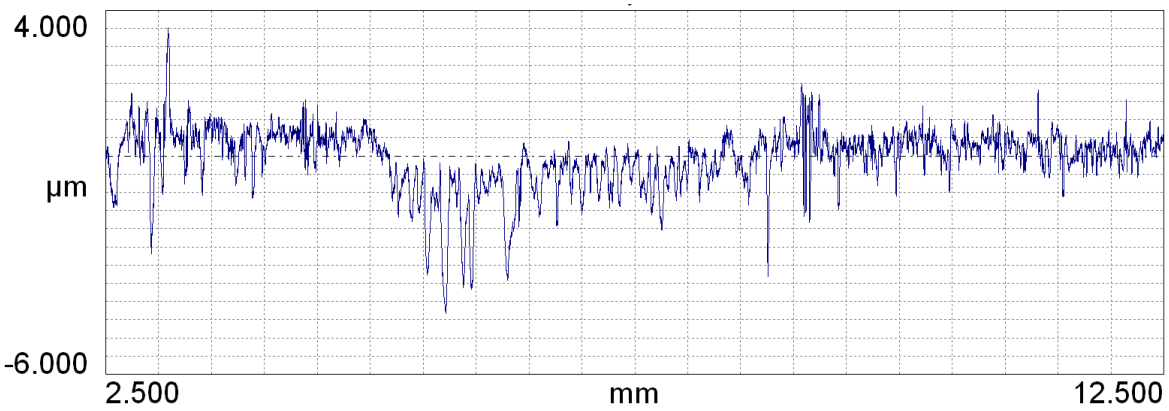


**Figure 91. Profile of the nominal wear track in the bismuth bronze valve plate.**

The tin infused bronze samples produced as a replacement for the leaded and bismuth bronzes showed a similar overall wear pattern (Figure 92), again characterized by abrasive and plowing wear. Similar to the bismuth bronze sample, the wear track was below the surface roughness, so the presence of surface asperities was eliminated.

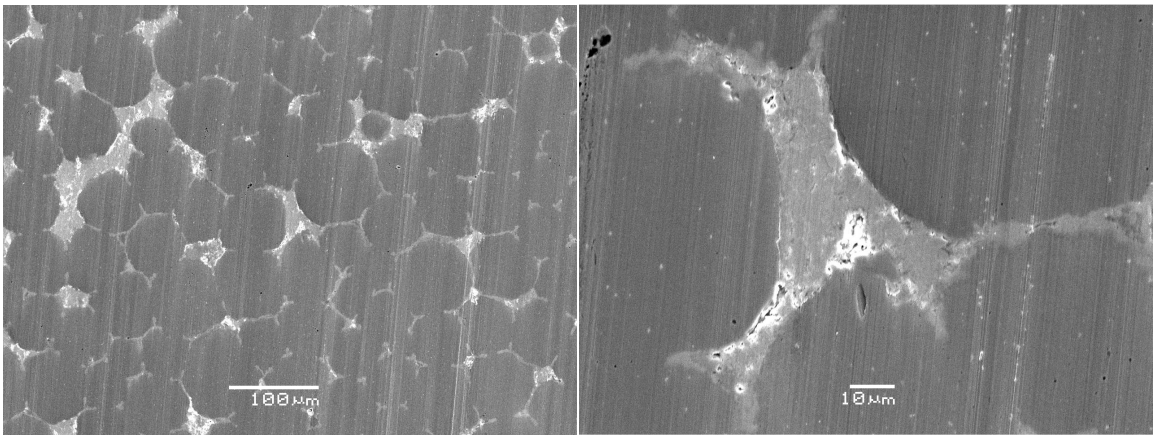


**Figure 92. Appearance of the tin infiltrated bronze wear track in the SEM.**

The primary difference in the tin infiltrated bronze (Sn/Cu-10Sn and Sn-1.37Mn/Cu-10Sn) samples was dominant presence of the soft phase. In the higher magnification image to the right in Figure 92, it can be noted that a small portion of the $Cu_6Sn_5$ that once rimmed the pore was pulled out. The $Cu_6Sn_5$ appeared to have been on the surface in the form of sub micron particles. Tin also appears to have been drawn onto the surface. The presence of either the $Cu_6Sn_5$ particles or the free tin could not be confirmed with EDS because of their scale.

The morphology of the soft phase in the wear track of the tin infused bronze wear sample is quite different from the leaded and bismuth bronzes, as shown in Figure 93.

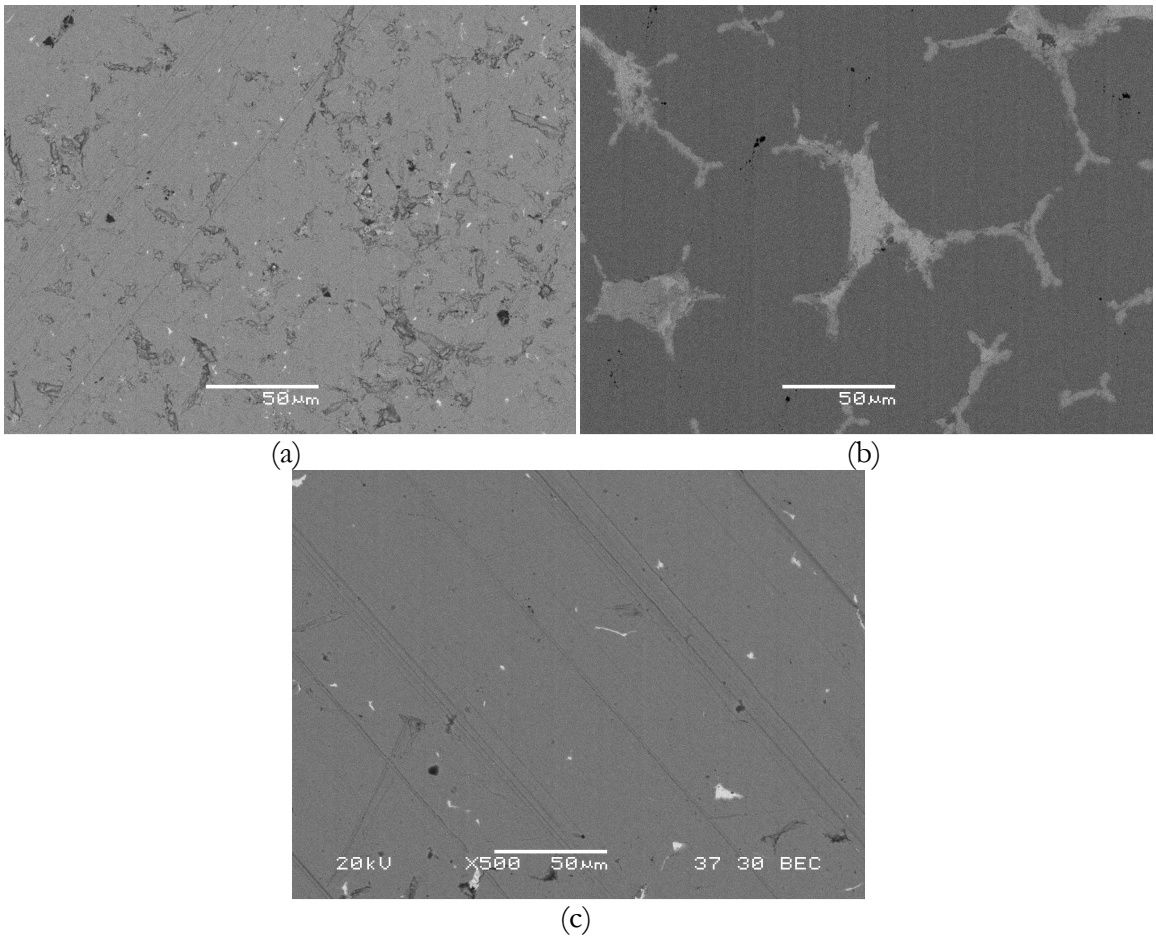


(a) (b)

(c)

**Figure 93. Soft phases in a) Cu-10Sn-10Pb b)Sn/Cu-10Sn and c) Cu-10Sn-3Bi tracks.**

Although the distribution of soft phases appears different in the wear track, comparison of the visible soft phase in the Sn/Cu-10Sn wear sample shows that it was nearly identical to that produced in the original infiltration samples (Figure 94). Those original production samples were

compared to the leaded and bismuth bronze valve plate microstructure in Figure 59 (Section 4.5.2.2) and were very similar. The deformation of the bronze material in the leaded and bismuth bronze likely masks the soft phase. In the tin infiltrated bronze, the fine, hard intermetallic particles produced by the breakup of the rim of intermetallics in each pocket may act as a mild abrasive. These particles are not large enough to affect the wear rate, but scour the surface of the wear track keeping it free of adhesive bronze and exposing the soft phase.

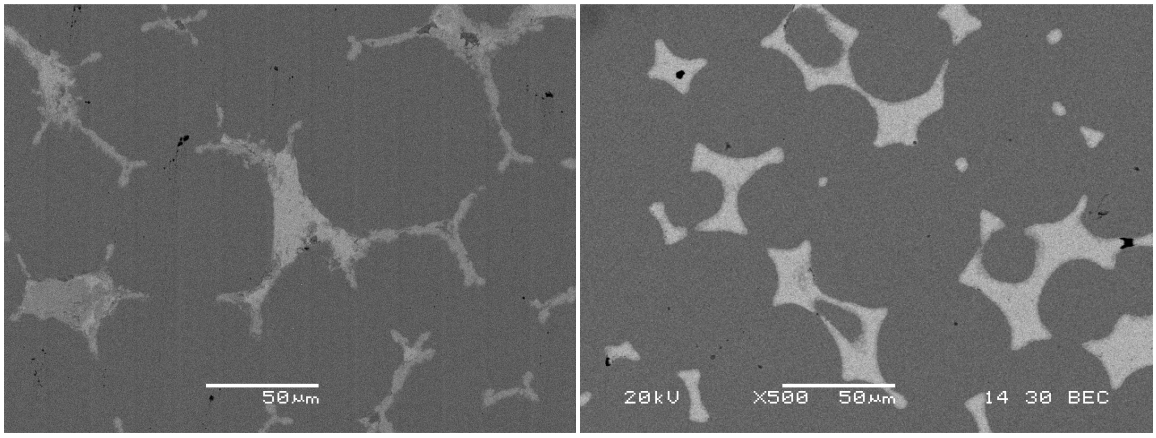


(a) (b)

**Figure 94. Soft phase distribution on the a) wear track and b) polished of Sn/Cu-10Sn.**

### 5.3.4 Highly Loaded Dry Wear Testing

The second set of wear tests was performed using the standard Falex tribometer pin on disk setup according to the procedure detailed in Section 5.1. The plots below show the resulting friction as a function of time. The leaded bronze showed the lowest friction (0.32 average) throughout the test and was relatively stable throughout. The tin infiltrated sample was even more stable through the wear test, but had a slightly higher coefficient of friction at 0.37. The bismuth sample started out with a coefficient of friction around 0.25 but rose to a fairly stable 0.45 after 200 meters of sliding.

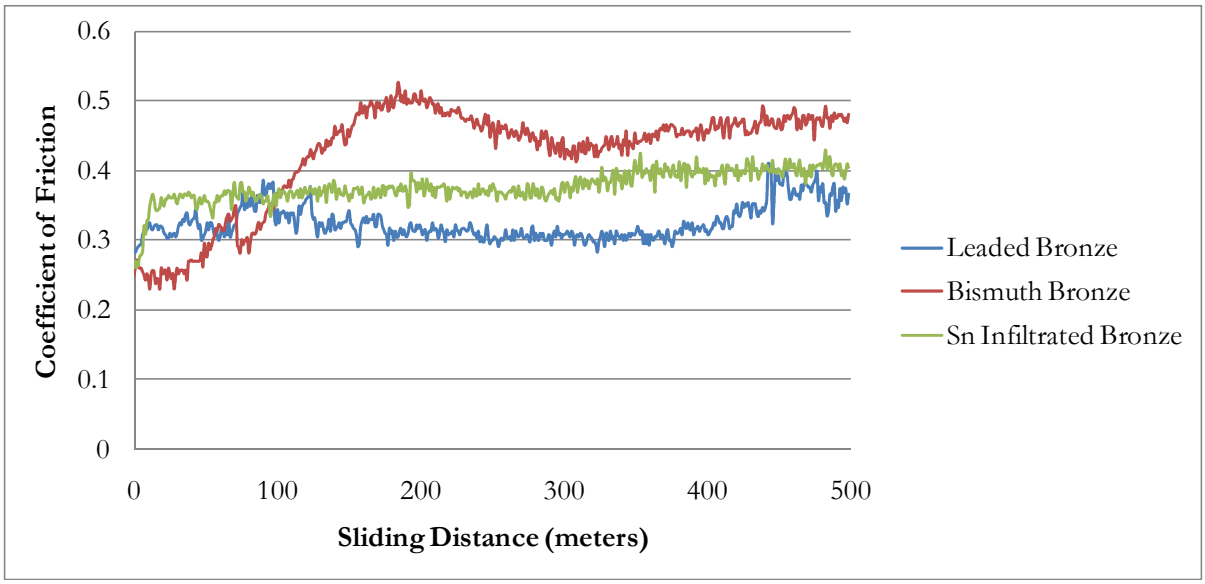


**Figure 95. Friction vs distance for each alloy against 52100 steel, 10cm/s, 10N.**

#### 5.3.4.1 Profilometry

Profilometry of the wear tracks shows that the tin bronze had the largest volume loss of the three materials, followed by the bismuth bronze and the best performer, the leaded bronze.

**Table 6. Heavily loaded dry sliding volume loss due to wear.**

| Disk Material | Volume loss vs. 52100 steel ($mm^3$) |
|---|---|
| Cu-10Sn-10Pb | 0.591 |
| Cu-10Sn-3Bi | 1.149 |
| Sn/Cu-10Sn | 4.130 |

#### 5.3.4.2 SEM

SEM examination of the surfaces from the first dry sliding wear test provided some explanation of the difference in volume loss between the three samples, particularly high volume loss for the tin infiltrated bronze. Under high magnification, the wear tracks have a similar appearance. The bronze matrix was significantly deformed in all three samples.

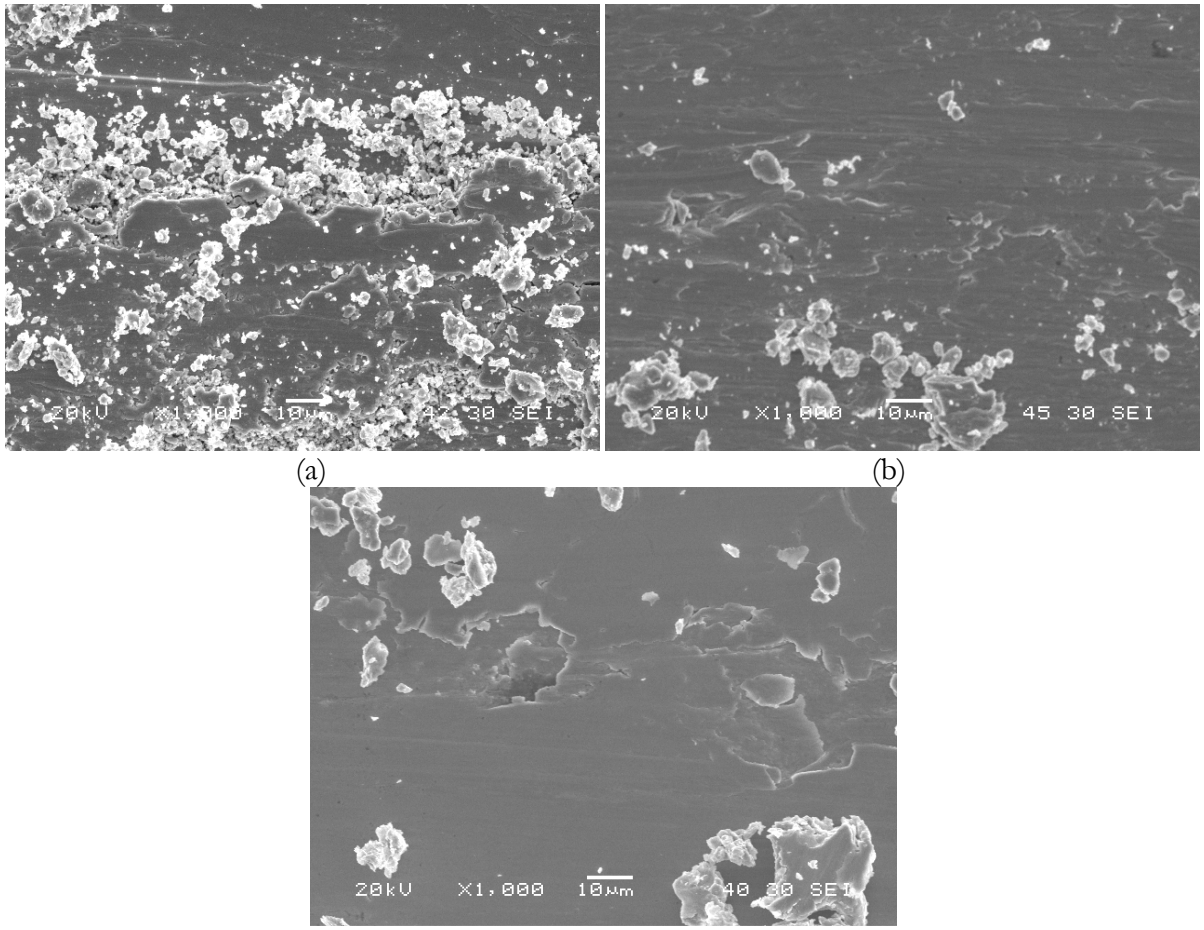


**Figure 96. a) Cu-10Sn-10Pb b) Cu-10Sn-3Bi and c) Sn/Cu-10Sn wear tracks.**

The 52100 bearing steel pins (Figure 97) from wear tests of each of the materials were similar in terms of amount of wear debris and material transfer (of bronze to the steel surface). The wear scars increase in size according to the calculated volume of material removed. This would be expected as the wear track conformed to the shape of the ball for each case.

The shape of the wear scar on each ball is the result of the contact with the opposing surface. The nearly circular scar of the bismuth bronze contacting pin is the result of sliding on a mostly flat surface, as shown on the right side of Figure 98. The elongated, elliptical wear scar on the pin that slid against the leaded bronze, and the even more elongated pin from the Sn/Cu-10Sn material are characteristic of two elastic bodies with one convex and one concave surface in contact. This would occur as the wear scar deepened into the originally flat surface, as shown in Figure 98.

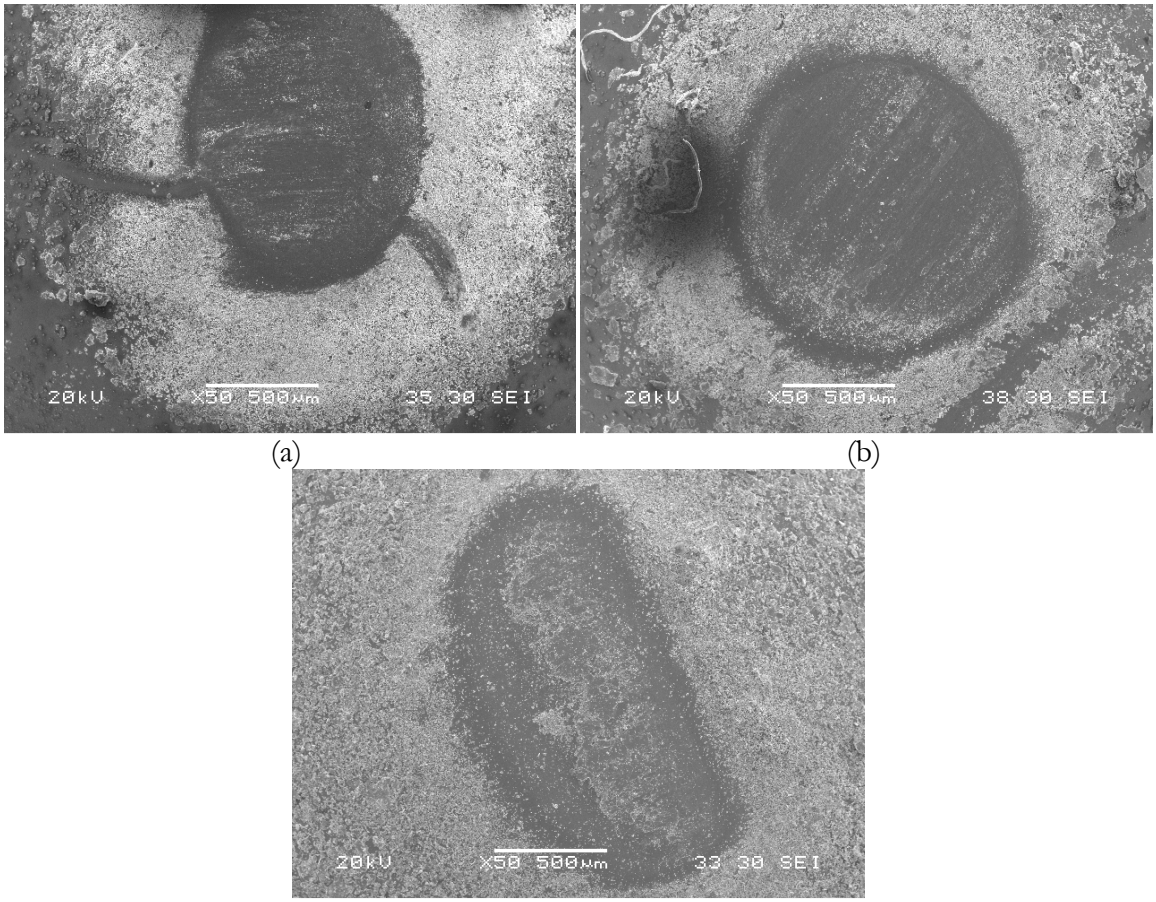


(a) (b)

(c)

**Figure 97. a) Cu-10Sn-10Pb b) Cu-10Sn-3Bi and c) Sn/Cu-10Sn ball surfaces.**

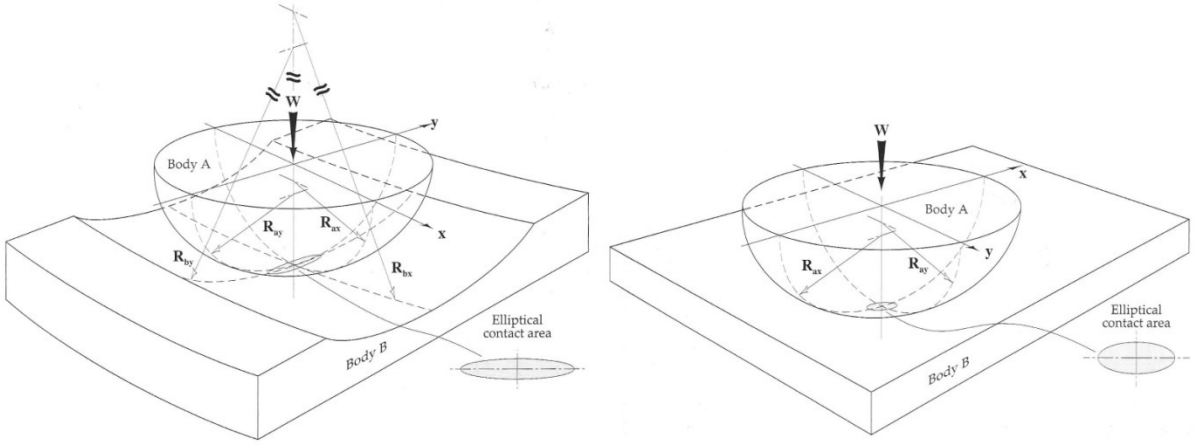


**Figure 98. Hertzian contact of a ball with a convex and flat surface (Stachowiak, 2005).**

The amount of eccentricity in the elliptical wear scar is related to the depth (concavity of the wear scar). The bismuth bronze shows the least deviation from the ball-on-flat arrangement because the wear track was shallow. Although the wear volume was greater than that of the leaded bronze, the radius was larger (26.47mm) than the leaded bronze (20.14mm). The Sn/Cu-10Sn material had the most material removed during the test, and had the smallest radius (9.48mm), thus creating the deepest wear scar and the most eccentric wear scar.

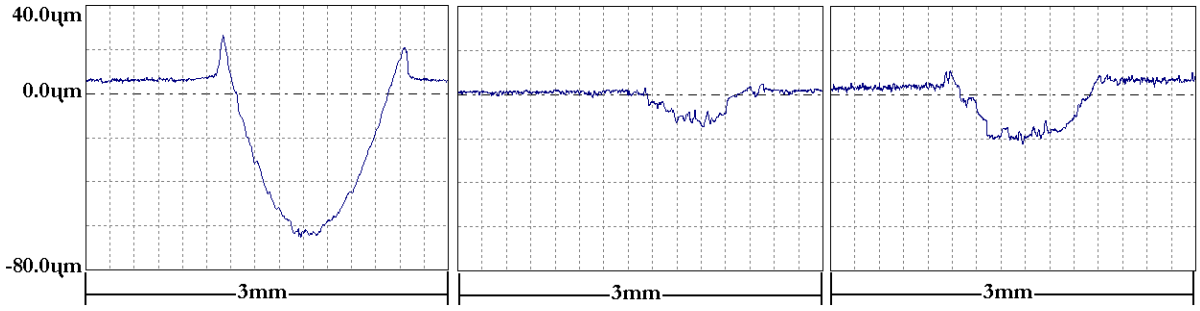


**Figure 99. Profiles of wear tracks in a)Sn/Cu-10Sn, b)Cu-10Sn-3Bi, & c)Cu-10Sn-10Pb.**

The most significant difference in the wear behavior of the three materials was the creation of wear debris. The three images of the wear debris along the wear tracks, shown in Figure 100, were all taken at the same magnification. There was a marked difference in the scale of the wear debris between the tin-infiltrated bronze samples and the existing valve plate materials. The scale of the debris on the leaded and bismuth bronze valve plates suggested localized yielding of the material due to asperities on the pin. In contrast, the scale of the wear debris on the Sn/Cu-10Sn disks was more reminiscent of bulk deformation and was on the size order of the bronze powder particles in the sintered material.

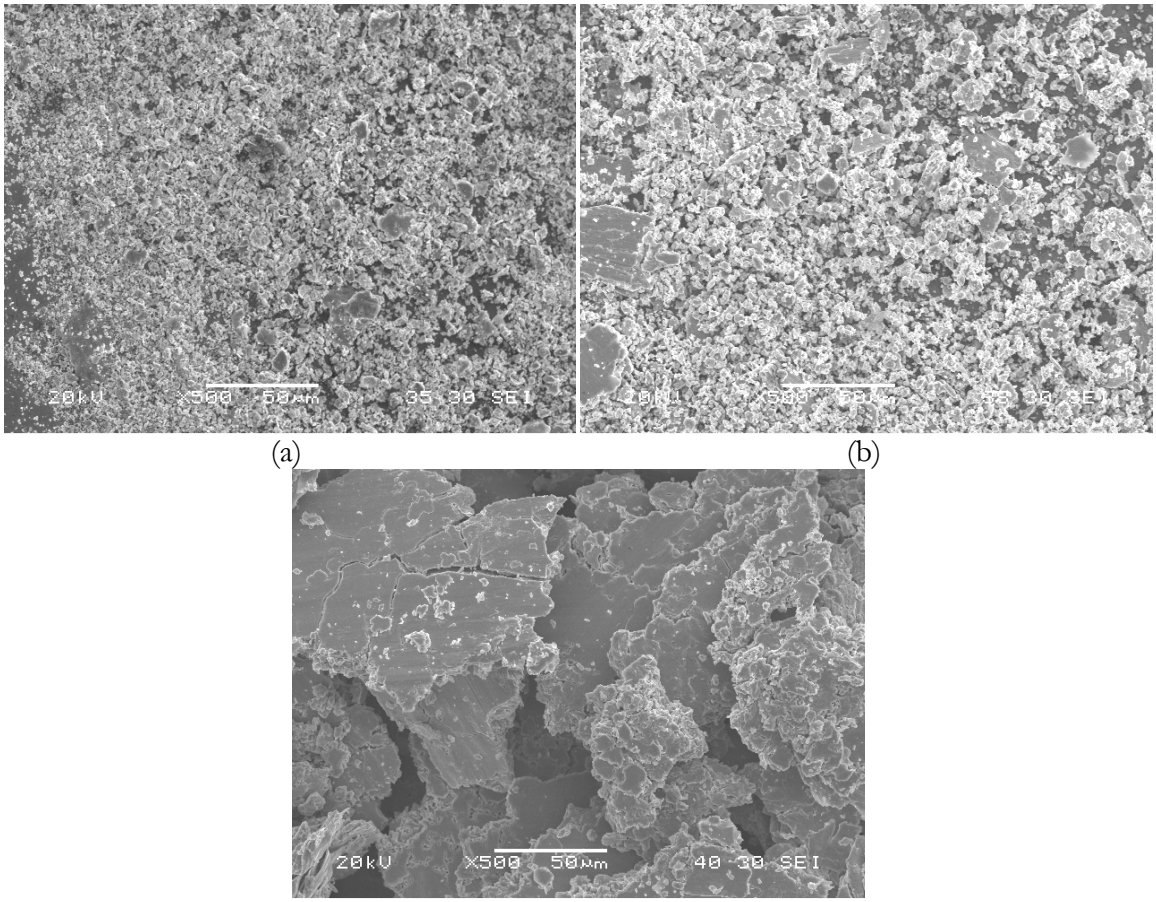


**Figure 100. a) Cu-10Sn-10Pb b) Cu-10Sn-3Bi and c) Sn/Cu-10Sn wear tracks.**

### 5.3.4.3 Discussion

Copper-based bearing materials are designed to take advantage of the strength of the bronze during high loading situations. Indeed, the wear characteristics displayed in each of the samples suggested that the bulk material (i.e. the matrix bronze strength) played the most important tribological role under high loading. Plastic deformation of the bronze matrix was the primary mode of wear and little influence of a soft phase was present on the surface.

It was previously determined that the yield strength of the as-infiltrated tin samples was 155MPa, due to the sintering parameters used to achieve maximum interconnected porosity. In contrast, P/M bismuth and P/M leaded bronzes were reported to have yield strengths of 280MPa and 230MPa, respectively.

The maximum hertzian contact stress on the surface of the bearing material was 402MPa and averaged 268MPa (assuming homogeneous materials and elastic deformation). The resultant shear stress in the disk material is 134MPa when the sample was at rest, and was located 0.022mm below the surface. As the coefficient of friction increases, the maximum shear stress increases and moves closer to the surface as shown in Figure 101 below.

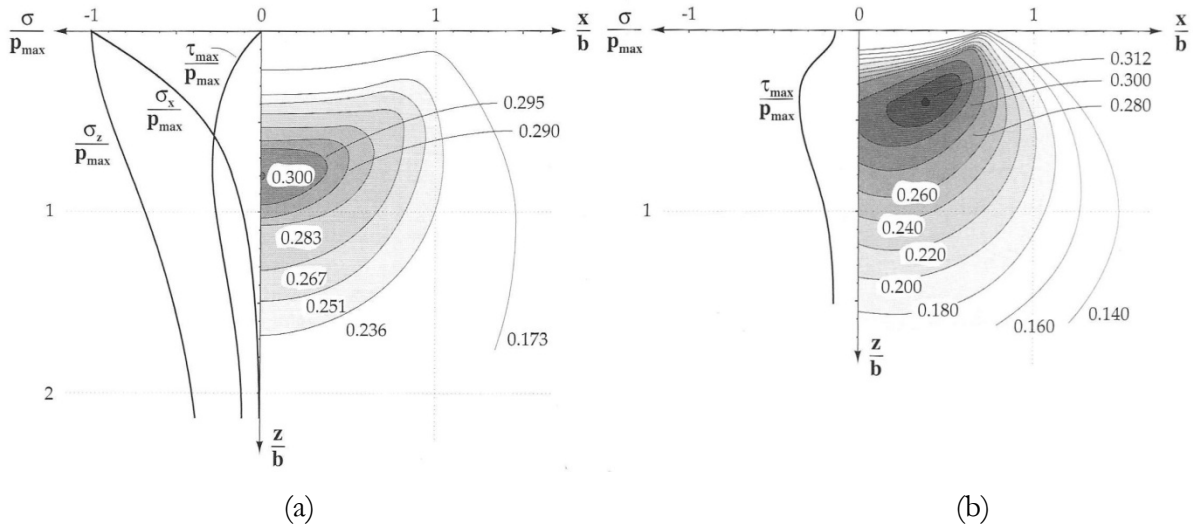


**Figure 101. Subsurface stress for a) static & b) sliding ball on flat contact (Stachowiak).**

The maximum shear stress in the material (134MPa) was very close to that of the yield strength of the Sn/Cu-10Sn bronze, especially in comparison to the 230MPa and 280MPa yield strengths of the Cu-10Sn-10Pb and Cu-10Sn-3Bi materials. This explains the bulk deformation and large wear debris present on the surface of the tin-infiltrated bronze bearing alloy. However, the alloy does show promise for being strengthened by increasing compaction and sintering parameters, thus eliminating the strength issue in wear tests.

### 5.3.5 High Speed Dry Wear Testing

The second set of wear tests was performed using the standard Falex tribometer pin on disk setup according to the procedure detailed in Section 5.1. The plot in Figure 102 shows the resulting friction as a function of time. All three materials started with nearly the same coefficient of friction (Pb,0.32; Bi,0.32; Sn,0.32) at the beginning of the test. The leaded and bismuth bronze both showed a decrease in the coefficient of friction during startup. Lead dropped to only 0.29, but the bismuth sample dropped to 0.15 before beginning to climb. Each

of the samples increased in coeffiecient of friction through the test at the same rate, although at different times. The Sn/Cu-10Sn sample reached its maximum early, then dropped slowly. The bismuth and leaded bronzes experienced the same increase in friction but later in the test, maxing out after 600m of sliding distance. It is possible that these samples, too, would have dropped had the test continued.

The bismuth bronze showed the lowest overall average friction (0.47 average) throughout the test and had a high average (from 700-1000m) of (0.66). The tin infiltrated bronze had a slightly higher coefficient of friction at 0.53, although it peaked early and thus has more values at the higher friction level. The average stabilized friction (300-1000m) was 0.57, lower than that of the bismuth bronze and leaded bronze. The leaded sample had an overall average coefficient of friction around 0.49 but rose to a fairly stable 0.63 after 600 meters of sliding.

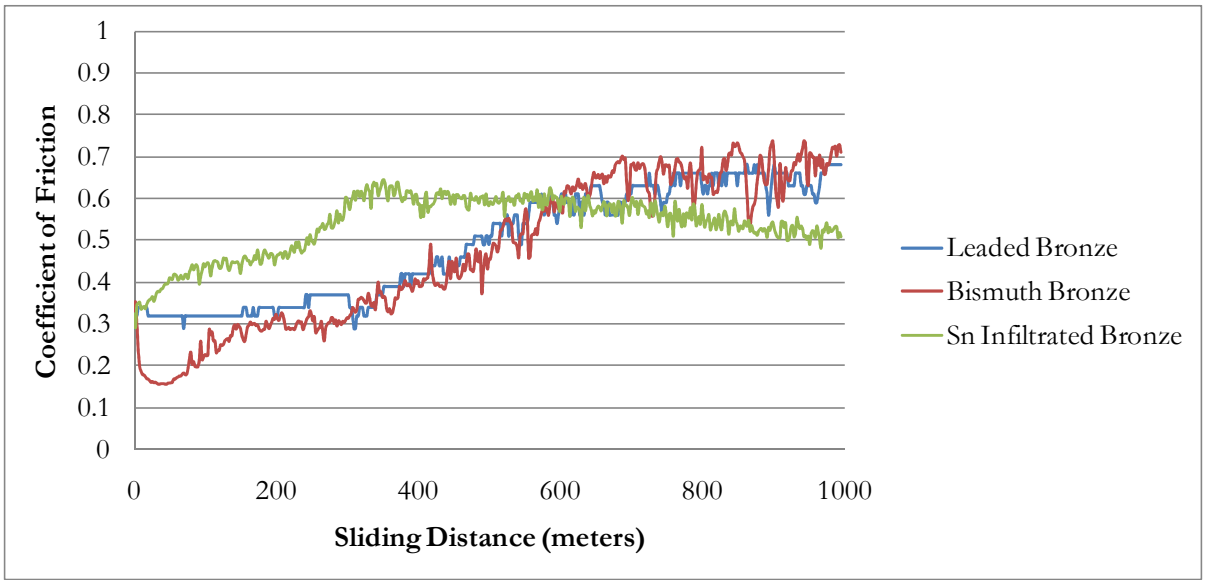


**Figure 102. Friction vs. distance for each alloy against P/M steel, 50cm/s, 1N.**

#### 5.3.5.1 Profilometry

Material removal from the disks in dry sliding with lighter loads against the copper-infiltrated P/M steel was more comparable than in the previous test. The Sn/Cu-10Sn bronze showed similar volume loss to the Cu-10Sn-3Bi material, but still slightly above leaded bronze.

**Table 7. High speed dry sliding volume loss due to wear.**

| Disk Material | Volume loss vs. P/M steel ($mm^3$) |
|---|---|
| Cu-10Sn-10Pb | 0.276262291 |
| Cu-10Sn-3Bi | 0.369509122 |
| Sn/Cu-10Sn | 0.393362434 |

### 5.3.5.2 SEM

The surfaces of the higher speed, lower load wear samples again showed very similar wear behavior. The wear was primarily abrasive wear along with plowing wear.

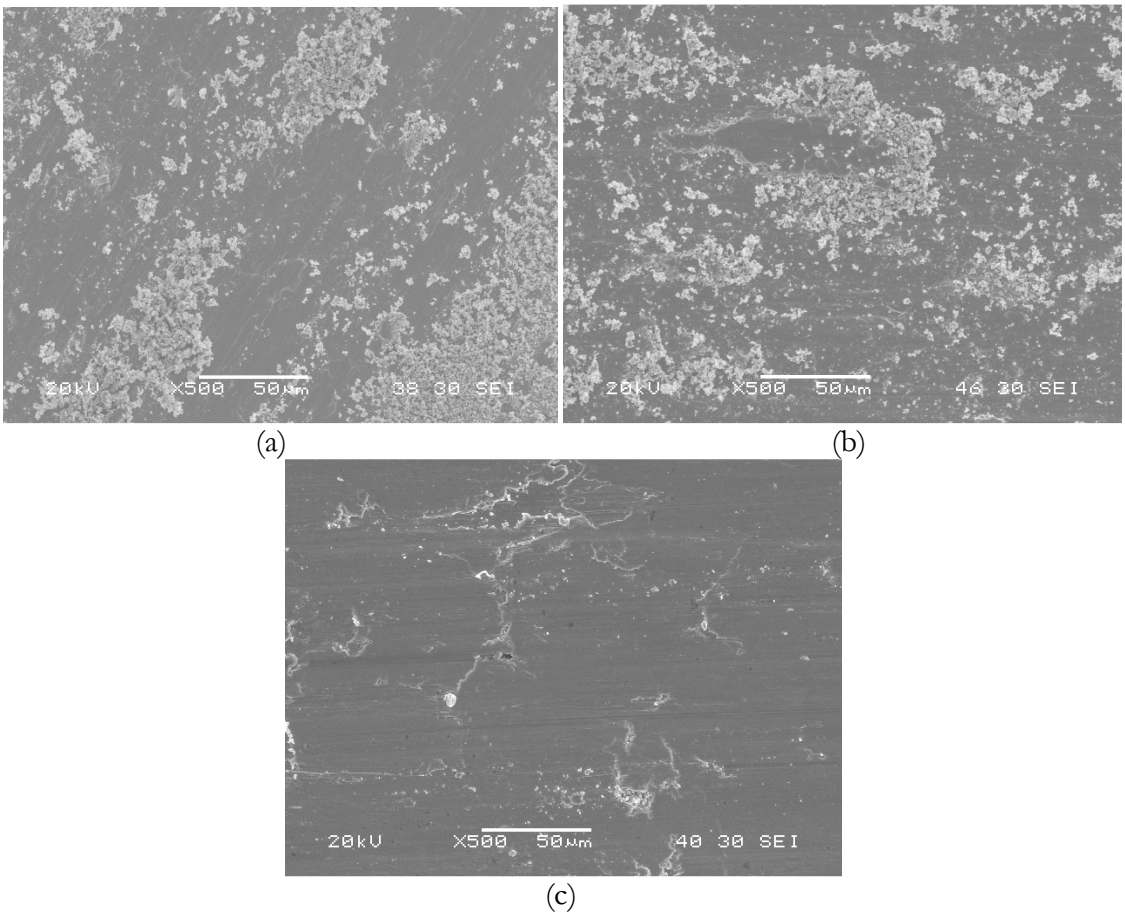


(a) (b)

(c)

**Figure 103. a) Cu-10Sn-10Pb b) Cu-10Sn-3Bi and c) Sn/Cu-10Sn wear tracks.**

The copper infiltrated P/M steel pins showed very little wear damage. The pin that was used to test the Cu-10Sn-10Pb sample (Figure 104a) had the most bronze material transferred to its surface. In contrast, there was very little of the Sn/Cu-10Sn material transferred to the surface of the pin (Figure 104c).

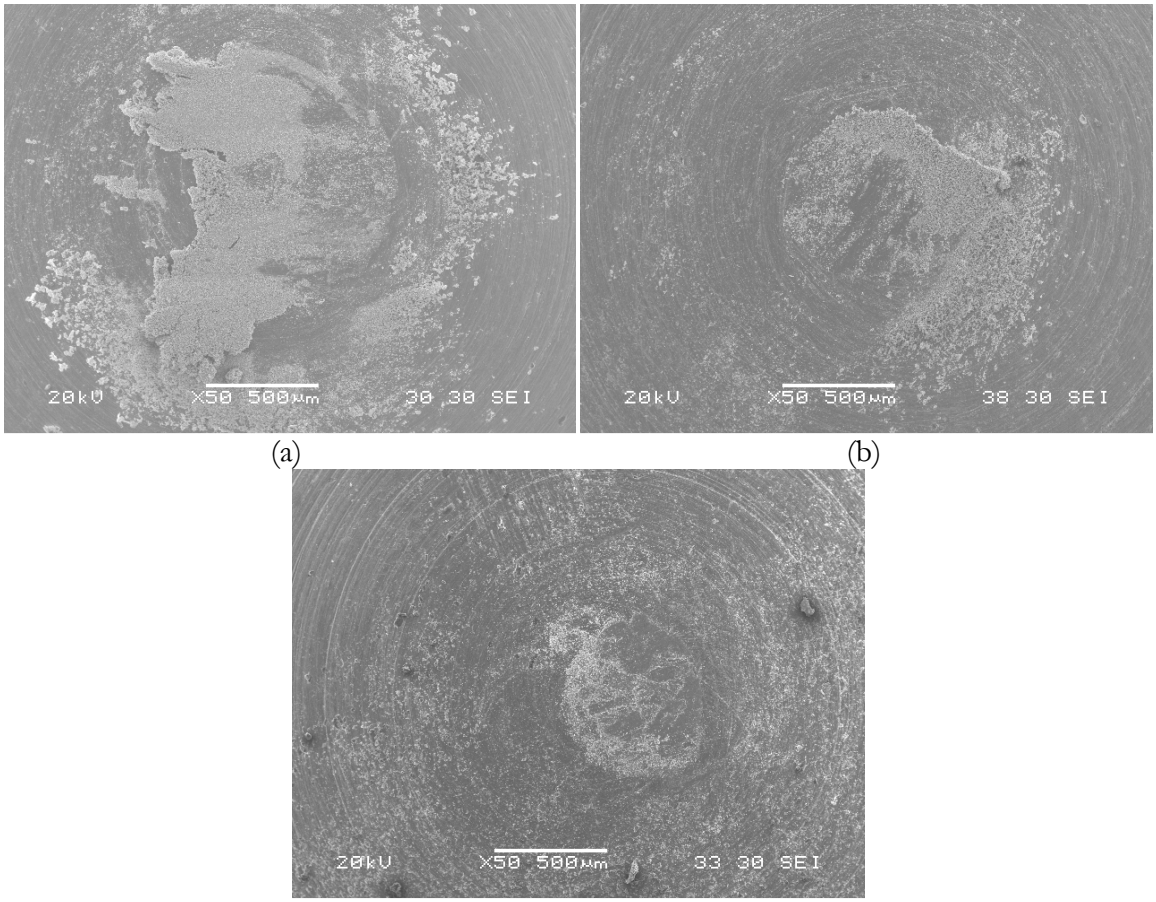


**Figure 104. a) Cu-10Sn-10Pb b) Cu-10Sn-3Bi and c) Sn/Cu-10Sn ball surfaces.**

Of particular note is the scale of the wear debris under lighter loading conditions. The wear debris for all the materials was comparable in size, as shown on the copper infiltrated P/M steel pin surfaces in Figure 105. In this wear test, the calculated maximum normal (Hertzian) stress is 187MPa, with an average being 124MPa. This results in a shear stress in the bronze material of 62MPa, which was far below the yield strength of any of the bronze materials.

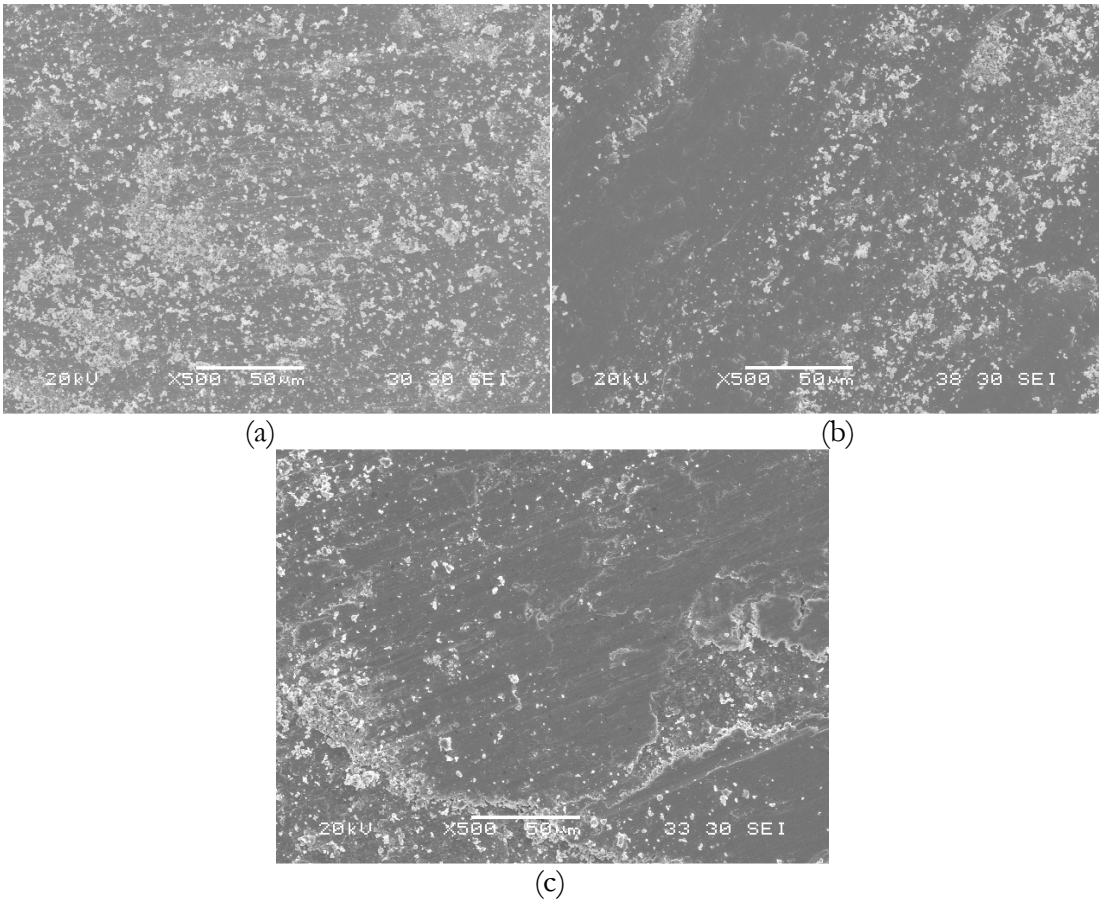


(a) (b)

(c)

**Figure 105. a) Cu-10Sn-10Pb b) Cu-10Sn-3Bi and c) Sn/Cu-10Sn ball surfaces.**

### 5.3.5.3 Discussion

The wear behavior of the tin-infiltrated bronze bearing material is similar to that of the existing bismuth and leaded bronze materials under moderate loads (187MPa) and speeds (50cm/s). The wear debris in this case was similar between all three samples. This agrees with the fact that the lighter load on the pin results in a shear stress far below the yield stress of each material. The coefficient of friction in all three materials was comparable between the three samples. The bismuth bronze showed the lowest overall average friction (0.47) and the leaded bronze was around 0.49. The tin infiltrated had a slightly higher coefficient of friction at 0.53, although it peaked early and thus has more values at the higher friction level. If only the stabilized friction levels are taken into account, the stabilized friction for the tin-infiltrated was 0.57, lower than that of the bismuth bronze (0.66) and leaded bronze(0.63).

## 5.4 Discussion

In order to be effective, the engineered microstructure of the tin infiltrated bronze must only contain a small amount of intermetallic phase along the edges of the pockets. The intermetallics possess properties that may be beneficial in small amounts, but mechanical issues brought on by thick layers of the brittle copper-tin intermetallics must be mitigated. The tin infiltrated bronze material must be able to operate in axial piston hydraulic pumps that see temperatures of up to 130˚C for extended times. These temperatures can promote the growth of $Cu_6Sn_5$ and $Cu_3Sn$ intermetallics. Manganese was added to the tin alloy to prevent the growth of the intermetallics, particularly of $Cu_3Sn$. It was shown through ageing tests that the addition of manganese did have an effect on the growth of $Cu_3Sn$, but no effect on the overall intermetallic layer thickness.

For the ease of initial production, samples produced throughout this study were made from bronze compacts pressed at 350MPa, then sintered at 650˚C for 2 hours. Keeping in mind that the 350MPa/650˚C/2hr compact production parameters were specifically chosen to maximize the ease of infiltration while sacrificing strength, the results from the TRS tests can be compared to the existing Cu-10Sn-Pb and experimental Cu-10Sn-3Bi strength data provided by Federal Mogul (Saxton, 2006). This comparison is shown in Figure 106.

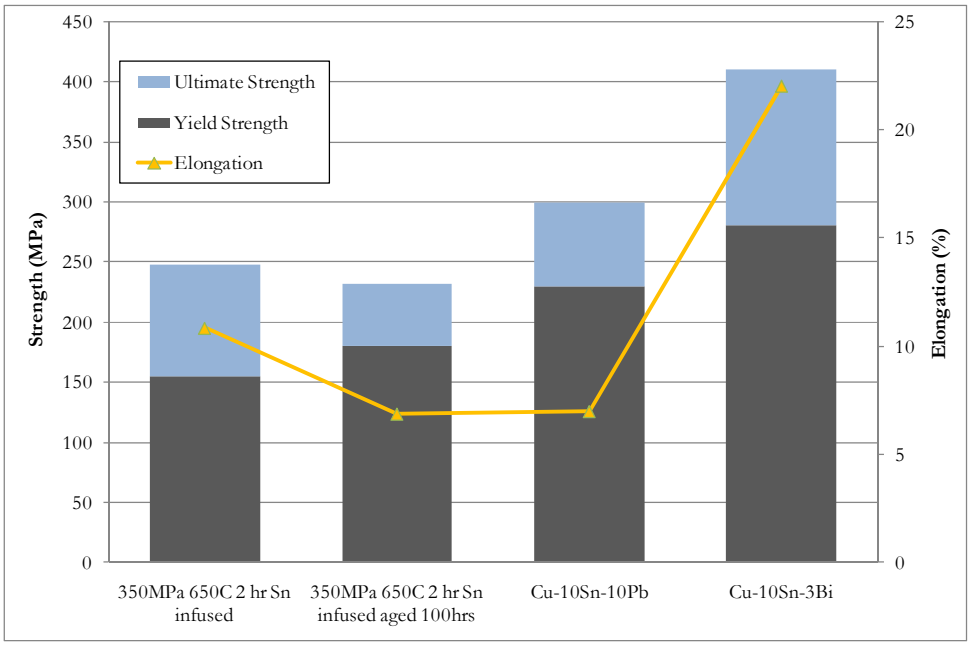


**Figure 106. Comparison of mechanical properties to previous alloys.**

The alloy developed for this study, the tin-infiltrated bronze, displayed mechanical properties that approached that of the leaded and bismuth bronze alloys previously developed. The results of tests relating compaction pressure and sintering (time and temperature) to strength show that increases in either parameter can and will increase the yield strength, ultimate strength, and elongation of the bronze compacts. In addition, samples have already been successfully infiltrated using a compaction pressure of 550MPa and sintered at 780˚C for 2 hours. Using these increased variables to create the sintered compact would result in mechanical properties on par with or exceeding those of the previous alloys.

The engineered tin infiltrated bronze bearing alloy performed well during the three sets of wear tests, as shown in Tables 8 and 9. Of particular interest are the lubricated conditions. The wear test was designed to best mimic the conditions in the axial piston hydraulic pump with current laboratory equipment. After the tests, the tin-infiltrated bronze material showed the same general wear mechanism as the leaded bronze and bismuth bronze for the lubricated tests. However, the Sn/Cu-10Sn alloy had the lowest volume loss of the bearing alloys. It also possessed the lowest coefficient of friction, although the figure was very similar to the leaded and bismuth bronzes.

**Table 8. Summarized coefficients of friction for the wear tests.**

| | Lubricated | | 10N 10cm/s 52100 dry | | 1N 50cm/s P/M steel dry | |
|---|---|---|---|---|---|---|
| Disk Material | average | stable | average | stable | average | stable |
| Cu-10Sn-10Pb | 0.18 | - | 0.32 | - | 0.49 | 0.63 |
| Cu-10Sn-3Bi | 0.19 | - | 0.42 | 0.46 | 0.47 | 0.66 |
| Sn/Cu1-0Sn | 0.17 | - | 0.38 | - | 0.54 | 0.57 |

**Table 9. Summarized volume loss for the wear tests.**

| Disk Material | Lubricated Disk | Lubricated Pin | 10N 10cm/s dry | 1N 50cm/s dry |
|---|---|---|---|---|
| Cu-10Sn-10Pb | 0.612 ($mm^3$) | 0.201 | 0.591 | 0.276 |
| Cu-10Sn-3Bi | 0.446 | 0.063 | 1.149 | 0.370 |
| Sn/Cu-10Sn | 0.353 | 0.104 | 4.130 | 0.393 |

The most substantial issue arose during the highly loaded wear tests. One of the primary purposes for using multicomponent bearing alloys is the strength of the bronze matrix, particularly during high loading situations. Indeed, the results of the highly loaded wear test

showed that the strength of the tin-infiltrated samples produced with maximum porosity (350MPa/650°C/2hr) did not possess sufficient strength. They exhibited bulk deformation and large wear debris present on the surface of the tin-infiltrated bronze bearing alloy. However, the strength tests show that the alloy can be strengthened by increasing compaction and sintering parameters, thus potentially eliminating the strength issue in wear tests.

# CHAPTER 6. CONCLUSIONS

- An initial comparison of the production powder metal valve plates made with Cu-10Sn-10Pb surface layers, and experimental valve plates made with Cu-10Sn-3Bi (wt.%) surface layers showed that the unacceptable wear behavior between the Cu-10Sn-10Pb and Cu-10Sn-3Bi alloys arose due to the use of bismuth as the soft phase in the alloy. Bismuth was implicated as the cause of both solid and liquid metal embrittlement of the bismuth bronze alloy.
- A novel lead free alternative was developed that utilizes free pockets of tin or tin alloy in a bronze matrix, building from the idea that lead and tin have long been used interchangeably as soft bearings. However, the solubility of tin in bronze required that the sample be created by liquid infiltration of a presintered porous bronze compact.
- Infiltration was shown to be an effective method of producing a the desired multicomponent microstructure with strong and soft phases given proper processing parameters.
- Solidification of the soft tin alloy created copper-tin intermetallics where it contacted the bronze in the infiltrated microstructure. In small volume fractions, these intermetallics have been shown to be beneficial for several properties. However, having a highly networked boundary of a hard, brittle intermetallic phase could prove to be a detriment to impact strength, toughness, and wear properties.
- The extent of the intermetallic compound layer formation, particularly $Cu_3Sn$, at the interface with the bronze matrix should be controlled to retain as much of the soft phase as possible. Initial control was achieved by minimizing the amount of heat exposure (temperature and time) required for infiltration of the porous Cu-10Sn bronze.
- Mitigation of the influence of intermetallic growth after thermal aging, particularly of $Cu_3Sn$, was also attempted by a minor alloy addition (manganese) to the tin.. From tests that were performed at temperatures (130˚C) likely to be experienced during operation of the valve plate, the addition of manganese did slow the growth of $Cu_3Sn$ compared to unalloyed tin, but had no effect on the overall intermetallic layer thickness.
- To promote the success of the melt infiltration processing approach, samples produced throughout this study were made from bronze compacts pressed at 350MPa, then

sintered at 650˚C for 2 hours. These compact production parameters were at the minimum green strength limits for handling and were designed to produce only modest sintered strength from the early stages of sintered neck growth. Even so, the porous bronze structures developed for this study displayed mechanical properties that approach that of the leaded bronze and bismuth bronze alloys previously developed.

- Increases compaction pressure and sintering (time and temperature) increased the yield strength, ultimate strength, and elongation of the bronze compacts to well beyond the previous alloys (as measured by TRS). This ability to control the strength and interconnected porosity of the bronze matrix should make it simple to create a material with in mechanical properties on par with or exceeding those of the previous alloys while retaining wear properties of the standard leaded bronze.
- Since mechanical strength is particularly important for highly loaded sliding conditions. Wear tests showed that tin-infiltrated samples produced with maximum porosity (350MPa/650˚C/2hr) did not possess sufficient strength for highly loaded applications. Being able to increase the strength by design of the bronze matrix presintered compact can eliminate this problem.
- In wear tests designed to simulate conditions in axial piston hydraulic pumps, the engineered tin infiltrated bronze bearing material showed the same general wear mechanism as the leaded bronze and bismuth bronze. However, the Sn/Cu-10Sn alloy had the lowest volume loss of the three bearing alloys, even in 350MPa/650˚C/2hr samples. It also possessed the lowest coefficient of friction, although the figure was very similar to the leaded and bismuth bronzes.

# CHAPTER 7. FUTURE WORK

The basis for a new lead-free bearing alloy was successfully developed and characterized. However, there is a considerable amount of opportunity to fine-tune the engineered structure of the composite material and the processing techniques used to produce it. Simple variations in processing parameters of both the bronze compacts and the infiltration of tin-based alloys have the capacity to change the composite microstructure for various applications. Optimization of the techniques used to manufacture the new, lead-free bronze alloy will make the bearing simple to produce in the future.

## 7.1 Alloy Development

### 7.1.1 Bronze Matrix Strength

The samples prepared for this study were created using compaction and sintering parameters (350MPa/650°C/2hr) for the Cu-10Sn powder that promoted the maximum ability to be infiltrated with the tin based alloys. Producing partially sintered bronze with these parameters created a bronze matrix with 20 vol.% interconnected porosity. However, these low density samples were not meant to have the strength ultimately required in bearing bronzes for axial piston hydraulic pumps.

It was shown in the strength study (Section 5.3.2) that the mechanical properties could be improved by increasing the compaction pressure and/or sintering temperature. The fracture surfaces from the strength study showed that interconnected porosity was present in samples in which either the compaction pressure (700MPa/650°C /2hr) or sintering temperature (350MPa/780°C/2hr) were increased over the base 350MPa/650°C samples.

Therefore, the compaction and sintering parameters can be manipulated to create a balance between the amount of interconnected porosity and the mechanical properties. The ability to manipulate these characteristics allows the composite microstructure to be tailored for the specific application. Future work, then, should focus on balancing these properties for the most effective bearing alloy.

Evidence for the potential for improvement provided by powder metallurgy is provided by samples produced in the initial round of infiltration. It was shown that bronze compacted at 550MPa and sintered for 2 hours at 780˚C could be infiltrated, despite their lower porosity. Even without the use of flux, the tin alloys had the ability to infiltrate to a significant depth (Figure 107).

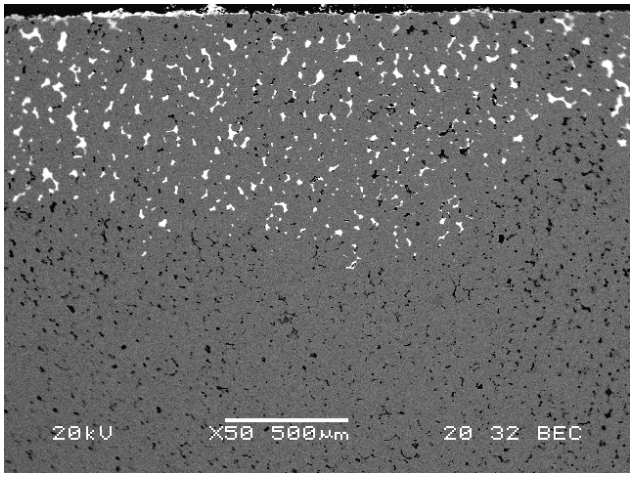


**Figure 107. Backscattered image of Sn-1.37Mn (shown as white) partial infiltration.**

The fracture surface of a similarly compacted and sintered sample (Figure 110) shows partially interconnected porosity that results in the infiltrated structure above. Although promising, Figure 107 and 108 show that some closed or partially closed porosity was present that was not infiltrated properly. If the porosity is interconnected, but the openings are too small for infiltration, the resultant structure may still be porous to oil. This could create problems in axial piston hydraulic pump valve plates where the valve plate must provide a sealing surface for the cylinder block. On the other hand, fully closed or blocked porosity on the wear contact surface can retain oil, aiding in lubrication between the contacting surfaces of the cylinder block and valve plate. Further investigation is required to determine what type of porosity is present in this type of microstructure and its effect on the materials performance as a valve plate surface layer.

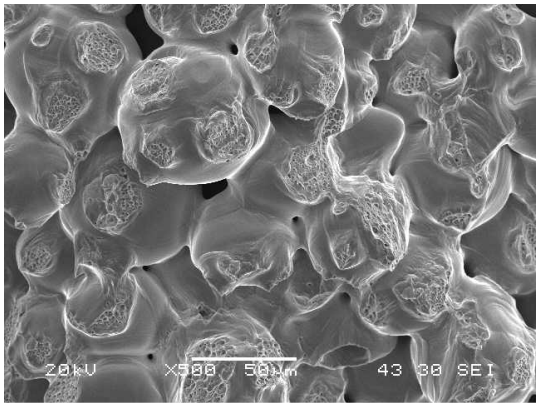


**Figure 108. Cu-10Sn bronze compacted at 500MPa and sintered at 780˚C for 2 hours.**

It was shown that by lowering the sintering temperature by 80˚C, the interconnected porosity was greatly increased in the bronze (Figure 109). In addition, the yield strength of the 500MPa 700˚C 2 hour bronze matrix was 235MPa, a number very comparable to the 230MPa and 280MPa yield strengths of the Cu-10Sn-10Pb and Cu-10Sn-3Bi materials. Future work should look at the effectiveness of infiltration in samples produced with compaction and sintering parameters like this that achieve sufficient strength while retaining interconnected porosity.

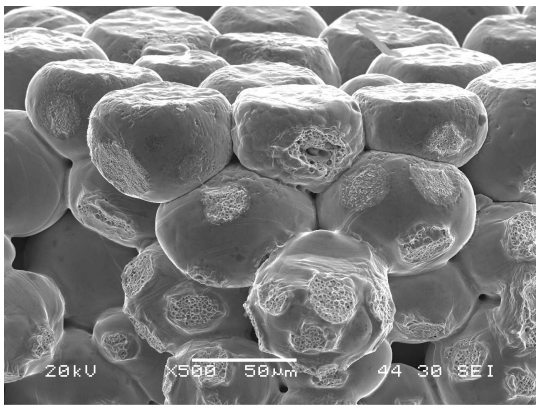


**Figure 109. Cu-10Sn bronze compacted at 500MPa and sintered at 700˚C for 2 hours.**

### 7.1.2 Infiltration

#### 7.1.2.1 Tin Manganese Infiltration

While infiltration was shown to be largely successful, particularly in samples pressed at 350MPa and sintered at 650˚C for 2 hours, there are ways that the infiltration can be improved with future study. Without flux, it was noted that the tin-manganese (Sn-1.37Mn wt. %) alloy powder did not coalesce well, as shown in Figure 110.

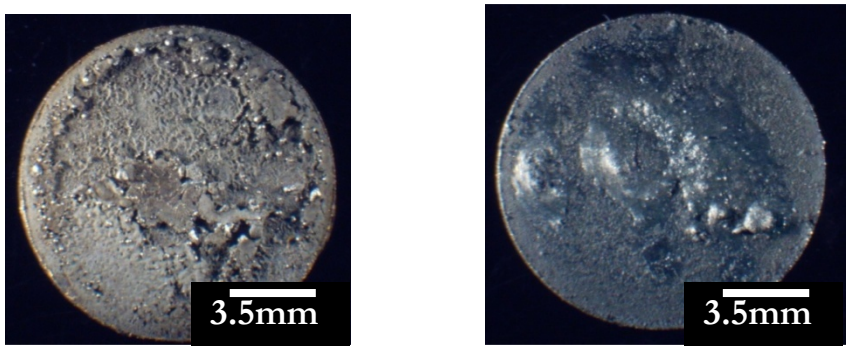


(a) (b)

**Figure 110. a) Sn-1.37Mn and b) Sn powders after equivalent heat treatment.**

Using Johnsons E127 flux, both the pure tin and tin-manganese (Sn-1.37Mn wt. %) alloys were shown to infiltrate the bronze to equal depths; however, the tin manganese samples repeatedly retained a portion of the alloy on the surface. Although only a small fraction of the metal remained on the surface, the appearance was that of a larger mass of material, as shown on the left two samples in Figure 111.


**Figure 111. Macroscopic view of a) Sn-1.37Mn and b) Sn infiltration samples.**

The volume of the "bump" on the surface is mainly due a highly porous structure that is created by gases trapped during reflow for infiltration. Figure 112 shows one of these bumps removed from the surface of the sintered bronze and viewed from below.

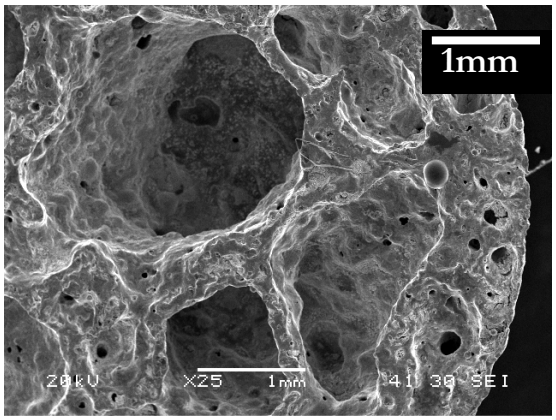


**Figure 112. Residual Sn-1.37Mn from the underside of the bump.**

Further work is required to determine the exact mechanism behind the phenomenon. There are a couple of possible explanations which could account for the behavior of the manganese samples. The first of these is the reaction of manganese during powder production with the atmosphere, or during infiltration with either the flux or atmosphere. The oxidation reaction of the powder during reflow for infiltration could also be influenced by the fine powder size with an increased surface area. Any combination of these reactions could result in the behavior exhibited above and should be explored in more detail.

The original target alloy was 5 wt.% Mn for the tin alloy that was used for infiltration. To produce the tin alloy powder, Mn was added in the form of 1mm electrolytic flakes to pure Sn and inductively melted in a graphite crucible in the gas atomizer under hydrogen (Strauss, 2009). Surprisingly, the Mn would not go into solution after 30 minutes at 1250˚C. According to the equilibrium phase diagram (Okamoto, 1999), the two metals should both liquid and/or in solution at that temperature. The formation of MnH was ruled out since extremely high pressures are required for its formation and the MnH would be unstable at the temperatures in the crucible (Strauss, 2009). A second attempt was made to produce the Sn-Mn alloy with a target of 2 wt.% Mn and the remainder Sn. The alloy was mostly solutionized at 1400˚C under Argon, but some remnants of unmixed material were present on the surface of the melt. The resulting powder composition was Sn-1.37Mn (wt. %) that was used for the bulk of the study.

The cause of the melting and solutionizing issues was not examined in this work, but may be the cause of the infiltration behavior shown in Figure 110 and Figure 111. Further study exploring the reactivity of tin-manganese should be pursued to eliminate this source of trouble if manganese is used as an alloying addition. Other alloying additions to tin, e.g. zinc, have also been shown to limit $Cu_3Sn$ intermetallic growth during thermal aging of solder joints on copper substrates. These alternative additions to tin should also be studied since they may avoid the obvious challenges of the manganese addition and should have the same benefit.

The issue of powder coalescence during reflow suggests that the tin-manganese powders are surface active and react with the atmosphere to form a shell that is retained on the molten tin-manganese powder particles, preventing them from coalescing. Using an acid-containing flux removes the outer reacted layer, allowing the particles to coalesce. Infiltration using pure tin without a flux was also shown to be more effective, which could mean that the manganese is the reactive species. Moreover, the -25µm pure tin powder (figure 113b) is not only larger than the Sn-1.37Mn powder (Figure 113a) that has a size distribution of d10 of 3.23µm, d50 of 7.81µm, and d90 of 15.48µm, but has far fewer particles of very small size. These small particles greatly increase the surface area of the tin-manganese powder, maximizing any surface reactions present.

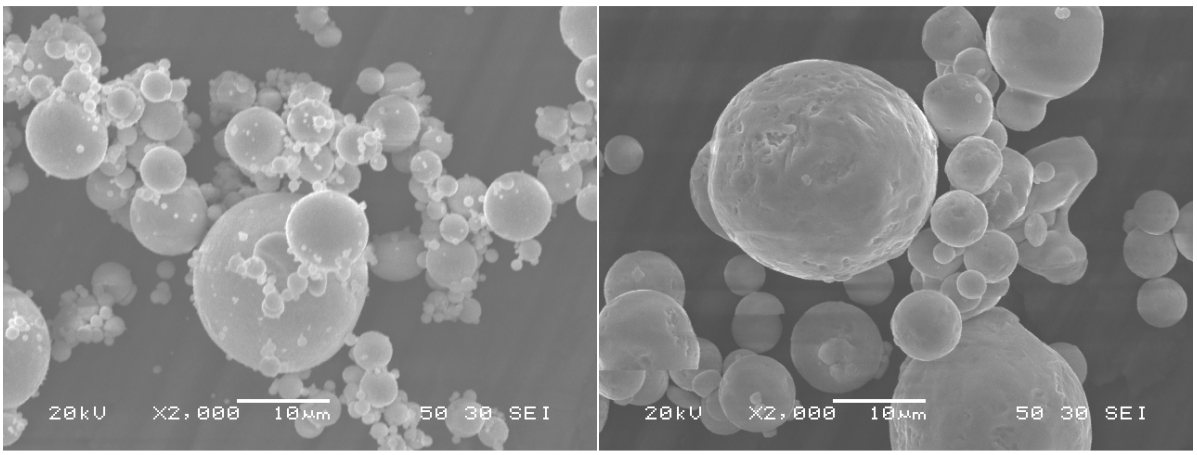


(a) (b)

**Figure 113. Gas atomized a)Sn and b) Sn-1.37Mn powder.**

Future work should look at the effect of powder size distribution and atmosphere on the coalescence of the powder for infiltration. Increasing the powder particle size may decrease the effect of the surface reactions, and allow the flux to remove the surface layer of the powder

particles during reflow. It may also be useful to decrease the percentage of powder in the flux paste from the 75 wt. % solids recommended by the manufacturer. This would make more acid available to clean the powder surfaces prior to reflow.

#### 7.1.2.2 Flux

The flux used in this study was chosen based on commercial availability. However, a flux more suited to the application could be developed. Johnson Manufacturing Companies E127 flux uses a relatively low viscosity, glycerin-based carrier that boils off during the heating stage of infiltration. The image in Figure 114 shows a sequence in time beginning with the flux applied to the surface of the sample. The second image shows the volume change associated with the boiling off of the solvent in the flux. This boiling action is likely responsible for the porous nature of the metal remaining on the surface and is undesirable for infiltration where the infiltrant alloy must be in contact with the bronze surface. The choice of another flux or an additional drying step for the paste could eliminate this issue.


**Figure 114. Time lapse images of Sn-1.37Mn infiltration in a bronze compact.**

In addition to the boiling effect, the E127 flux produces a sticky, water soluble residue from the glycerin as the tin alloy melts. This residue appears to primarily remain on the surface of the tin alloy; however, some may penetrate the porous bronze compact during infiltration. The effect of this on the production of steel backed bearings should be investigated and the glycerin may need to be eliminated from any future flux.

#### 7.1.2.3 Complete Infiltration

The samples produced in this study were all prepared using sintered bronze that was 3-7mm in thickness. Each sample was only provided a limited amount of fluxed tin-alloy paste for infiltration as shown in Figure 116. Since the bronze samples were effectively open to all sides,

there was nothing to prevent the spread of the tin alloy in the bronze compact, occasionally resulting in partially filled pores as seen in the fracture surface in Figure 115.

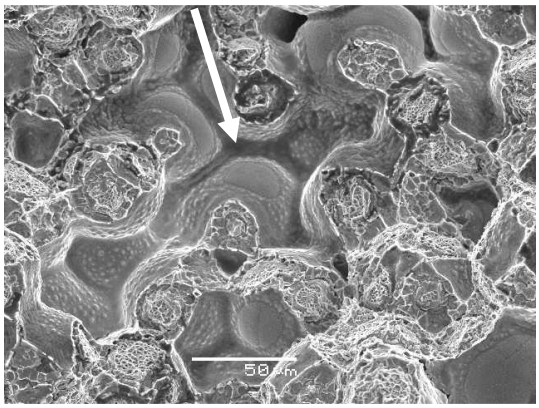


**Figure 115. Partially filled pores in a fracture surface of tin infiltrated bronze.**

The open pores in the fracture surface (example highlighted with a white arrow) are detrimental to the wear behavior of the bearing if left interconnected. However, valve plate surface layers are only on the order of 500µm thick after lapping, and are backed with a steel plate. The steel plate may cause liquid tin to pool in the pores, effectively filling them all, or it may cause gases to be trapped in the pores by the infiltrating tin alloy. Future work should look at infiltrating steel backed samples to determine the effect of the steel in terms of infiltration and microstructure.

### 7.1.3 Intermetallic Growth

It was shown throughout the present work that initial intermetallic growth could be controlled by limiting the time the infiltrated bronze compact remained above room temperature. By increasing the heating rate for infiltration, lowering the superheat, and quenching the sample, only minimal $Cu_6Sn_5$ was formed along the interface between the bronze and tin alloy.

To create an effective bearing alloy for axial piston hydraulic pumps, the influence of the intermetallics on alloy strength and wear resistance properties must be minimized. This is particularly important when the valve plates operate in ambient temperatures of 130°C for hours on end. Temperatures this high promote the growth of copper-tin intermetallic layers that reduce the amount of free tin alloy in the pockets, influencing the wear behavior of the alloy.

The growth of the intermetallics also causes a decrease in the mechanical properties of the alloy as the bronze is replaced by brittle intermetallics; the effect of this replacement of the strong bronze by brittle intermetallics is particularly problematic at the narrow necks of sintered bronze particles.

It was shown that small additions (1.37 wt. %) of manganese were able to stifle the growth of $Cu_3Sn$ at the tin/bronze interface, but did not influence the overall intermetallic thickness. Other alloying additions should be explored in future work to negate the growth of both $Cu_6Sn_5$ and $Cu_3Sn$ copper-tin intermetallics in the infiltrated bronze bearing, as mentioned above.

Aside from alloying additions, other steps can be taken to reduce the effect of the intermetallic growth. A simple way to reduce the influence of the copper-tin intermetallics is to eliminate as much of the tin/bronze interface as possible. Creating pockets of tin with high volume to surface area ratios would reduce the amount of copper-tin intermetallics formed. Larger pores in the bronze compacts can be achieved using increased particle size. To ensure the packing density stays low, a uniform powder size should be used.

An example of a possible modified microstructure is shown schematically in Figure 116. Sintered bronze particles are represented in orange, the infiltrant tin alloy in gray, and $Cu_6Sn_5$ in white. The samples shown in Figure 116 each contain approximately the same volume fraction of soft phase (shown in gray). The material created with finer prior particles contains 21 vol. % soft phase, and the courser example contains 17 vol. %.

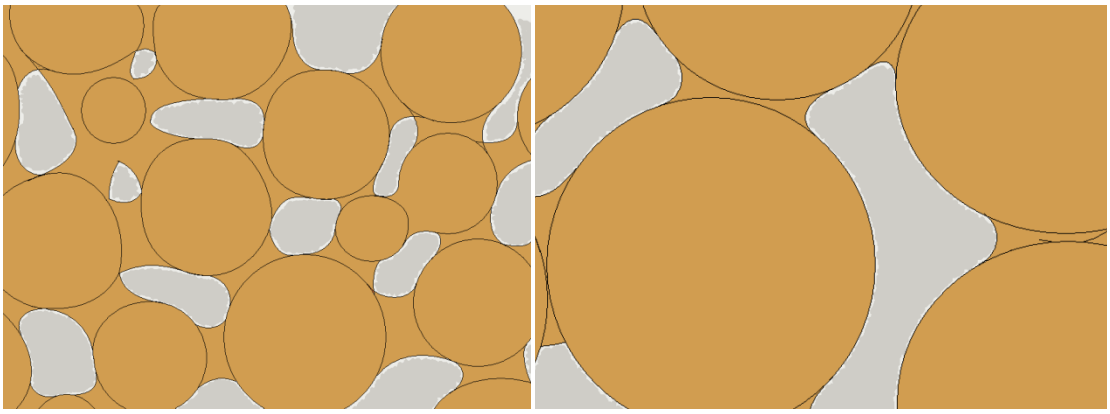

**Figure 116. a) Sn-1.37Mn and b) Sn powders after equivalent heat treatment.**

If each sample is aged at the same temperature for the same amount of time, as represented in Figure 117, the finer microstructure retains 17 vol. % of the original free tin. The microstructure with larger pores, on the other hand, still has 29 vol. % of the original tin available to act as a solid lubricant.

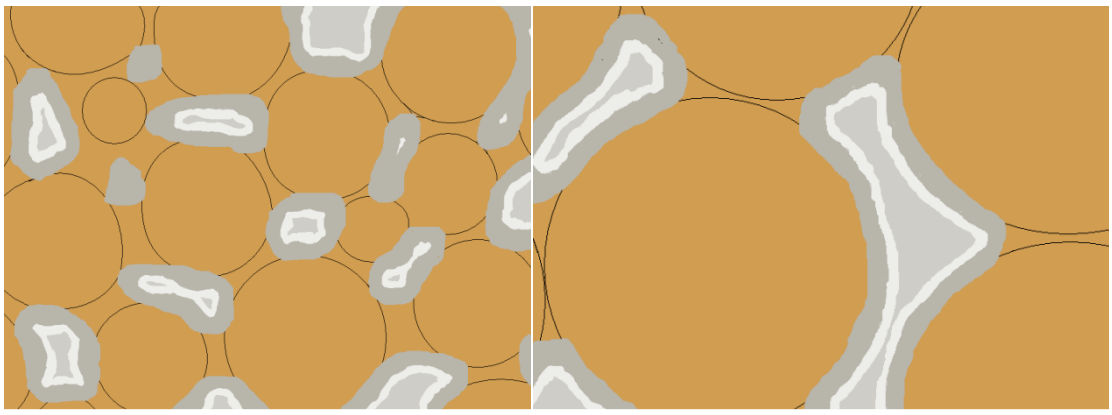

**Figure 117. a) Sn-1.37Mn and b) Sn powders after equivalent heat treatment.**

In addition to creating an advantage by manipulating the surface area to volume ratio of the infiltrated pores, increased bronze particle size with a uniform size distribution allows the bronze to be sintered at higher temperatures to greatly increase the neck diameter without sacrificing porosity. This will reduce the risk of embrittlement as the copper at the necks is used up by the intermetallics. Smaller necks risk being "bridged" by copper-tin intermetallics, creating a fracture path for brittle failure through the bulk material.

Future work should strive to optimize alloying additions and microstructure to both reduce the growth of copper-tin intermetallics during operation and minimize the impact of the remaining increase in intermetallic thickness. Doing so will ensure that the bearing alloy is as effective after hundreds or thousands of hours as it was when it was new.

## 7.2 Wear Testing/Material Validation

As any of the refinements from Section 7.1 are made to the alloy, the samples should be tested for mechanical properties and wear resistance in the same manner as the base alloy in Chapter 5. As strength is improved, the samples may be tested using tensile testing rather than the TRS tests intended for more brittle materials. Tests to determine the effect of high

temperature aging can be extended to reflect the service times expected of axial piston hydraulic pumps (~10,000hrs) as alloying additions and microstructural improvements are made to the composite bearing material.

Wear testing of the engineered Sn+X/Cu-10Sn composite materials is critical to determining their future as a lead free bearing alloy. The current alloys, Sn/1.37Mn and Sn-1.37Mn/Cu-10Sn, were wear tested using available equipment in the as-infiltrated condition. Multiple repetitions of these wear tests should be performed, including aged samples of the material for comparison. Any additional modifications to the microstructure in terms of strength, alloying additions, or fraction of solid phase should be performed using comparable wear tests.

Future laboratory wear testing should also including higher sliding velocities than the 50cm/s the current Falex ISC250PC tribometer is capable of producing on the current 40mm diameter test samples. Axial piston hydraulic pumps operate at up to 5000RPM, creating sliding speeds approaching 30m/s. Replicating this speed will be important in qualifying the final material.

## 7.3 Prototype Valve Plates

Although the composite bearing alloy developed in this study is applicable to a wide variety of applications for which wear resistance is required, the ultimate goal was to develop a material that created a satisfactory replacement material for the leaded bronze surface layer on axial piston hydraulic pump valve plates. The ultimate test then, is to produce prototype valve plates using the new tin alloy infiltrated bronze as surface layers. These valve plates would be produced as dictated by the future study described in Section 7.1, then installed in axial piston pumps running a similar test routine to that shown in Table 1 (Section 3.2.1). The results of tests such as this will be the determining factor for the ultimate success of the tin infiltrated bronze bearing alloy in axial piston hydraulic pumps.

# BIBLIOGRAPHY


1. Aglan, Heshmat. (2006). Fracture and Fatigue Damage Tolerance of Bainitic and Pearlitic Rail Steels. U.S. Department of Transportation Federal Railroad Administration.
2. Akers, Arthur, Max Gassman, and Richard Smith. (2006). Hydraulic Power System Analysis. New York: CRC Press.
3. American Society for Testing and Materials. (1969). Evaluation of Wear Testing. Philadelphia: American Society for Testing and Materials.
4. Bannister, Kenneth E. (1996). Lubrication for Industry. New York: Industrial Press, Inc.
5. Betz, Mike (2008). Sauer Danfoss Corporation. Ames, Iowa. private communication.
6. Bhushan, Bharat (2001). Modern tribology handbook, Volume 1. Mechanics and materials science series. Florida: CRC Press. pp 773.
7. Chang, L.S., E. Rabkin, B.B. Straumal, B. Baretzky, and W. Gust. (1999). Thermodynamic Aspects of the grain boundary segregation in Cu(Bi) alloys. ActaMetallurgica Inc.
8. Chatterjee, U. K., S. K. Bose, S. K. Roy. (2001). Environmental Degradation of Metals. CRC Press. Marcel Dekker, Inc. pp. 414-421
9. Davis, Joseph R. (2001). Copper and Copper Alloys. New York: ASM International.
10. Deng, X., R. S. Sidhu, P. Johnson and N. Chawla. (2005). Influence of reflow and thermal aging on the shear strength and fracture behavior of Sn-3.5Ag solder/Cu joints. Metallurgical and Materials Transactions A. Vol. 36, No 1. pp. 55-64.
11. Dowson, Duncan. (1998). History of Tribology. London: Professional Engineering Publishing Limited.
12. European Union. The Office for Official Publications of the European Communities (2003). Directive 2002/95/EC of the European Parliament and of the Council of 27 January 2003: on the restriction of the use of certain hazardous substances in electrical and electronic equipment. Retreived on June 16, 2008 from: http://www.interwritelearning.com/rohs compliance.pdf.
13. European Union. The Office for Official Publications of the European Communities (2005). Commision Decision of 13 October 2005 amending for the purposes of adapting to the technical progress the Annex to Directive 2002/95/EC of the European

Parliament and of the Council on the restriction of the use of certain hazardous substances in electrical and electronic equipment . Retrieved on June 16, 2008 from: http://www.reachcompliance.eu/english/ legislation/docs/launchers/launch-2005-717-EC.html.

14. Glaeser, William A. (1992). Materials for Tribology. New York: Elsevier.
15. Herian, J.and K. Anio. (2008). The structure and properties of steel with different pearlite morphology and its resistance to abrasive wear. Archives of Materials Science and Engineering. Vol. 31, No. 2. pp. 83-86.
16. Humpston, Giles and David M. Jacobson. (2004). Principles of Soldering. Ohio: ASM International.
17. Keast, V.J. and D. B. Williams. (1999). Quantitative Compositional Mapping of Bi Segregation to Grain Boundaries in Cu. Acta Matter.Vol 47. No 15. Pp 3999-4008. ActaMetallurgica, Inc.
18. Khonsari, Michael M. and E. Richard Booser. (2001). Applied Tribology: Bearing Design and Lubrication. New York: John Wiley and Sons, Inc.
19. Lambeck, Raymond P. (1983). Hydraulic Pumps and Motors: Selection and Application for hydraulic Power Control Systems. New York: Marcel and Dekker, Inc.
20. Lansdown A.R. and A. L. Price. (1986). Materials to Resist Wear: A Guide to their Selection and Use. New York: Pergamon Press.
21. Laporte, V., K. Wolski, P. Berger, A. Terlain, and G. Santarini. (2005). Diffusion-Controlled Liquid Bismuth Induced IntergranularEmbrittlement of Copper.Defect and Diffusion Forum Vols. 237-240. pp. 683-688
22. Liu, A. F. ( 2005). Mechanics and Mechanisms of Fracture. ASM International. pp.76
23. Lunn, B. (1965). The Wear Resistance of Tin Bronzes and Related Alloys. *Wear*, 8, 401-406.
24. Nenakhov, A. V. and A. G. Kostornov. (2003). Tribological Characteristics Of Materials Based On Bronze For Small Friction Assemblies. Powder Metallurgy and Metal Ceramics, Vol. 42, Nos. 7-8.
25. Okamoto, H. (1999). Mn-Sn (Manganese-Tin). Journal of Phase Equilibria. Vol. 20, No. 5. pp542.

26. Peterson, Marshall B and Ward O Winer. (1980). Wear Control Handbook. New York: American Society of Mechanical Engineers.
27. Sauer Danfoss (2009). Unpublished.
28. Saxton, David M. (2006). Lead-Free Replacements for SAE 792 in Bushing Applications. Federal Mogul Corporation. SAE International.
29. Shpenkov, George Petrovich. (1995). Friction Surface Phenomena. Tribology Series. V 29. New York: Elsevier.
30. Simons, Eric N. (1972) Metal Wear: a brief outline. New York: Elsevier.
31. Strauss, Joe (2009). Private Communication.
32. Summers-Smith, J.D. (1994). An Introductory Guide to Industrial Tribology. London: Mechanical Engineering Publications Limited.
33. Thümmler, F. and R. Oberacker. (1993). Introduction to Powder Metallurgy. Cambridge, The University Press.
34. Totten, George E. and Hong Liang. (2004). Surface modification and mechanisms: friction, stress and reaction engineering. New York, Macel Dekker.
35. United States Environmental Protection Agency. (2008). Priority Chemicals and Chemical Fact Sheets . Retrieved June 16, 2008 from: http://www.epa.gov/epaoswer/hazwaste/minimize/chemlist.htm.
36. Villforth III, Frederick J. (1996). Hydraulics. Lubrication, 82(1), 1-23.
37. Zum Gahr, Karl-Heinz. (1987). Tribology Series: Vol. 10. Microstructure and Wear of Materials. New York: Elsevier.

# ACKNOWLEDGEMENTS

First and foremost, I would like to express my gratitude to Dr. Iver Anderson for giving me the opportunity to complete a master's degree at Iowa State. The advice and direction he provided allowed me to grow as a student, an engineer, and a person. I would like to thank Matt Besser for his advice and guidance throughout my project, and for patiently allowing me to use his laboratory and equipment for my studies. Lanny Lincoln and Dave Byrd deserve credit for helping me with sample preparation and general laboratory assistance

I am grateful for the funding that Sauer Danfoss provided for this project and my advanced education. The engineers at Sauer Danfoss also deserve credit for their assistance in the project. Mike Betz, Jake Auliff, David Wills, Marc Diesselberg, and Sam Hall each contributed to my graduate studies in some way.

I would also like to thank the members of Dr. Anderson's research group: Emma White, Nathaniel Oster, Joel Rieken, Adam Boesenberg, John Meyer, Scott Long and Benjamin Rattle, as well as my committee members: Dr. Scott Chumbley and Dr. Palaniappa A. Molian.

And finally, I would not be where I am today were it not for the support of my family. I'd like to thank my mother, Dale; my father, Galen; and my sisters, Kate and Shawnda, for their support through the years. This thesis is written in loving memory of my mother, who remains my greatest source of motivation.